U.S. Department of Energy
FreedomCAR and Vehicle Technologies, EE-2G
1000 Independence Avenue, S.W.
Washington, D.C. 20585-0121

FY2006

WIDE-BANDGAP SEMICONDUCTORS

Prepared by:

Oak Ridge National Laboratory
Mitch Olszewski, Program Manager

Submitted to:

Energy Efficiency and Renewable Energy
FreedomCAR and Vehicle Technologies
Vehicle Systems Team

Susan A. Rogers, Technology Development Manager

November 2005

OAK RIDGE NATIONAL LABORATORY

MANAGED BY UT-BATTELLE FOR THE DEPARTMENT OF ENERGY

ORNL/TM-2005/214

Engineering Science and Technology Division

WIDE-BANDGAP SEMICONDUCTORS

M. S. Chinthavali[2]
B. Ozpineci[1]
L. M. Tolbert[1]
A. S. Kashyap[2]

[1]Oak Ridge National Laboratory
[2]Oak Ridge Institute for Science and Technology

Publication Date: November 2006

Prepared by the
OAK RIDGE NATIONAL LABORATORY
Oak Ridge, Tennessee 37831
managed by
UT-BATTELLE, LLC
for the
U.S. DEPARTMENT OF ENERGY
Under contract DE-AC05-00OR22725

ORNL-27 (4-00)

This report was prepared as an account of work sponsored by an agency of the United States Government. Neither the United States Government nor any agency thereof, nor any of their employees, makes any warranty, express or implied, or assumes any legal liability or responsibility for the accuracy, completeness, or usefulness of any information, apparatus, product, or process disclosed, or represents that its use would not infringe privately owned rights. Reference herein to any specific commercial product, process, or service by trade name, trademark, manufacturer, or otherwise, does not necessarily constitute or imply its endorsement, recommendation, or favoring by the United States Government or any agency thereof. The views and opinions of authors expressed herein do not necessarily state or reflect those of the United States Government or any agency thereof.

TABLE OF CONTENTS

Page

LIST OF FIGURES iv

LIST OF TABLES vii

1. INTRODUCTION 1

2. SiC DEVICES
   - 2.1 INTRODUCTION 2
   - 2.2 SiC SCHOTTKY DIODES 2
     - 2.2.1 Static Characteristics 3
     - 2.2.2 Dynamic Characteristics 5
   - 2.3 SiC FIELD EFFECT TRANSISTOR (FET) DEVICES 9
     - 2.3.1 Static Characteristics
       - 2.3.1.1 SiC JFET 10
       - 2.3.1.2 SiC MOSFET 11
       - 2.3.1.3 Gate-drive requirements 14
     - 2.3.2 Dynamic Characteristics 15
   - 2.4 CONCLUSIONS 19

3. HYBRID Si-SiC INVERTER
   - 3.1 OBJECTIVE 20
   - 3.2 WHY A HYBRID INVERTER 20
   - 3.3 TESTING AND MODELING THE 75-A DIODE 20
     - 3.3.1 SiC SBD On-State Testing 20
     - 3.3.2 SiC Diode Modeling 21
     - 3.3.3 Parameter Extraction and Model Validation Using the Characterized Data for Diodes 22
   - 3.4 SCHOTTKY DIODE AT DIFFERENT TEMPERATURES 23
   - 3.5 SIMULATION OF Si IGBT–SiC SCHOTTKY DIODE HYBRID INVERTER 25
   - 3.6 CONFIGURATION OF THE INVERTER 30
     - 3.6.1 Normal Mode 32
     - 3.6.2 Debug Mode 32
   - 3.7 INVERTER TESTING 32
     - 3.7.1 Isolation Impedance 33
     - 3.7.2 R-L Load Test 33
       - 3.7.2.1 Test setup 33
       - 3.7.2.2 Operation 34
       - 3.7.2.3 Results 35
     - 3.7.3 Dynamometer Test 38
       - 3.7.3.1 Test setup 38
       - 3.7.3.2 Motoring mode 39
       - 3.7.3.3 Regeneration mode 43
   - 3.8 EXPLANATION FOR THE POWER LOSS DIFFERENCE BETWEEN THE INVERTERS 46
   - 3.9 CONCLUSIONS 48

TABLE OF CONTENTS (cont'd)

Page

4. ALL-SiC INVERTER
 4.1 INTRODUCTION 50
 4.2 JFET CHARACTERIZATION AND MODELING
  4.2.1 SiC JFET Characterization 50
  4.2.2 SiC JFET Modeling 54
  4.2.3 Parameter Extraction and Model Validation of the Rockwell SiC JFET 56
 4.3 SIMULATION OF ALL-SiC INVERTER 61
 4.4 CONFIGURATION OF THE INVERTERS 64
 4.5 INVERTER TESTING
  4.5.1 Testing the Controller 65
  4.5.2 Resistive- and Inductive-Load Tests 67
   4.5.2.1 Operation 67
   4.5.2.2 Results 68
 4.6 CONCLUSIONS 74

5. DURATION TESTS
 5.1 INTRODUCTION 76
 5.2 TEST SETUP 76
 5.3 OPERATION 78
 5.4 DEVICE FAILURE DISCUSSION 91
 5.5 CONCLUSIONS 92

6. CONCLUSIONS 93

7. REFERENCES 94

APPENDIX A. o-v CHARACTERISTICS OF SiC AND Si DIODES 96

APPENDIX B: MOVING AVERAGE FILTER EXPLANATION 98

DISTRIBUTION 99

LIST OF FIGURES

Figure **Page**

2.1 Cross-section of a SBD 2
2.2 i-v characteristics of Si pn and SiC Schottky diodes at 27°C and SiC diodes at different operating temperatures 3
2.3 i-v characteristics of S3 (600 V, 10 A) at different operating temperatures 3
2.4 V_d for Si and SiC diodes at different operating temperatures 4
2.5 R_d for Si and SiC diodes at different operating temperatures 5
2.6 Reverse-recovery test circuit 6
2.7 Reverse-recovery test setup 6
2.8 Reverse-recovery waveforms showing the diode current (top) and voltage (bottom) for the diode S3 7
2.9 Reverse-recovery waveforms showing the diode current (top) and voltage (bottom) for the diode S2 7
2.10 Reverse-recovery waveforms showing the diode current (top) and voltage (bottom) for the diode S4 8
2.11 Reverse-recovery waveforms showing the diode current (top) and voltage (bottom) for the diode S1 8
2.12 Reverse-recovery waveforms showing the diode current (top) and voltage (bottom) for the Si pn diode 9
2.13 Turn-off energy losses with respect to forward current at different operating temperatures 9
2.14 *i-v* characteristics of SiC JFET at different temperatures 10
2.15 On-resistance of SiC JFET at different temperatures 11
2.16 Transfer characteristics of several SiC JFET samples 11
2.17 Forward characteristics of SiC MOSFET at room temperature 12
2.18 Forward characteristics of SiC MOSFET at different temperatures 12
2.19 On-resistance of SiC MOSFET at different temperatures 13
2.20 Transfer characteristics of SiC MOSFET at different temperatures 13
2.21 Gate threshold voltage of SiC MOSFET at different temperatures 14
2.22 The peak-gate currents and gate-voltage waveforms (a) SiC JFET and (b) SiC MOSFET 15
2.23 The gate and switching waveforms of the SiC JFET 16
2.24 The gate and switching waveforms of the SiC MOSFET 17
2.25 Energy loss plots: (a) SiC JFET, (b) SiC MOSFET 18
3.1 i-v characteristics of the 75-A SiC diode from Cree 21
3.2 Model topology of the power diode 21
3.3 Measured (solid) and simulated (dotted) on-state waveforms of SiC Schottky diode at different temperatures 23
3.4 Measured (solid) and simulated (dotted) reverse-recovery waveforms of the SiC Schottky diode from Cree 24
3.5 Simulation showing the reverse-recovery current in a SiC diode for different values of junction capacitances 25
3.6 Schematic representation of the hybrid inverter in Saber 26
3.7 Simulated three-phase load currents in the hybrid inverter 27
3.8 Simulated phase voltage (phase 1) in the hybrid inverter 27
3.9 Total instantaneous output power from the three phases of the hybrid inverter. 28
3.10 Comparison of peak-power output vs. efficiencies for hybrid and all-Si inverter 29
3.11 Comparison of efficiencies (from simulation) of hybrid and all-Si inverter 29

LIST OF FIGURES

Figure **Page**

3.12 Inverter topology ... 30
3.13 Semikron inverter unit. ... 30
3.14 75-A Schottky diodes developed by Cree. ... 30
3.15 Block diagram of the control system ... 31
3.16 A screen shot of the user interface software ... 32
3.17 R-L load test setup. ... 34
3.18 R-L load test operating waveforms. ... 35
3.19 R-L load test efficiency curves for various load conditions. ... 36
3.20 Inverter dyne test setup ... 38
3.21 100-hp dyne cell. ... 39
3.22 Dynamometer test–motoring mode operating waveforms. ... 40
3.23 Dynamometer test–motoring mode efficiency plots at 70ºC ... 41
3.24 Dynamometer test–motoring mode data obtained from the power meter ... 42
3.25 Dynamometer test–regeneration mode operating waveforms. ... 44
3.26 Dynamometer test–regeneration mode efficiency plots at 70°C ... 45
3.27 Comparison of static characteristics of Si pn diode and SiC Schottky diodes. ... 47
3.28 Comparison of reverse-recovery characteristics of Si pn diode and SiC Schottky diode ... 48
3.29 Instantaneous output power during regeneration. ... 48
4.1 Cross-section of the SiC JFET structure ... 50
4.2 Unipolar operation of the Rockwell SiC JFET. ... 51
4.3 Bipolar operation of the Rockwell SiC JFET. ... 51
4.4 Test for obtaining the pinch-off voltage. ... 52
4.5 Turn-on waveforms of the SiC JFET. ... 53
4.6 Turn-off waveforms of the SiC JFET. ... 53
4.7 Internal topology of the SiC JFET ... 54
4.8 Transfer characteristic of the Rockwell JFET. ... 57
4.9 Extraction of channel modulation factor LAMBDA. ... 57
4.10 Rockwell SiC JFET measured (solid) and simulated (dotted) on-state waveforms at 25°C for different gate voltages (V_{gs} ranging from 0 V to −2.5 V) ... 58
4.11 Extraction of channel modulation factor LAMBDA. ... 59
4.12 SiC JFET simulated (dashed) and measured (solid) turn-on waveforms at 25°C: (a) gate voltage, (b) drain voltage, and (c) drain current ... 59
4.13 SiC JFET simulated (dashed) and measured (solid) turn-off waveforms at 25°C: (a) gate voltage, (b) drain voltage, and (c) drain current ... 60
4.14 Schematic representation of the all-SiC inverter. ... 62
4.15 On-state validation of SiC diode at 25°C—measured (solid) and simulated (dashed). ... 62
4.16 Reverse-recovery validation of SiC diode at 25°C—measured (solid) and simulated (dashed) ... 63
4.17 Simulated output voltage in phase 1 of the all-SiC inverter with resistive load ... 63
4.18 All-SiC module ... 64
4.19 All-Si module ... 64

LIST OF FIGURES

Figure **Page**

4.20 Gate-drive control unit 65
4.21 Controller output voltage with 30-V swing for SiC module 66
4.22 Controller output voltage with 20-V swing for Si module 66
4.23 Test setup for R-L load test 67
4.24 Operating waveforms of SiC module for R-L load test 68
4.25 Efficiencies comparison plot at 30-Hz operation for R-L load test 69
4.26 Efficiencies comparison plot at 40-Hz operation for R-L load test 69
4.27 Efficiencies comparison plot at 40-Hz operation for resistive-load test 70
4.28 Efficiencies comparison plot at 50-Hz operation for resistive-load test 70
4.29 Efficiencies comparison plot at 50-Hz operation for resistive-load test 71
4.30 Forward characteristics of IGBT and JFET in the Si and SiC modules 71
4.31 Forward characteristics of diodes in the Si and SiC modules 72
4.32 (a) Turn-off voltage waveform of SiC JFET 73
(b) Turn-on voltage waveform of SiC JFET 73
4.33 (a) Turn-off voltage waveform of Si IGBT 74
(b) Turn-on voltage waveform of Si IGBT 74
5.1 Test setup for duration testing 76
5.2 Four different buck converters 77
5.3 The buck-converter topology 77
5.4 Plot of temperature data for diodes without the filter 78
5.5 Plot of temperature data for switches without the filter 79
5.6 Temperature profile for power switches at 250-V, 10-kHz operation. 80
5.7 Turn-on current waveforms of Si IGBTs with SiC and Si diodes 81
5.8 Temperature profile for 10-kHz operation: (a) Switches; (b) Diodes 82
5.9 Comparison of static charactersitics for Si IGBT and SiC JFET 82
5.10 Temperature profile for diodes at 100-kHz operation. 83
5.11 Temperature profile for power switches at 100 kHz 83
5.12 Temperature profile for diodes at 125 kHz 84
5.13 Temperature profile for power switches at 125 kHz 84
5.14 Temperature profile for diodes at 150 kHz 85
5.15 Temperature profile for power switches at 150 kHz 85
5.16 Temperature profile for diodes at different operating frequencies 86
5.17 Temperature profile for power switches at different operating frequencies 86
5.18 Plot of temperature profile for diodes at 15 kHz 88
5.19 Plot of temperature profile for power switches at 15 kHz 88
5.20 Plot of temperature profile for diodes at 20 kHz 89
5.21 Plot of temperature profile for power switches at 20 kHz 89
5.22 Plot of temperature profile for diodes at 25 kHz. 90
5.23 Plot of temperature profile for power switches at 25 kHz 90
5.24 Plot of temperature profile for power switches at different frequencies 91
A.1 *i-v* characteristics of S1 (1200 V, 7.5 A) at different operating temperatures 96
A.2 *i-v* characteristics of S4 (300 V, 10 A) at different operating temperatures 96
A.3 *i-v* characteristics of S2 (600 V, 4 A) at different operating temperatures 97
A.4 *i-v* characteristics of Si pn diode (600 V, 10 A) at different operating temperatures 97

LIST OF TABLES

Table **Page**

3.1 SiC power diode model parameters and extraction characteristics for the Cree 75-A diode 26
3.2 Efficiencies of the hybrid inverter during testing and simulation........ 28
3.3 Efficiencies of the all-Si inverter during testing and simulation........ 28
4.1 SiC power JFET model parameters and extraction characteristics for the Rockwell 15-A JFET 61
5.1 Specifications of the devices used in the buck converters 77
5.2 Temperature data of power devices at 300-V, 10-kHz operation........ 80

1. INTRODUCTION

With the increase in demand for more efficient, higher-power, and higher-temperature operation of power converters, design engineers face the challenge of increasing the efficiency and power density of converters [1, 2]. Development in power semiconductors is vital for achieving the design goals set by the industry. Silicon (Si) power devices have reached their theoretical limits in terms of higher-temperature and higher-power operation by virtue of the physical properties of the material. To overcome these limitations, research has focused on wide-bandgap materials such as silicon carbide (SiC), gallium nitride (GaN), and diamond because of their superior material advantages such as large bandgap, high thermal conductivity, and high critical breakdown field strength.

Diamond is the ultimate material for power devices because of its greater than tenfold improvement in electrical properties compared with silicon; however, it is more suited for higher-voltage (grid level) higher-power applications based on the intrinsic properties of the material [3]. GaN and SiC power devices have similar performance improvements over Si power devices. GaN performs only slightly better than SiC. Both SiC and GaN have processing issues that need to be resolved before they can seriously challenge Si power devices; however, SiC is at a more technically advanced stage than GaN. SiC is considered to be the best transition material for future power devices before high-power diamond device technology matures.

Since SiC power devices have lower losses than Si devices, SiC-based power converters are more efficient. With the high-temperature operation capability of SiC, thermal management requirements are reduced; therefore, a smaller heat sink would be sufficient. In addition, since SiC power devices can be switched at higher frequencies, smaller passive components are required in power converters. Smaller heat sinks and passive components result in higher-power-density power converters. With the advent of the use of SiC devices it is imperative that models of these be made available in commercial simulators. This enables power electronic designers to simulate their designs for various test conditions prior to fabrication.

To build an accurate transistor-level model of a power electronic system such as an inverter, the first step is to characterize the semiconductor devices that are present in the system. Suitable test beds need to be built for each device to precisely test the devices and obtain relevant data that can be used for modeling. This includes careful characterization of the parasitic elements so as to emulate the test setup as closely as possible in simulations.

This report is arranged as follows:

- Chapter 2: The testing and characterization of several diodes and power switches is presented.
- Chapter 3: A 55-kW hybrid inverter (Si insulated gate bipolar transistor–SiC Schottky diodes) device models and test results are presented. A detailed description of the various test setups followed by the parameter extraction, modeling, and simulation study of the inverter performance is presented.
- Chapter 4: A 7.5-kW all-SiC inverter (SiC junction field effect transistors (JFET)–SiC Schottky diodes) was built and tested. The models built in Saber were validated using the test data and the models were used in system applications in the Saber simulator. The simulation results and a comparison of the data from the prototype tests are discussed in this chapter.
- Chapter 5: The duration test results of devices utilized in buck converters undergoing reliability testing are presented.

2. SiC DEVICES

2.1 INTRODUCTION

SiC unipolar devices such as Schottky diodes, JFETs, and metal oxide semiconductor field-effect transistors (MOSFETs) have much higher breakdown voltages than their Si counterparts, which makes them suitable for use in medium-voltage applications. At present, SiC Schottky diodes are the only commercially available SiC devices. The maximum ratings of these commercial devices are 1200 V and 20 A. Some other 600-V prototype Schottky diodes with a 100-A rating are in the experimental stage and are expected to be commercially available in the near future.

SiC Schottky diodes are being used in several applications and have been proven to increase the system efficiency compared with Si device performance [4]. A significant reduction in the weight and size of SiC power converters with an increase in the efficiency is projected [1, 2]. In the literature, the performance of SiC converters has been compared with that of traditional Si converters and has been found to be superior [5, 6].

This chapter presents the characteristics for several SiC diodes and power switches and compares their performance. Some applications require that devices be able to handle extreme environments that include a wide range of operating temperatures. In the following sections, the static and dynamic performances of some commercially available SiC Schottky diodes and experimental samples of SiC JFETs and MOSFETs tested over a wide temperature range will be presented.

2.2 SiC SCHOTTKY DIODES

The Schottky barrier diode (SBD) is a majority-carrier device that has minimal reverse-recovery charge and therefore switches extremely fast.

It consists of a metal in direct contact with the semiconductor drift region, which happens to be the voltage blocking layer as shown in Fig. 2.1. The semiconductor region under the metal is lightly doped, making the contact a rectifying one instead of ohmic. The type of metal contact used to fabricate the device determines the knee voltage of the device (the voltage at which the diode starts conducting).

Fig. 2.1. Cross-section of a SBD.

SiC Schottky diodes are majority-carrier devices and are attractive for high-frequency switching because they have lower switching losses than pn diodes. However, they have higher leakage currents, which affect the breakdown voltage ratings of the devices [7]. SiC Schottky diode test results presented in this report are designated as S1 (1200 V, 7.5 A), S2 (600 V, 4A), S3 (600 V, 10 A), and S4 (300 V, 10 A).

2.2.1 Static Characteristics

The static characteristics of different SiC Schottky diodes at room temperature are shown in Fig. 2.2. The threshold voltages (or the knee voltages) and the on-state resistances are different for the diodes because of the differences in device dimensions at different voltage and current ratings. The threshold voltage also varies with the contact metal used in the Schottky diodes because of the variation in the Fermi level for different metal-to-semiconductor contacts [8]. The static characteristics of one of the diodes (S3, 600 V, 10 A) over a temperature range of −50°C to 175°C are shown in Fig. 2.3. The static characteristics of the remaining diodes can be found in Appendix A.

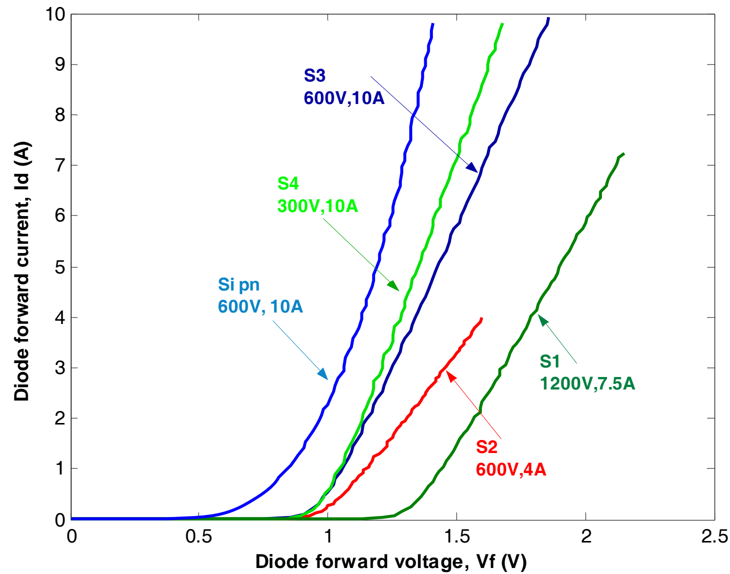

Fig. 2.2. i-v characteristics of Si pn and SiC Schottky diodes at 27°C and SiC diodes at different operating temperatures.

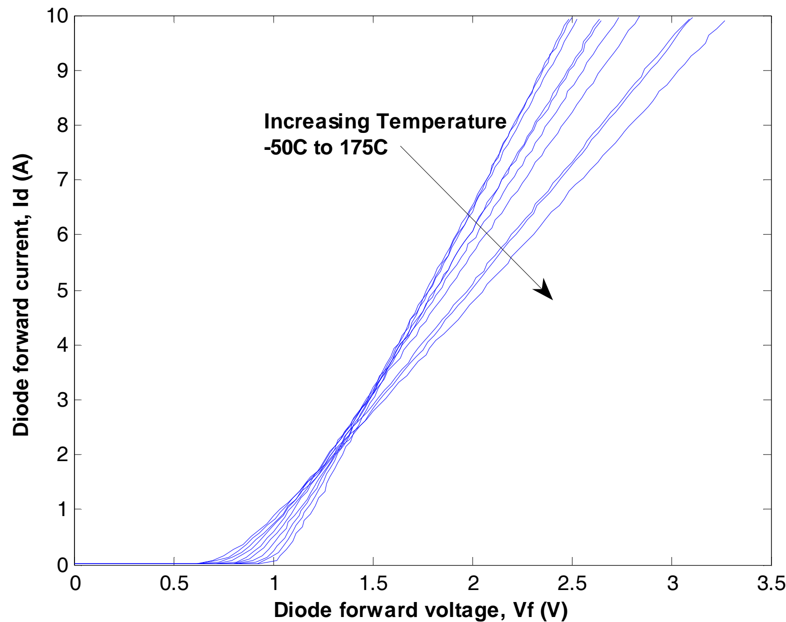

Fig. 2.3. i-v characteristics of S3 (600 V, 10 A) at different operating temperatures.

The approximate on-state voltage drop equation of a diode is given as

$$V_f = V_d + I_d \cdot R_d \,, \tag{2.1}$$

where V_d is the forward voltage drop and R_d is the series resistance of the diode obtained from the piece-wise linear (PWL) model of the diode. The PWL model parameters were extracted from the experimental test data in Fig. 2.3. The variation in V_d with temperature is plotted in Fig. 2.4 for all the diodes tested.

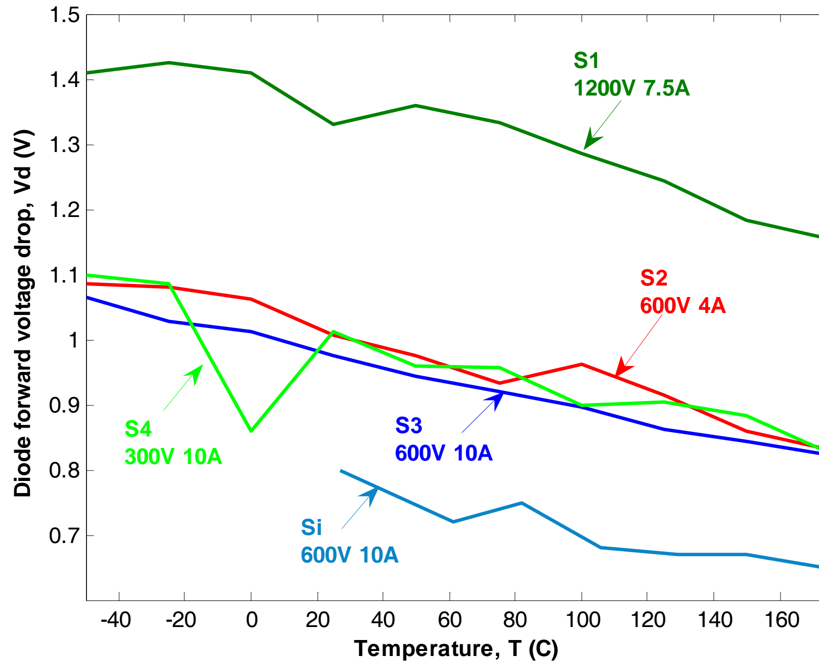

Fig. 2.4. V_d for Si and SiC diodes at different operating temperatures.

The on-state voltage drop of a Schottky diode depends on the barrier height and the on-state resistance, both of which vary with temperature. At lower current levels, as the temperature increases, the thermal energy of the electrons increase causing the lowering of the barrier height.

A lower barrier height means a lower barrier potential and a lower forward voltage drop [9]. At higher current levels, the on-state voltage drop is mainly because of the series resistance of the diode, which is one of the critical parameters that determine the performance of the device. The dominant component of the diode series resistance is the specific on-resistance, $R_{on,sp}$. $R_{on,sp}$ for majority-carrier devices can be expressed as a function of breakdown voltage and the critical electric field [10];

$$R_{on,sp} = \frac{4V_B^2}{\varepsilon(E_c)^3 \mu_n} \,, \tag{2.2}$$

where ε is the permittivity (C/V·cm), V_B is the breakdown voltage, E_c is the breakdown field (V/cm), and μ_n is the electron mobility (cm^2/V·s).

$R_{on,sp}$ increases with temperature because the mobility decreases at higher temperatures. Consequently, the diode series resistance increases with the temperature and the device has a positive-temperature

coefficient, which makes it easier to parallel the devices. The disadvantage, however, is that the diode conduction loss also increases with temperature.

The series resistance, R_d, for the diodes is calculated from the slope of the *i-v* characteristics at high currents and is plotted for different temperatures as shown in Fig. 2.5. The series resistance of each diode is unique because of the differences in blocking voltages and in the die area. To withstand high breakdown voltages, the blocking layer thickness must be increased and the doping concentrations must be reduced. This results in an increased series resistance of the diode. Hence, device S1 rated at 1200 V, 7.5 A has a higher series resistance than S3 (600 V) and S4 (300 V). The resistance also varies with the area of the device. It is evident from Fig. 2.5 that S2 and S3, with the same voltage but different current ratings, have different series resistances.

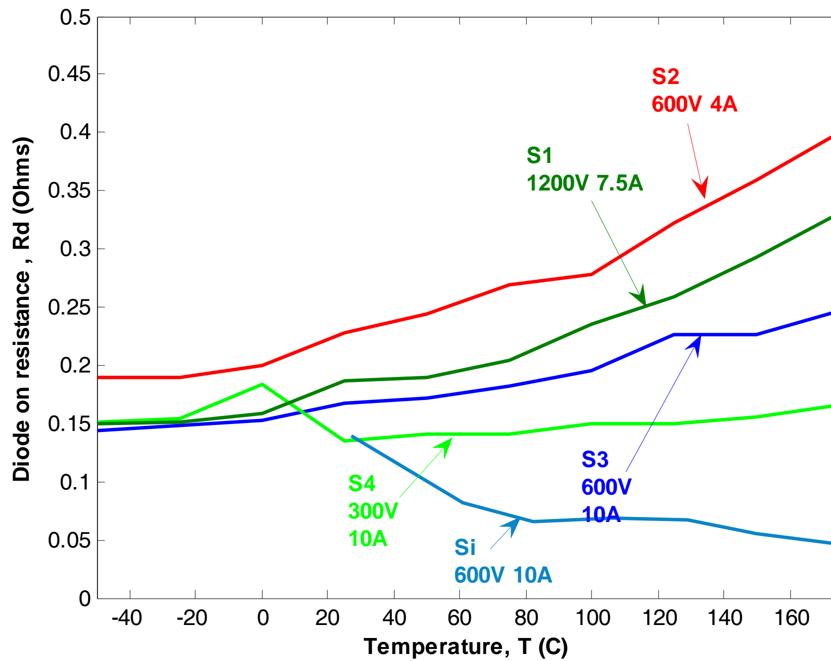

Fig. 2.5. R_d for Si and SiC diodes at different operating temperatures.

2.2.2 Dynamic Characteristics

A buck chopper with an inductive load was built to evaluate the switching characteristics of the diodes. The test circuit shown in Fig. 2.6 was built for the tests.

The test circuit consists of a gate-driver chip that drives the IGBT. The load includes a 24-mH inductor and a 45.5-Ω resistor (with a maximum power dissipation rating of 1200 W) in series. The IGBT was switched at 5 kHz with a duty cycle of 50%. The reverse-recovery tests were performed at different direct current (dc) voltages ranging from 50 to 200 V.

The tests were performed for the following diodes: (a) S3 (600 V, 10 A), (b) S2 (600 V, 4 A), (c) S4 (300 V, 10 A), (d) S1 (1200 V, 7.5 A), and (e) a Si pn diode (600 V, 10 A) which was included for comparison purposes. Figure 2.7 shows the reverse-recovery test setup in the lab. Some of the reverse-recovery waveforms are shown in Figs. 2.8 and 2.9.

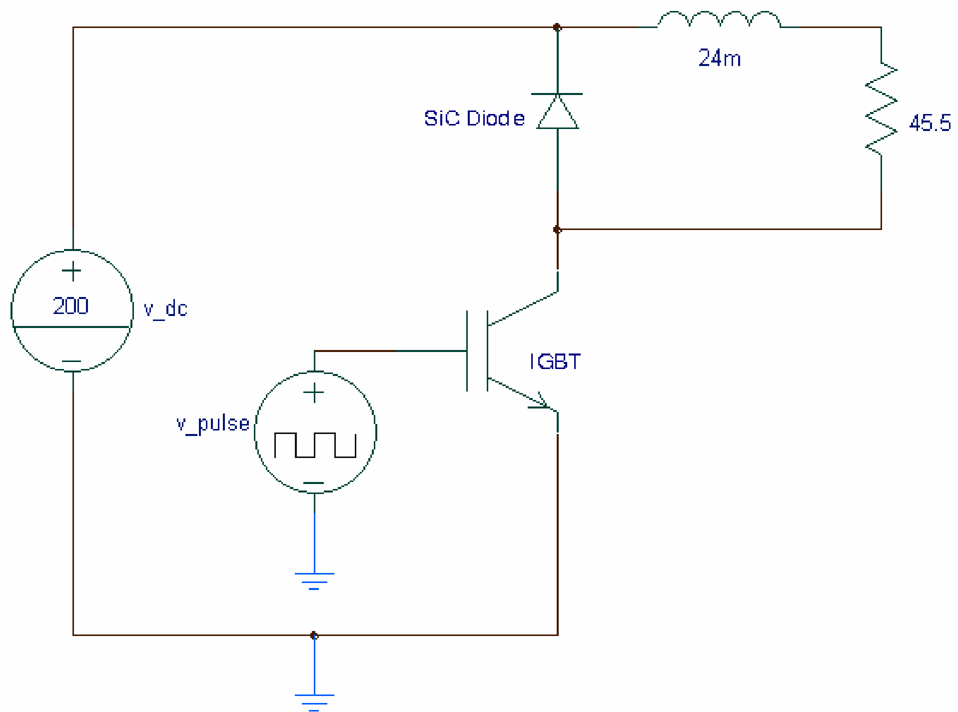

Fig. 2.6. Reverse-recovery test circuit.

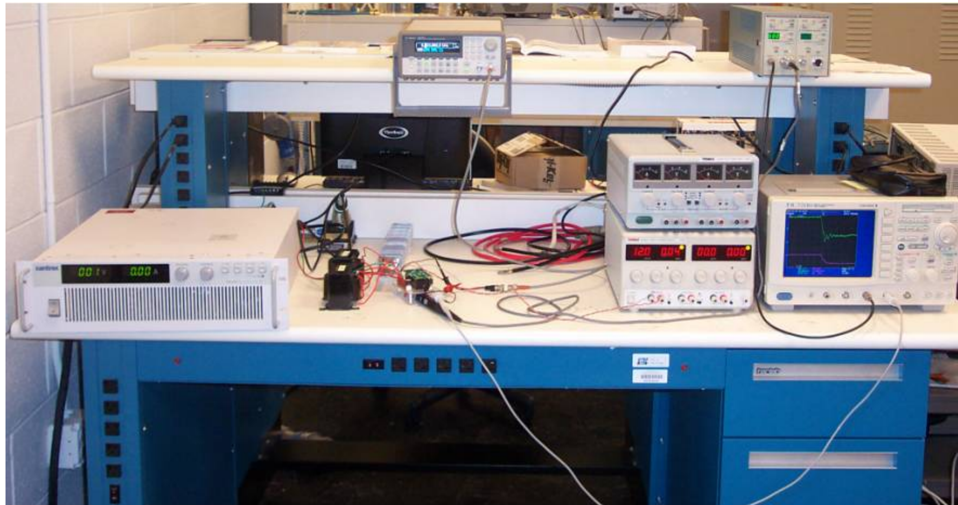

Fig. 2.7. Reverse-recovery test setup.

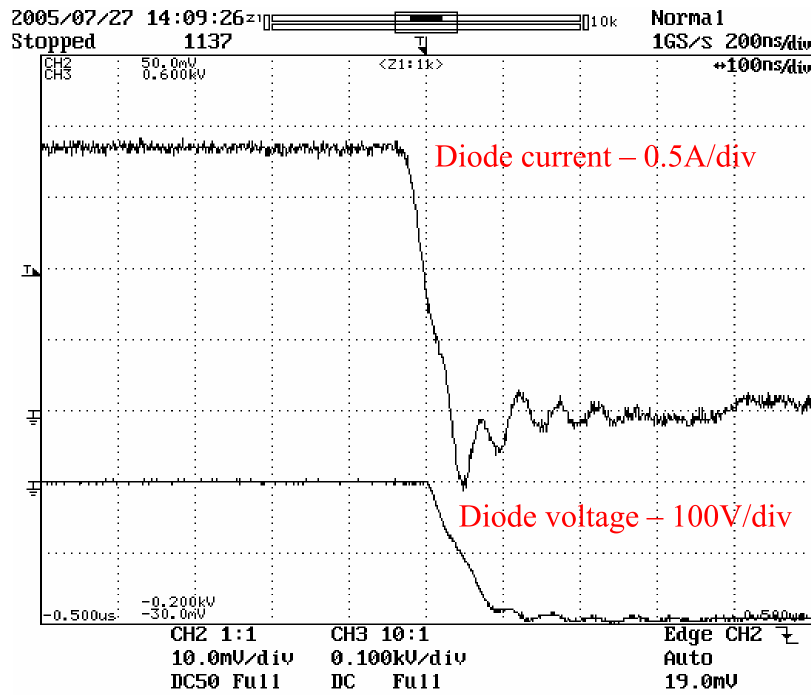

Fig. 2.8. Reverse-recovery waveforms showing the diode current (top) and voltage (bottom) for the diode S3.

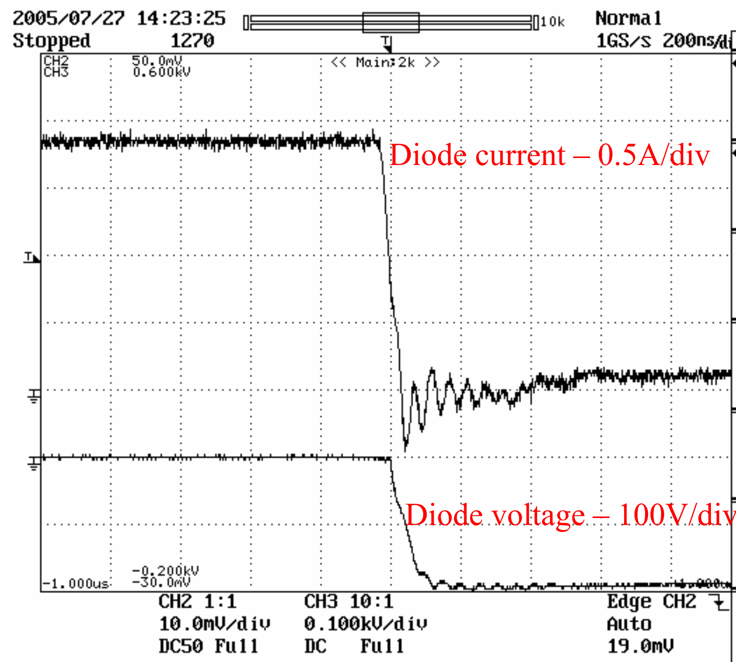

Fig. 2.9. Reverse-recovery waveforms showing the diode current (top) and voltage (bottom) for the diode S2.

The reverse-recovery waveforms for all the diodes tested are shown in Figs. 2.8, 2.10, 2.11, and 2.12. The energy losses for various forward peak currents at different temperatures are shown for the Si diode and

the SiC diode S4 in Fig. 2.13. The switching loss for the Si diode increases with temperature and forward current, while the switching loss for the SiC diode S4 is almost independent of the change in temperature and varies slightly with increasing forward current. The reason is that the reverse-recovery current of a diode depends on the charge stored in the drift region. Schottky diodes have no stored charge because they are majority-carrier devices and thus have no reverse recovery. However, oscillations due to parasitic internal pn diodes and capacitances look like reverse-recovery phenomena. The reduced reverse recovery of Schottky diodes makes it possible to reduce the size of the snubbers. Low reverse-recovery and snubber losses increase the efficiency of the power converters.

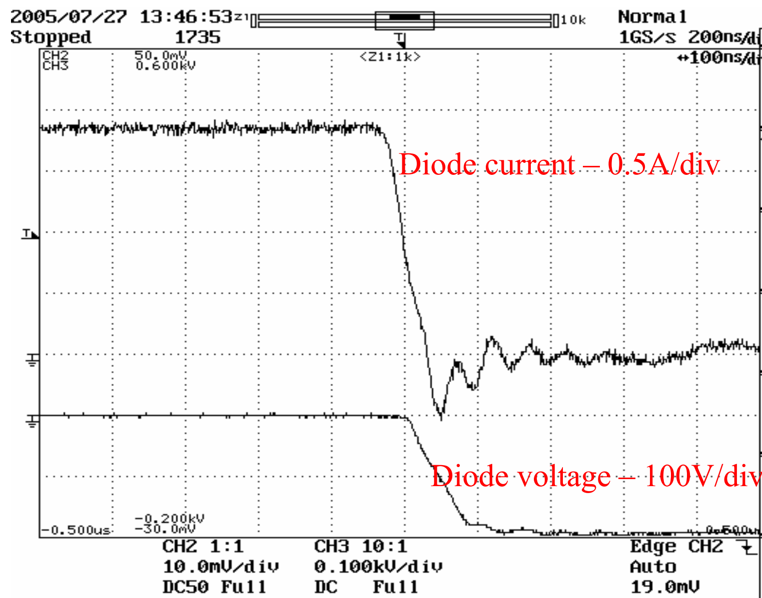

Fig. 2.10. Reverse-recovery waveforms showing the diode current (top) and voltage (bottom) for the diode S4.

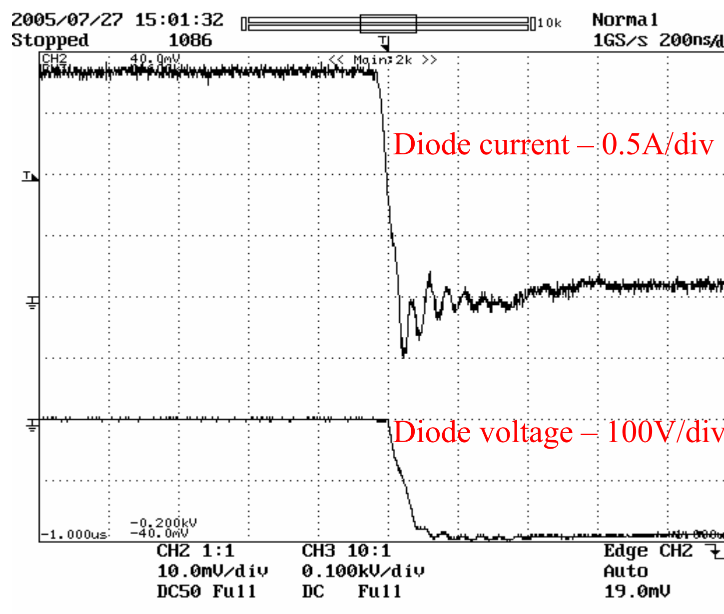

Fig. 2.11. Reverse-recovery waveforms showing the diode current (top) and voltage (bottom) for the diode S1.

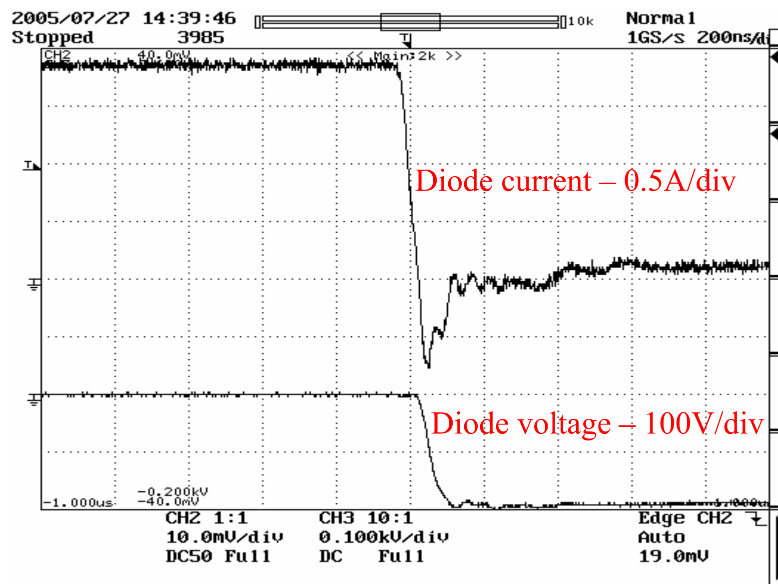

Fig. 2.12. Reverse-recovery waveforms showing the diode current (top) and voltage (bottom) for the Si pn diode.

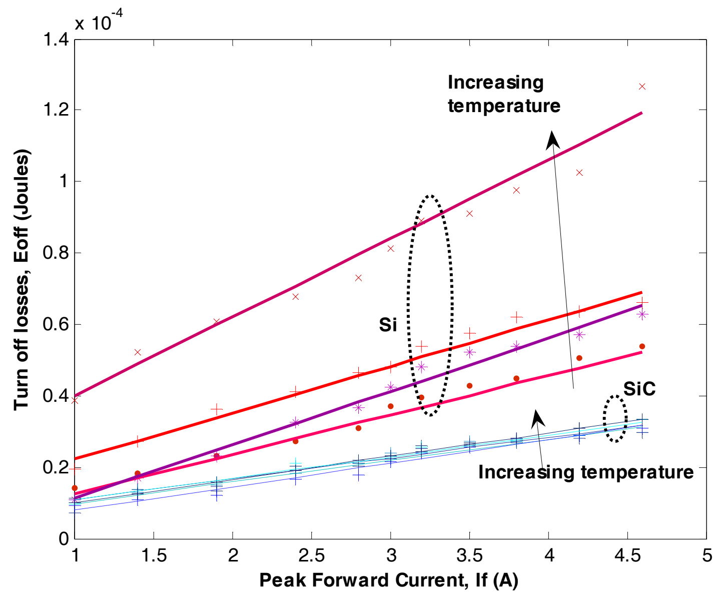

Fig. 2.13. Turn-off energy losses with respect to forward current at different operating temperatures.

2.3 SiC FIELD-EFFECT TRANSISTOR (FET) DEVICES

FET devices are majority-carrier devices and are preferred over minority-carrier devices in power converters. However, Si FET devices, like Si Schottky diodes, can only be used in low voltage (<300-V) applications because of their high on-state resistance. Even the first experimental SiC FET devices have blocking voltages of over 1000 V. It is expected that in the near future, SiC FET devices will dominate Si minority-carrier devices in the medium-voltage (< 3000-V) applications.

2.3.1 Static Characteristics

2.3.1.1 SiC JFET

A JFET is a unipolar device and has several advantages compared with MOSFET devices. A JFET has a low voltage drop and a higher-switching speed and is free from gate-oxide interface problems, unlike a MOSFET [11]. A SiC JFET is typically a normally-on device and conducts even though there is no gate voltage applied. A gate voltage must be applied for it to stop conduction. This feature dictates special gate-drivers, increasing the complexity of the design. A normally-on device is not desirable for power electronics since it requires additional protection circuitry to prevent a dc bus short if the gate signals fail.

A Si JFET is not classified as a power electronics device. The SiC JFET, however, can be used in high-voltage, high-power applications, unlike a Si JFET because of its vertical structure and the intrinsic properties of SiC.

A normally-on SiC JFET rated at 1200 V and 2 A was tested to study the high-temperature behavior of the device. The forward characteristics of this device at different temperatures are shown in Fig. 2.14. As seen in Figs. 2.14 and 2.15, SiC JFETs have a positive-temperature coefficient, which means that, like SiC Schottky diodes, their conduction losses will be higher at higher temperatures. A positive-temperature coefficient makes it easier to parallel these devices and reduce the overall on-resistance. The on-resistance of the JFET increases from 0.36 Ω at −50°C to 1.4 Ω at 175°C, as shown in Fig. 2.16.

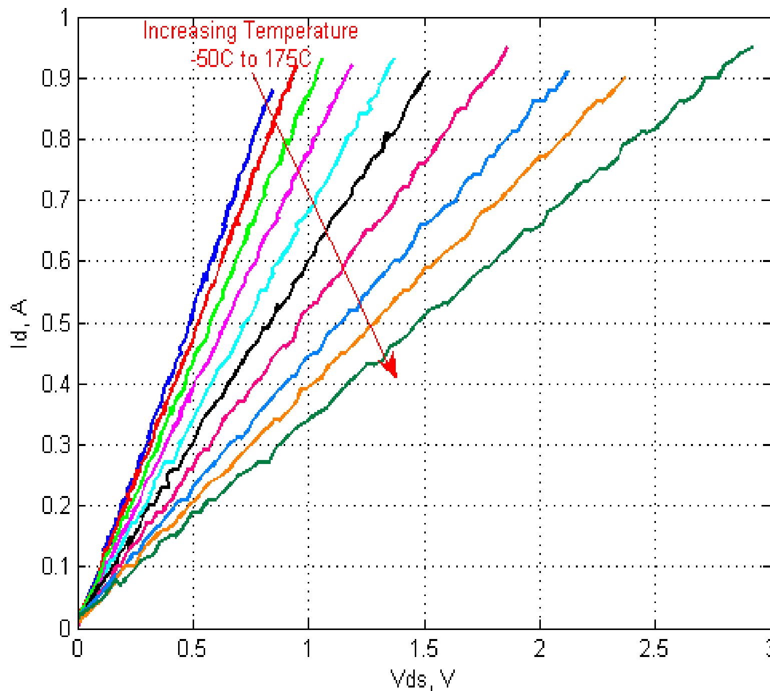

Fig. 2.14. *i-v* characteristics of SiC JFET at different temperatures.

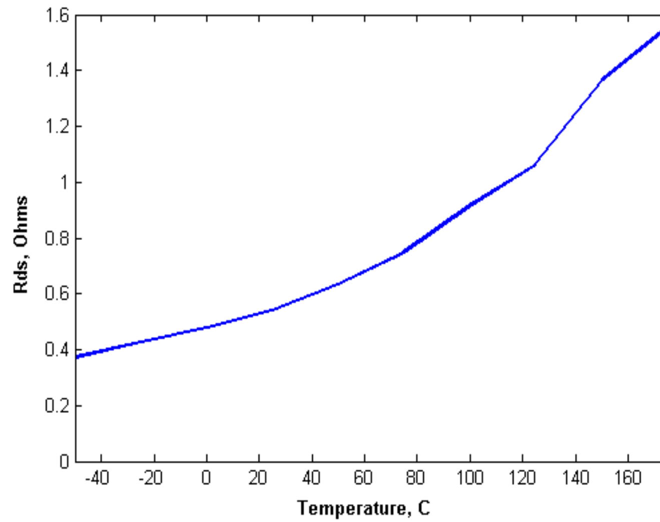

Fig. 2.15. On-resistance of SiC JFET at different temperatures.

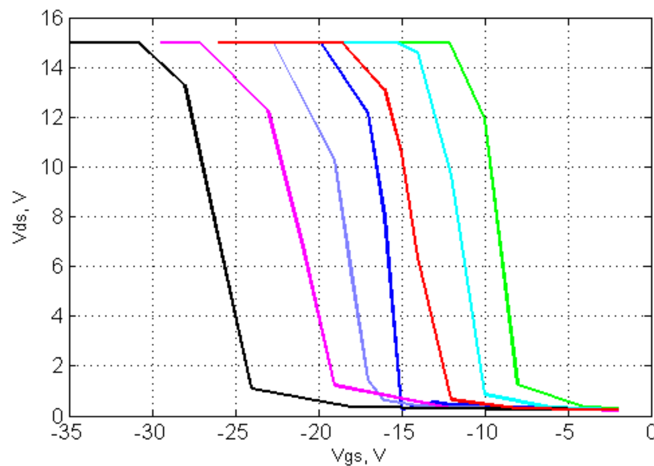

Fig. 2.16. Transfer characteristics of several SiC JFET samples.

The on-resistance is high; however, this device is a low-current-rated device and is an early prototype. It is expected that as the technology matures, lower on-resistances will be possible.

The transfer characteristics of different SiC JFET samples are shown in Fig. 2.16. The negative gate pinch-off voltage required to turn off the device is higher than that required for Si devices and varies from sample to sample. This variation is attributed to the fact that these devices are experimental samples.

2.3.1.2 SiC MOSFET

A MOSFET is a unipolar device and is normally off. The forward characteristics of a 1.2-kV, 15-A SiC MOSFET at room temperature are shown in Fig. 2.17. The gate voltage was varied from 0 to 20 V in increments of 5 V. For V_{gs} = 20 V, there is a 6.7-V drain-to-source voltage drop that corresponds to a 15-A drain current. Note that it would be more reasonable to operate this device at 5 A with V_{gs} = 20V because of a low voltage drop of 1.5 V. The forward characteristics of the same SiC MOSFET for a temperature range of −50 to 175°C are shown in Fig. 2.18. Note that the device's response to temperature

increase changes at 50°C. To get a better understanding of this phenomenon, the on-state resistances of the device are calculated from the slopes of the different curves and are plotted with respect to temperature in Fig. 2.19. It is interesting to note that this device has a negative temperature coefficient at up to 50°C and a positive-temperature coefficient above that. MOSFETs are majority-carrier devices and are expected to have positive-temperature coefficients. The components of the on-resistance of a MOSFET, can be expressed as the sum of several different resistances because of the different regions in the MOSFET structure

$$R_{on} = R_{cont} + R_{sub} + R_{ch} + R_{acc} + R_{jfet} + R_d \ , \tag{2.3}$$

where R_{cont} is the contact resistance, R_{sub} the substrate resistance, R_{ch} the channel resistance, R_{acc} the accumulation layer resistance, R_{JFET} the resistance of the JFET like region, and R_d is the resistance of the drift region [12].

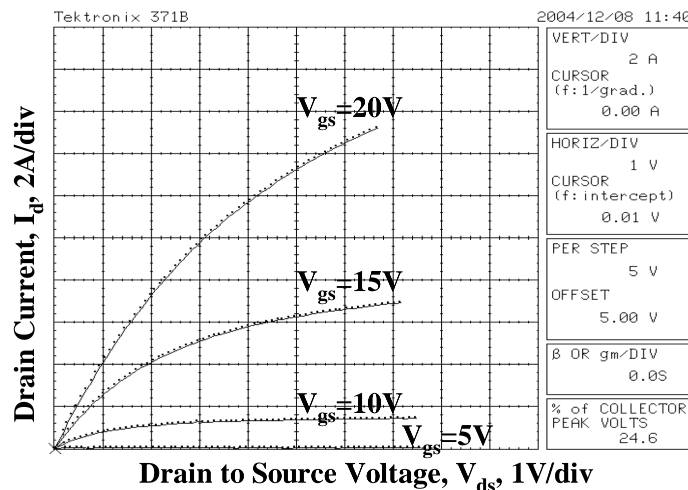

Fig. 2.17. Forward characteristics of SiC MOSFET at room temperature.

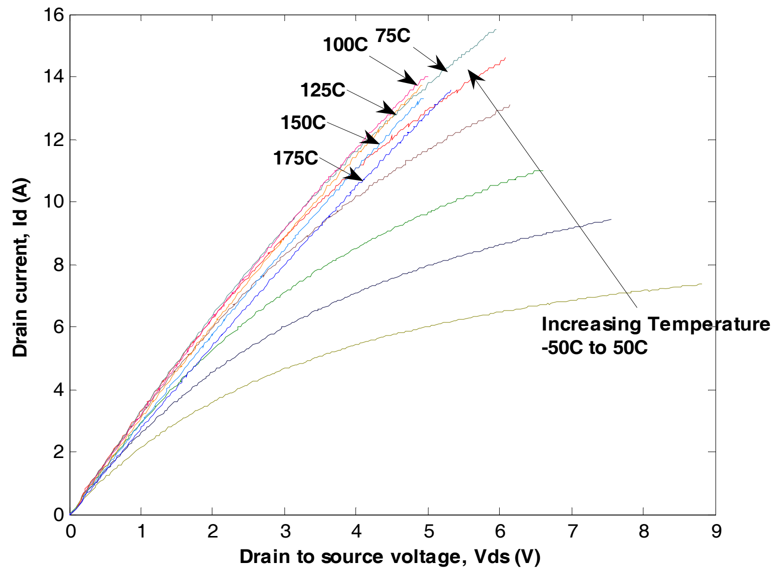

Fig. 2.18. Forward characteristics of SiC MOSFET at different temperatures.

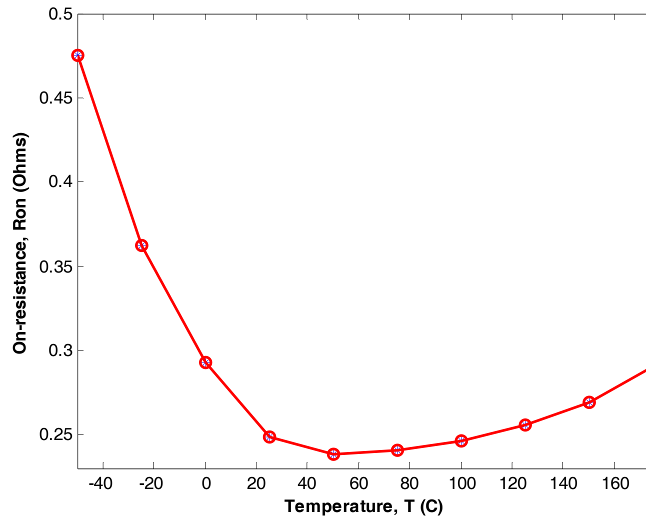

Fig. 2.19. On-resistance of SiC MOSFET at different temperatures.

At lower temperatures, the contribution of the channel resistance to the total on-state resistance is dominant [13]. The channel mobility increases with temperature because the interface traps are closer to the conduction band [13, 14]; thus the channel resistance decreases with temperature. Consequently, at low temperatures, the MOSFET on-resistance decreases. Above a certain temperature value, the channel resistance is not dominant; and because of the other dominant on-resistance components, the MOSFET overall on-resistance increases.

The SiC MOSFET gate-threshold voltage is measured from the transfer characteristics shown in Fig. 2.20. The gate-threshold voltage decreases with increasing temperature. Figure 2.21 shows the change in threshold voltage from 10.7 V at –50°C to 2.8V at 175°C. This change is due to the trapped charge in the SiO_2, as well as the impurities at the SiO_2 interface. These trapped charges become active at high temperatures, which results in a Fermi level shift toward the bandgap, causing the drain current to flow at low threshold voltages. In other words, less gate voltage is required at high temperatures for the same drain current to flow through the device.

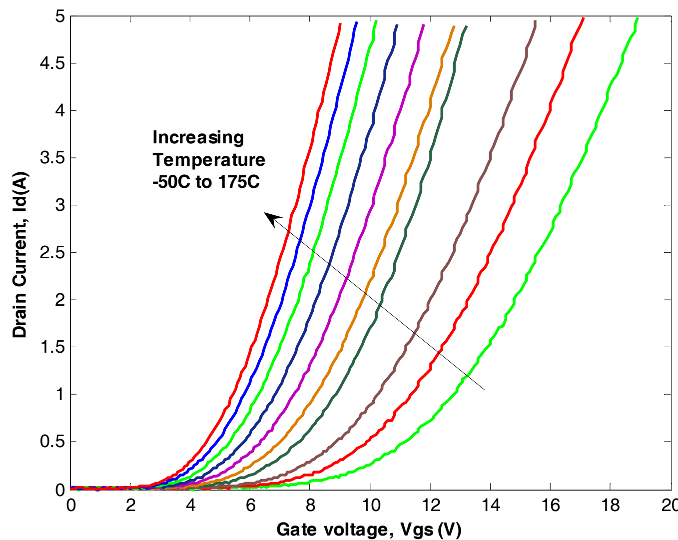

Fig. 2.20. Transfer characteristics of SiC MOSFET at different temperatures.

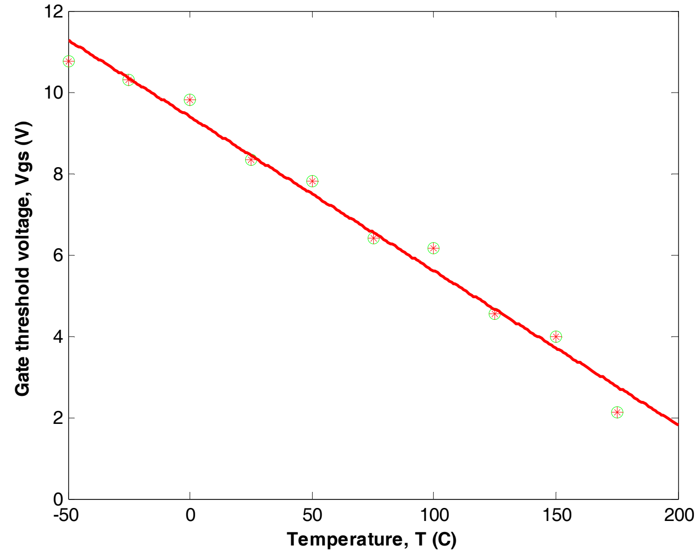

Fig. 2.21. Gate-threshold voltage of SiC MOSFET at different temperatures.

2.3.1.3 Gate-drive requirements

SiC FET switches can be operated at higher switching frequencies and higher temperatures; therefore, they have different gate-drive requirements compared with traditional Si power switches. The switching performance of the FET devices is determined by charging and discharging of the parasitic capacitances across the three terminals, input capacitance, reverse-transfer capacitance, and output capacitance. These capacitances are proportional to the area of the device [6]. Since SiC devices have smaller areas than comparable Si devices, even for high-blocking voltages, the capacitances are reduced. This enables devices to operate at higher switching speeds. A comparison of capacitance values for a SiC MOSFET and for a Si power switch is reported in [15].

One of the important parameters in gate-drive designs is the capacitance between the gate and the other terminals. Total input capacitance of the JFET, C_{iss}, determines the current required by the gate and the rate at which the applied gate voltage is built across the gate and source terminals. Therefore, the gate-drive circuit is required to have the capability of providing peak currents to charge the input capacitance quickly. The peak-gate current is limited by the series resistance between the gate and the gate-driver output. Higher gate-series resistance decreases the ringing effect due to the internal impedance of the device; however, it also results in slower turn-on times.

As mentioned earlier, there are several gate-drive circuit design options for SiC JFETs using transistors and other discrete devices [10, 16]. A commercial gate-driver chip IXDD414 was used in this project to drive the SiC FETs under test for a more reliable and quick gate-driver design. Note that this gate-driver chip can be used with most of the SiC JFETs whose transfer characteristics are shown in Fig. 2.16, as well as the SiC MOSFET samples. The gate driver can be redesigned to be used as a SiC MOSFET gate drive by replacing the series-gate resistor and reversing the output-voltage polarity. The peak-gate currents and gate-voltage waveforms driving a SiC JFET and a SiC MOSFET are shown in Fig. 2.22. As seen in this figure, a SiC MOSFET requires a higher current than a SiC JFET to operate at the same switching frequency, i.e. 250 kHz in this case.

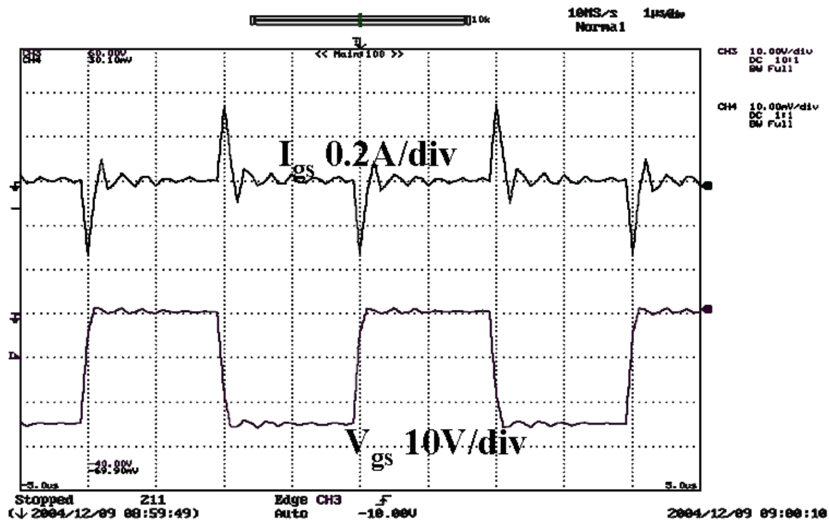

(a) SiC JFET

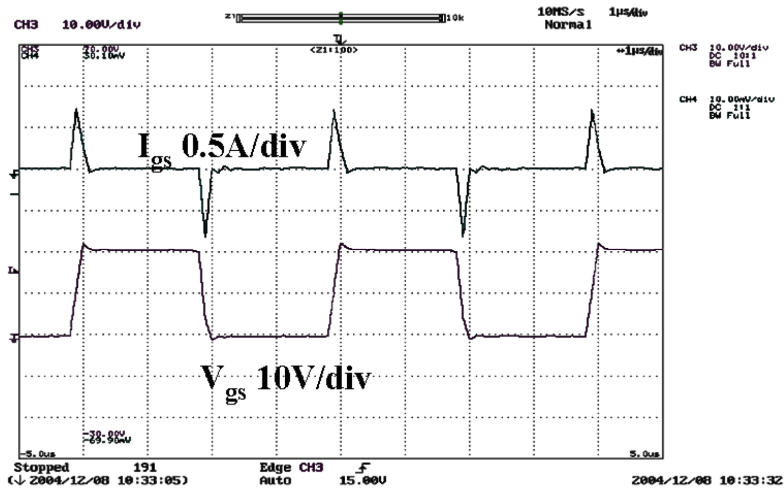

(b) SiC MOSFET

Fig. 2.22. The peak-gate currents and gate-voltage waveforms.

2.3.2 Dynamic Characteristics

The gate-drive circuit discussed in the previous section was used to determine the dynamic characteristics of the SiC MOSFET and JFET.

SiC JFETs are normally-on devices and they can be turned off only by applying a negative voltage that is higher than what a typical Si power device requires. Based on the transfer characteristics (Fig. 2.16), the gate drive was designed for a voltage of –25 V, since that would be enough to turn off most of the samples tested.

When SiC JFETs are operated at high frequencies, they need high peak-gate currents to charge and discharge the gate capacitances faster. For example, 250-kHz switching was achieved with a series-gate resistance of 5.4 Ω and a peak-gate current of 0.38 A.

The gate voltage and the switching waveforms of the JFET are shown in Fig. 2.23. The device has a turn-off delay $t_{d,off}$ of 40 ns, fall time t_f of 80 ns, turn-on delay $t_{d,on}$ of 20 ns, and rise time t_r of 100 ns.

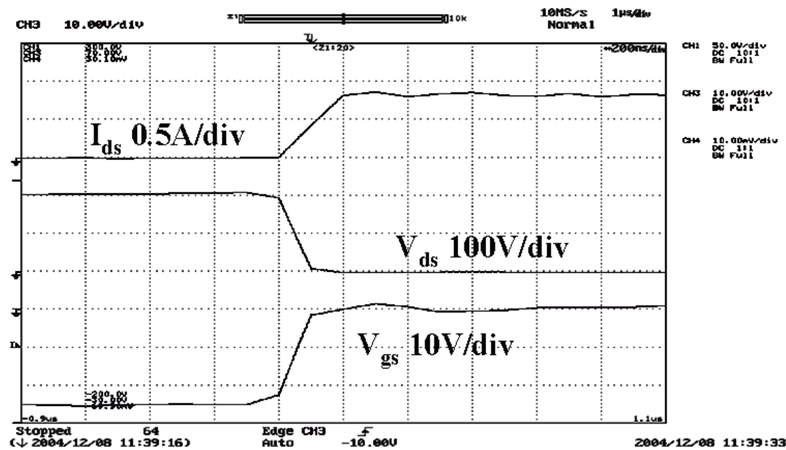

(a)

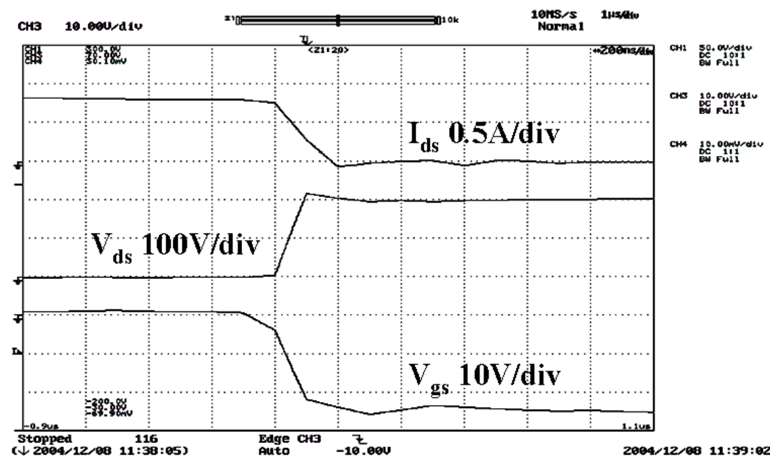

(b)

Fig. 2.23. The gate and switching waveforms of the SiC JFET.

The gate-drive voltage for the MOSFET was selected as 20 V, as determined from the forward characteristics to obtain the optimum performance. The 250-kHz operation was achieved with a series-gate resistance of 7.2 Ω and a peak-gate current of 0.6 A. The gate and switching waveforms for a SiC MOSFET are shown in Fig. 2.24. The device has a turn-off delay $t_{d,off}$ of 40 ns, fall time t_f of 100 ns, turn-on delay $t_{d,on}$ of 20 ns, and rise time t_r of 100 ns.

Note that both the SiC JFET and the MOSFET show fast dynamic responses, which would be required for high-frequency switching.

The turn-on and turn-off energy losses for both the SiC MOSFET and the JFET were calculated by integrating the instantaneous power over the turn-on (t_{on}) and turn-off times (t_{off}). The energy losses calculated for the SiC MOSFET and JFET at different temperatures for a 5-kHz, 50% duty cycle, 100-V,

0.8-A operation are shown in Fig. 2.25. It is interesting to note that a SiC JFET needs almost no energy to turn on because of its normally-on feature. Another observation from these figures is that the total switching losses do not vary much with temperature.

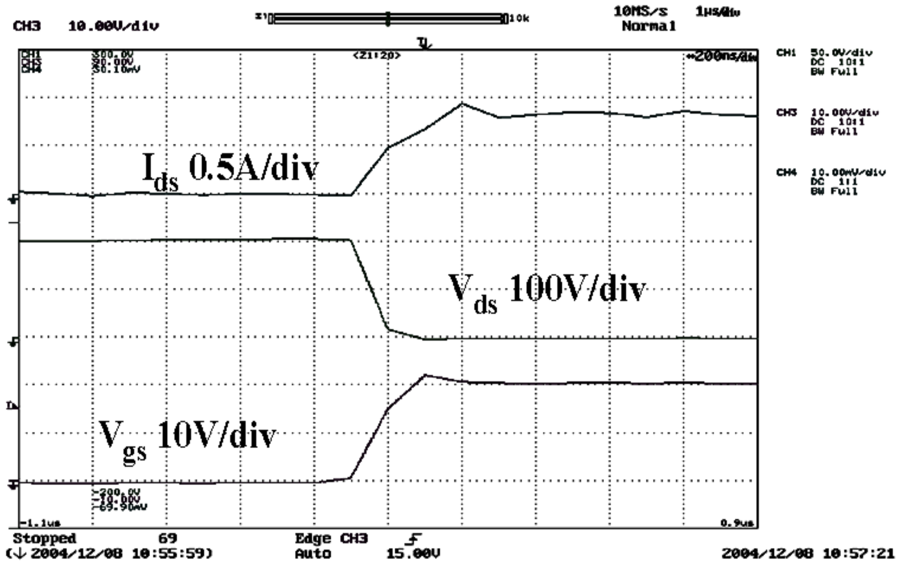

(a)

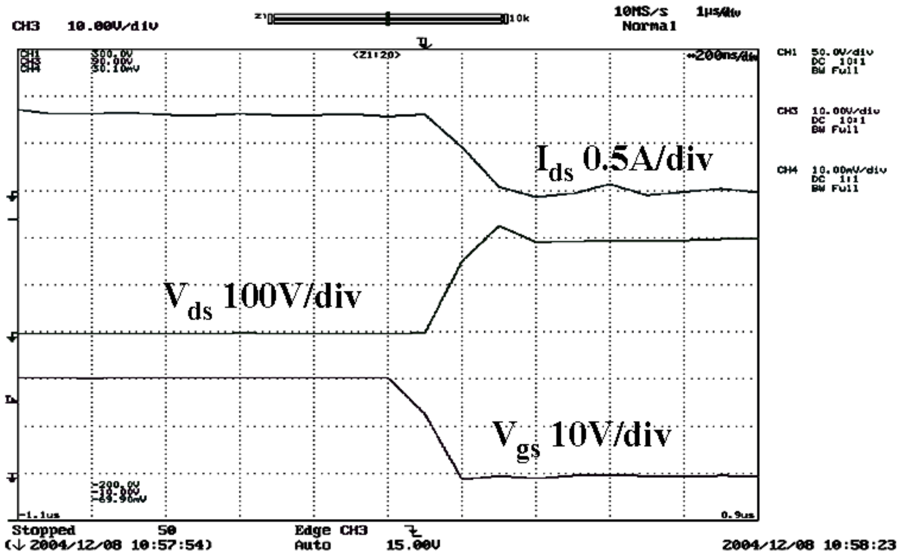

(b)

Fig. 2.24. The gate and switching waveforms of the SiC MOSFET.

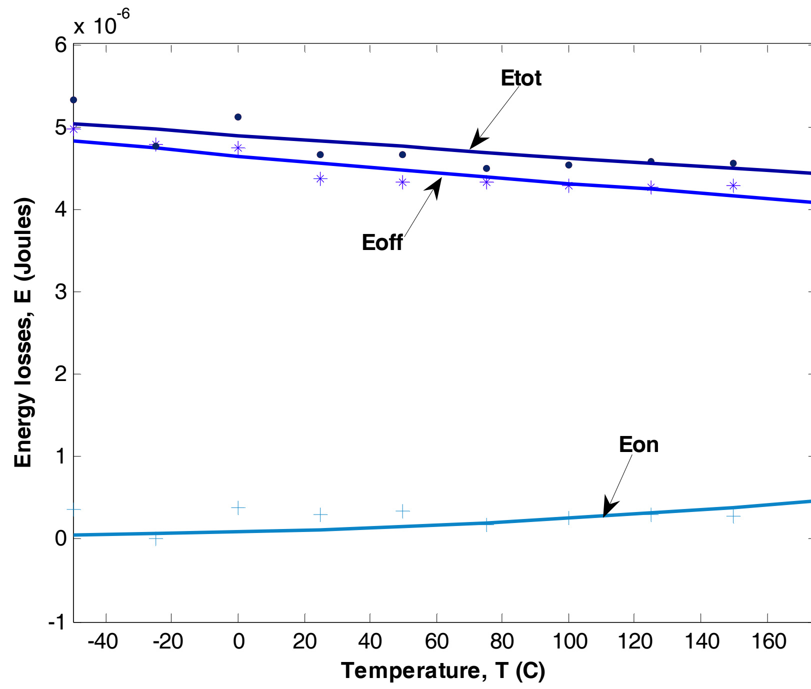

(a) SiC JFET.

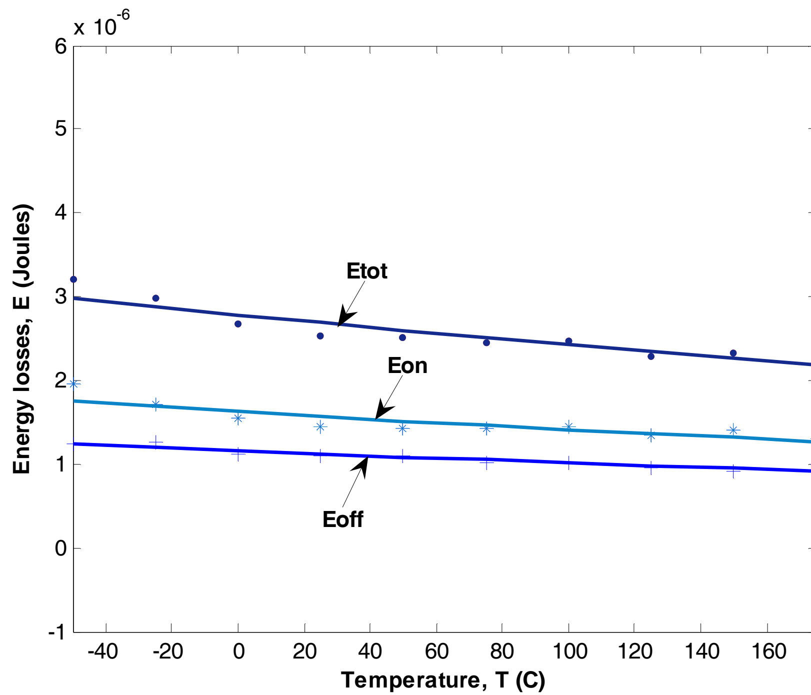

(b) SiC MOSFET.

Fig. 2.25. Energy loss plots.

2.4 CONCLUSIONS

The static and dynamic performances of some SiC Schottky diodes, SiC MOSFETs, and SiC JFETs were analyzed. It was observed that SiC Schottky diodes and JFETs have positive-temperature coefficients. However, SiC MOSFETs display a negative temperature behavior for temperatures below 50°C and a positive-temperature coefficient behavior above this value. This is due to the interface-trap defects in the SiC MOSFET, which will eventually be eliminated with maturing SiC manufacturing technology. SiC Schottky diodes showed excellent reverse-recovery characteristics compared with Si pn diodes. Even though SiC Schottky diodes have higher on-resistances, they exhibit near-perfect switching characteristics, making their performance superior to their Si counterparts. Thus replacing Si devices with comparable SiC Schottky diodes will improve the performance of the power switches in a power converter by reducing the switching stress on the switches and decreasing the overall losses.

The switching losses were almost constant for a wide temperature range for all the SiC unipolar devices presented in this report, showing that SiC unipolar devices are well suited for high-frequency, high-temperature, and high-power applications. Also, hard-switching circuits at higher power levels and higher frequencies can be realized using SiC devices because of their excellent switching characteristics. With further improvements in current ratings, SiC MOSFETs can replace Si IGBTs in medium-voltage applications. SiC MOSFETs are preferred over SiC JFETs because of their normally-off feature. However, gate-oxide reliability still remains an issue for SiC MOSFETs.

3. HYBRID Si-SiC INVERTER

3.1 OBJECTIVE

The objective is to evaluate the performance of a hybrid Si IGBT–SiC Schottky diode inverter and compare it with the performance of a similar all-Si inverter. The main focus of this project is to study the impact of replacing pn diodes with SiC Schottky diodes in an inverter by performing inductive load and dynamometer tests.

3.2 WHY A HYBRID INVERTER

SiC Schottky diodes have been proven to have better performance characteristics than similar Si pn diodes [17], especially with respect to switching characteristics as they have negligible reverse-recovery losses. SiC devices also can operate at higher temperatures, thereby resulting in reduced heat sink weight and volume. Improved switching performance impacts the main power switches by reducing the stress on them and improving the system performance. SiC Schottky diodes are already commercially available at relatively low current ratings. These diodes are being used in niche applications such as power factor correction circuits. It is expected that the first impact of SiC devices in inverters will be as a result of SiC Schottky diodes replacing the Si pn diodes.

Several problems must be addressed to meet the Department of Energy's (DOE's) FreedomCAR and Vehicle Technologies program goals, such as reducing the size and weight of the power electronics and cooling systems and increasing their efficiency**.** To evaluate the possibility of solving some of these problems using SiC diodes, Oak Ridge National Laboratory (ORNL) collaborated with Cree and Semikron to build a hybrid 55-kW (Si IGBT–SiC Schottky diode) inverter by replacing the Si pn diodes in Semikron's inverter with Cree's SiC Schottky diodes.

3.3 TESTING AND MODELING THE 75-A DIODE

For SBDs, the two main tests that need to be performed are testing the static characteristics, consisting of i-v curves, and turn-off testing, from which the reverse recovery of the diode can be evaluated.

3.3.1 SiC SBD On-State Testing

SBDs from Cree rated for 75 A were tested in the TEK 371B curve tracer to obtain the on-state characteristics over a range of temperatures (–55°C to 175°C). The diode was placed in an oven (connected through high-temperature wires) to evaluate the temperature characteristics. Since this is a high-current device, the voltage drops across the connecting wires become significant. The resistance was found to be 0.073 Ω, and corresponding voltage drops across the wires were subtracted from the raw data, thereby yielding the true voltage drop across the diode.

As seen in Fig. 3.1, the built-in potential (or the knee voltage) decreases with the increase in temperature because the increasing thermal energy of electrons in the metal overcomes the Schottky barrier height at a lower forward voltage. It can also be seen that there is a decrease in the slope of the on-state characteristics with a temperature increase. This is because of the reduction in mobility, or increase in on-resistance, that is typically seen in a majority-carrier device and is a sign of a positive-temperature coefficient.

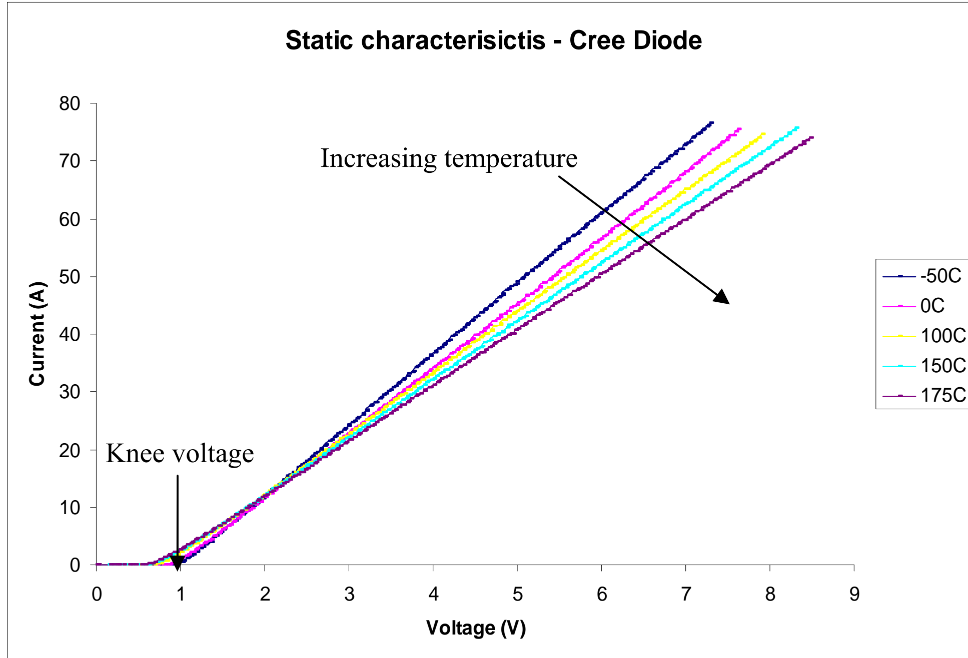

Fig. 3.1. i-v characteristics of the 75-A SiC diode from Cree.

3.3.2 SiC Diode Modeling

The SiC diode model used in this project was developed at the University of Arkansas. It is a robust model that can accurately model forward and reverse recovery accurately over temperature. Moreover, many details pertaining to the fabrication of the diode need not be known by the user, making parameter extraction flexible. Figure 3.2 shows the topology of the SiC power-diode model.

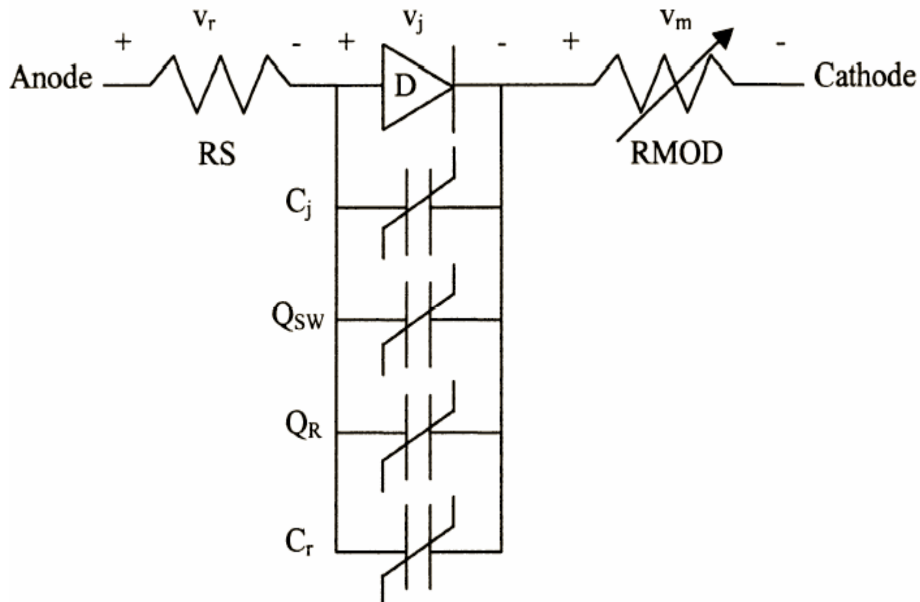

Fig. 3.2. Model topology of the power diode [18].

The model described is a "unified" one in that it can model pn, Schottky, and merged pn–Schottky diodes. Therefore, all the features will not be turned on for modeling the Schottky diode for this research effort. Some of the variables seen in Fig. 3.2 do not pertain to Schottky diodes and are therefore not explained.

For modeling the static characteristics, the diode uses several equations of the form

$$i = IS(e^{\frac{V_j}{N \cdot V_T}} - 1) \;, \tag{3.1}$$

where IS is the saturation current, V_j is the forward diode junction voltage, N is the emission coefficient, and V_T is the thermal voltage (kT/q). There are different regions in the diode operation, such as high- and low-level injections and recombination, all of which are modeled with similar equations. Moving boundary conditions are used to model the dynamic characteristics such as turn-on, turn-off, and reverse recovery.

To incorporate temperature effects, Eq. (3.1) is altered as follows

$$IS(T) = IS(TNOM) \cdot (T/TNOM)^{XTI} \cdot e^{[(T/TNOM)-1] \cdot (EG/NT.VT)} \;, \tag{3.2}$$

where T is the user defined temperature, $TNOM$ is room temperature, and XTI is the temperature compensation factor.

Such normalized temperature-based factors are used in all the equations that need to scale with temperature.

3.3.3 Parameter Extraction and Model Validation Using the Characterized Data for Diodes

The model was constructed in MAST HDL and simulated in the Saber simulator. The dc test-bench consists of a constant dc source connected to the SiC diode model. The physical and structural parameters of the diode are first determined at the nominal temperature. The P-N grading coefficient, M, is set to the default value of 0.5. The parameters RS (series resistance), ISR (low-level recombination saturation current), and NR (low-level recombination emission coefficient) can be extracted from the forward on-state characteristics. For Schottky diodes, NR is typically set to 1. The forward series resistance, RS, can be obtained directly from the inverse of the slope of the on-state current versus the voltage characteristic at high to medium currents. After RS is extracted, the diode current versus internal-junction voltage ($V_j = V_D - I_D \cdot RS$) is calculated with the measured data. An I_D versus $V_{j\ \mathrm{semi}}$-log plot is then used to extract NR and ISR as follows

$$2.3\log I_D = 2.3\log ISR + 2.3V_j/(NR \cdot V_T) \;. \tag{3.3}$$

The y intercept of the semi-log plot gives the value of ISR. The temperature-dependent parameters are then extracted. The saturation current, ISR's temperature exponent $XTIR$, is extracted using the low forward current characteristic over a range of temperatures. The decrease in slope of the on-state characteristics as temperature increases is used to extract the parameters representing the temperature dependency of the series resistance RS. In other words, RS is extracted for each on-state curve for all temperatures. The values of the extracted RS for each temperature are then used in Eq. (3.4) to optimize the values of the exponential $GAMMA$, linear $TRS1$, and quadratic $TRS2$ temperature parameters for RS.

$$RS(T) = RS(TNOM) \cdot [(T/TNOM)^{\gamma} + TRS1(T-TNOM) + TRS2(T-TNOM)^2] \;. \tag{3.4}$$

After the parameters are extracted from the on-state characteristics, the depletion and package capacitance are then extracted from the reverse-recovery waveforms. For Schottky diodes, the absence of stored charge reduces the reverse recovery to just the charging of the depletion and package capacitances. After the diode current crosses zero, the voltage is seen to rise as the depletion and package capacitances are charged. The initial peak in the reverse recovery is due to the junction capacitance, as the depletion region is narrow and is accounted for in the model by *CJ0* and *FC* (forward bias-depletion capacitance coefficient); while the further increase in the negative reverse current as the diode voltage rises is due to the package capacitance (*CP*). At high voltages, the depletion region decreases, and therefore the package capacitance dominates. Therefore, *CP* is extracted from the high-voltage part of the reverse-recovery waveform. Care should be taken to ensure that the voltage waveforms from which *CJ0* and *CP* are extracted are aligned and have the same *dv/dt*.

3.4 SCHOTTKY DIODE AT DIFFERENT TEMPERATURES

The on-state validation of the model with the SiC 75-A diode from Cree is seen in Fig. 3.3. The percentage error is approximately 0.3–0.4% in the 100°C and 150°C curves and approximately 2–3% in the 25°C curve.

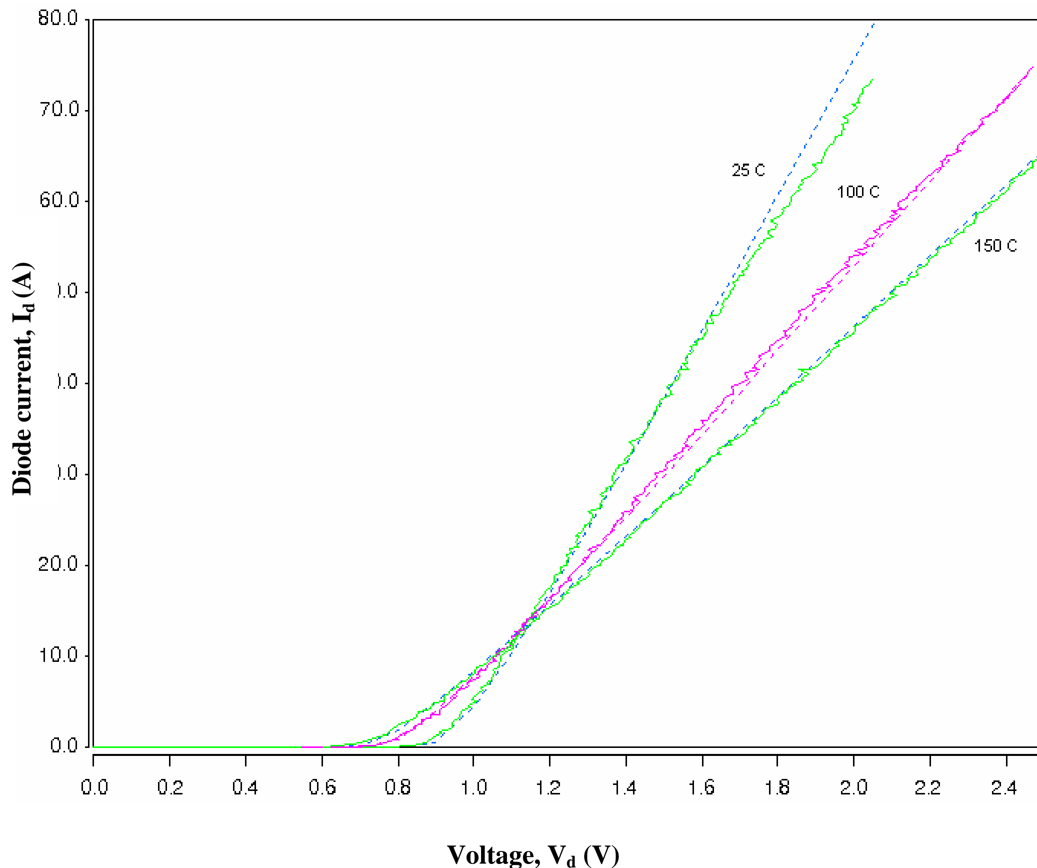

Fig. 3.3. Measured (solid) and simulated (dotted) on-state waveforms of the SiC Schottky diode at different temperatures.

Figure 3.4 shows the reverse recovery of the SiC diode and the corresponding behavior of the model (in dotted lines) with the extracted *CJ0* parameter. The model is accurately tracking the test data.

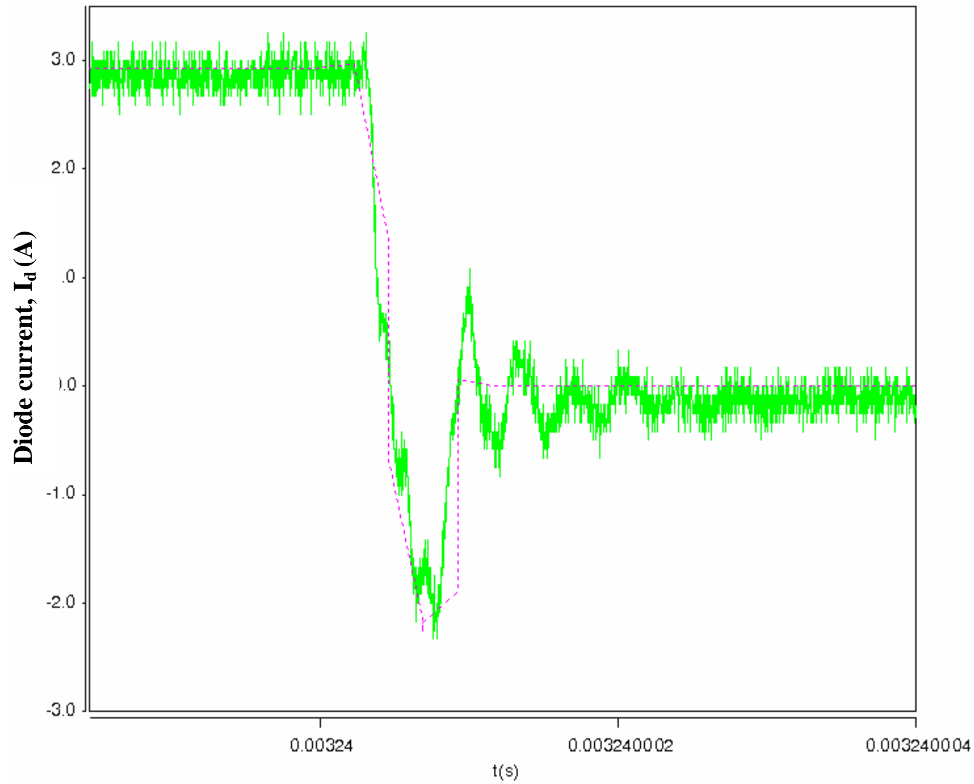

Fig. 3.4. Measured (solid) and simulated (dotted) reverse-recovery waveforms of the SiC Schottky diode from Cree.

The junction capacitance can then be extracted from the reverse-recovery data that essentially determines the switching speed and the peak-reverse-recovery current of the device. In Fig. 3.5, the effect of the junction capacitance can be seen on the reverse-recovery current. It can be easily deduced that the peak-reverse-recovery current is directly proportional to the diode-junction capacitance.

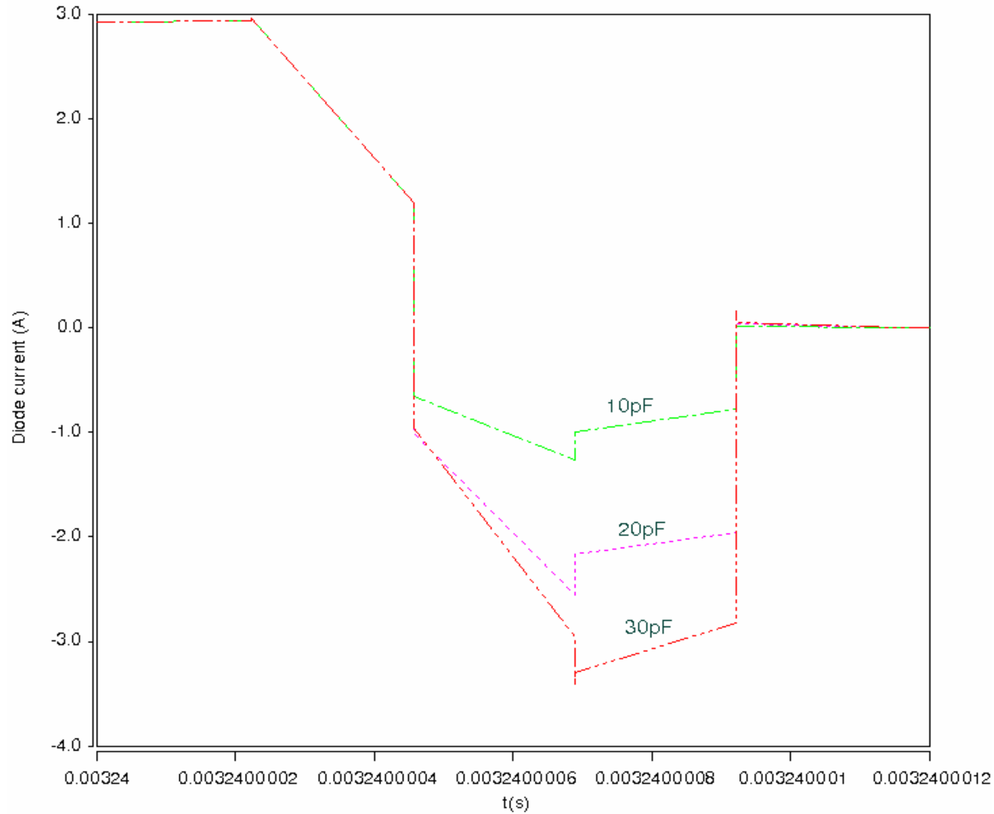

Fig. 3.5. Simulation showing the reverse-recovery current in a SiC diode for different values of junction capacitances.

3.5 SIMULATION OF Si IGBT–SiC SCHOTTKY DIODE HYBRID INVERTER

After the modeling and parameter extraction of the devices, the device models were used to construct a three-phase voltage-source inverter in Saber. The Saber Sketch software in the suite was used. The model closely emulated the prototype inverter from Semikron in terms of the inverter topology. The switching frequency was set to 10 kHz. Library models were used for the comparators, voltage sources, and passive elements. A graphical representation of the SiC Schottky diode model was created which can be interfaced directly with other library elements instead of manually creating net lists. The modulating sine wave had a frequency of 75 Hz, which was therefore the frequency of the output current. The IGBT that was used for constructing the Semikron inverter was not available in the Saber library. Therefore, another IGBT with similar ratings was used as the transistor switch instead. The load consisted of a 1.24-Ω resistor and a 1.5-mH inductor. The input dc bus voltage was set at 325 V. The inverter topology is shown in Fig. 3.6.

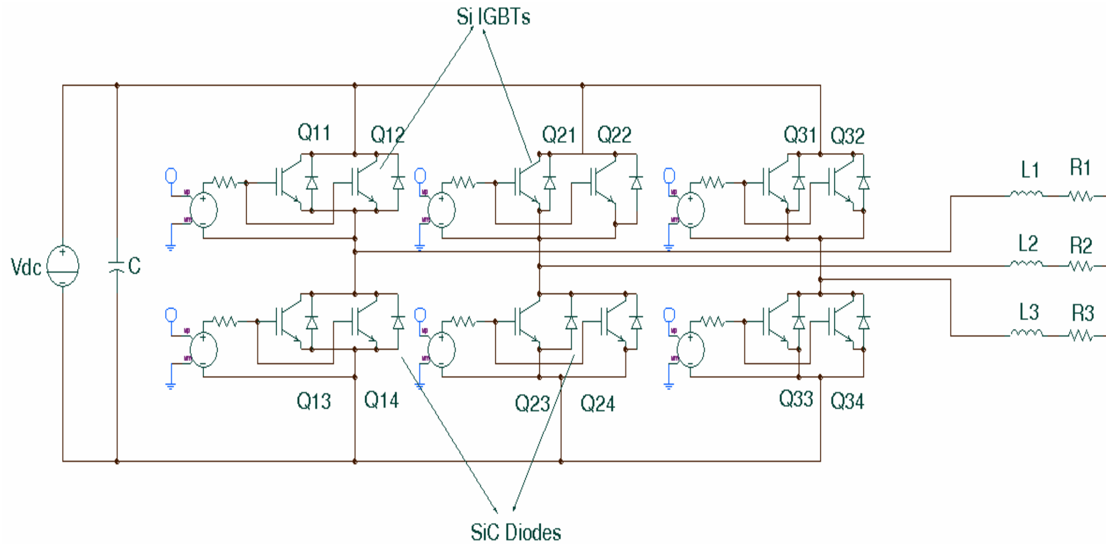

Fig. 3.6. Schematic representation of the hybrid inverter in Saber.

Table. 3.1. SiC power diode model parameters and extraction characteristics for the Cree 75-A diode

Parameter	Parameter name	Extraction characteristic	Value
EG	Bandgap	Device-specific	1.6
VJ	Built-in junction potential	Device-specific	1.5
CJ0	Zero-bias junction capacitance	Device-specific	20 pF
M	P-N grading coefficient	Device-specific	0.5
FC	Forward-bias deletion capacitance coefficient	Device-specific	0.5
NB	Base doping concentration	Device-specific	$1e^{15}$
RS	Forward series contact resistance	High- to medium-current on-state slope	0.013
ISR	Low-level recombination saturation current	Low-current on-state region	$5e^{-16}$
NR	Low-level recombination emission coefficient	Low-current on-state region	1
XTIR	*ISR* temperature exponent	Low-current on-state vs. T	3
TNR1	Linear *NR* temperature coefficient	Low-current on-state vs. T	0
TNR2	Quadratic *NR* temperature coefficient	Low-current on-state vs. T	0
TRS1	Linear *RS* temperature coefficient	High- to medium-current on-state slope vs. T	$-14e^{-3}$
TRS2	Quadratic *RS* temperature coefficient	High- to medium-current on-state slope vs. T	$-16e^{-6}$
GAMMA	*RS* temperature exponent	High- to medium-current on-state slope vs. T	2.5

An all-Si inverter with Si IGBTs and diodes was also simulated using the device parameters in Table 3.1. The load currents and a single-phase voltage from the simulations are shown in Figs. 3.7 and 3.8, respectively. The efficiencies of the inverter obtained during simulations are shown in Table 3.2. Table 3.3 shows the modulation index used and the resulting inverter efficiencies of the inverter. Note that the Si IGBT–SiC Schottky diode hybrid has much better efficiencies than the all-Si inverter.

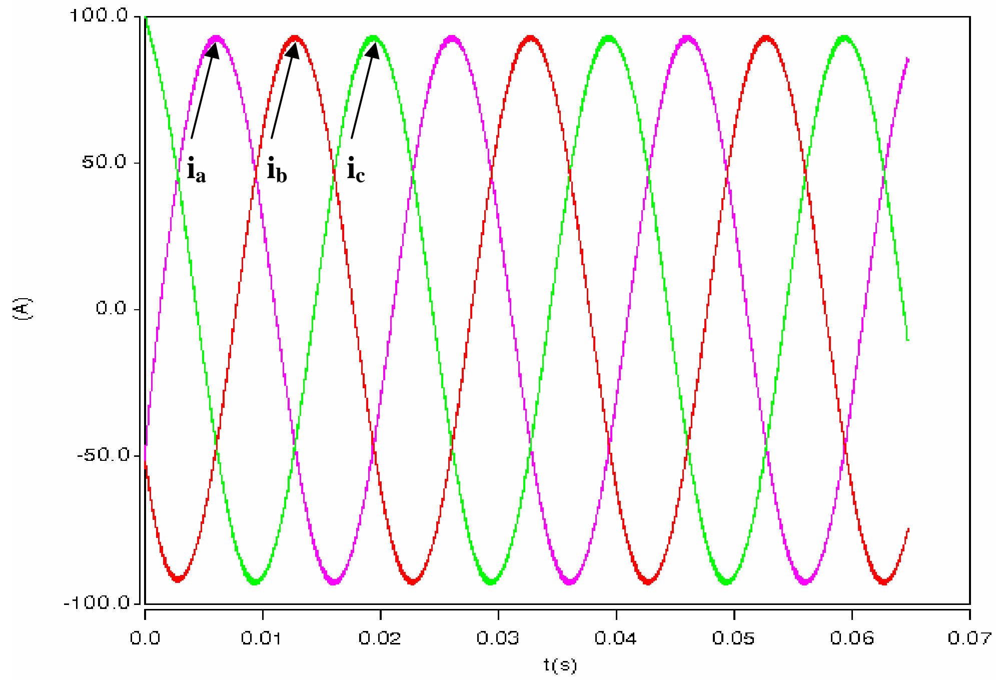

Fig. 3.7. Simulated three-phase load currents in the hybrid inverter.

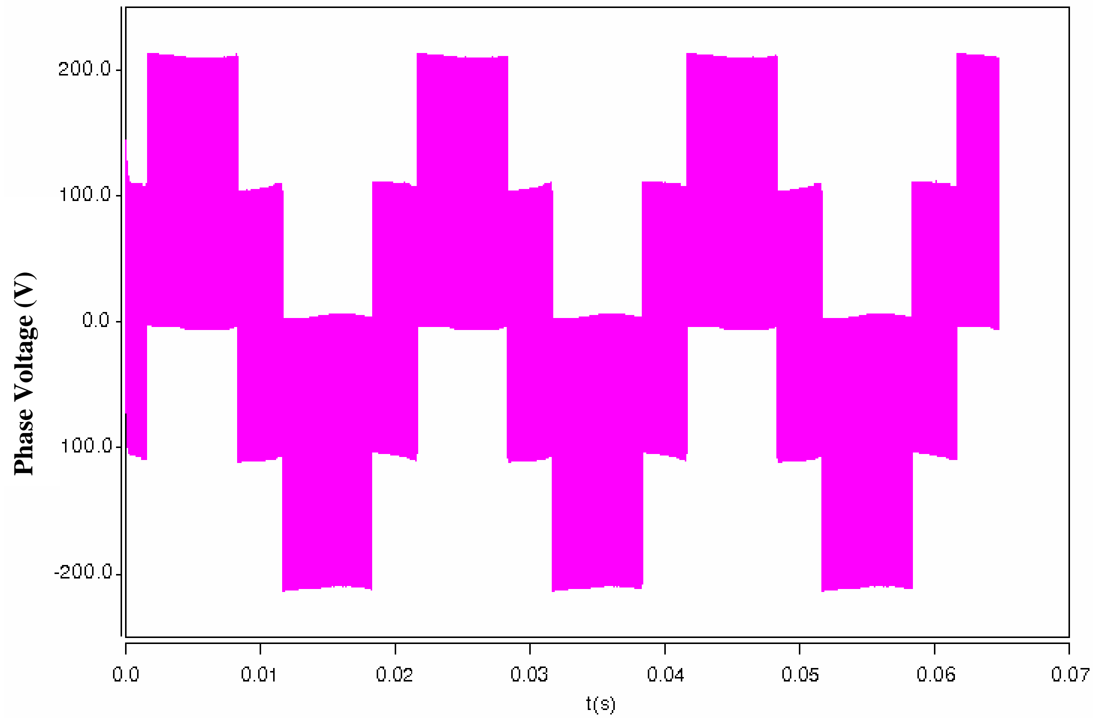

Fig. 3.8. Simulated phase voltage (phase 1) in the hybrid inverter.

Table 3.2. Efficiencies of the hybrid inverter obtained from simulation

Modulation index	Peak power output from simulation (kW)	Efficiency (simulation) percent
0.572671	41.65	93.54
0.700348	48.43	94.27
0.801846	54.97	95.15
0.899974	62.88	96.27
0.985006	68.92	97.36

Table 3.3. Efficiencies of the all-Si inverter obtained from simulation

Modulation index	Peak power output from simulation (kW)	Efficiency (simulation) percent
0.586299	40.33	92.07
0.710617	48.17	93.48
0.821163	54.43	94.41
0.910835	61.77	95.14
1.001043	68.09	96.53

The simulation and testing was performed for all conditions with a constant dc supply of 325 V. The instantaneous-power output from the inverter is shown in Fig. 3.9. The peak-power output can also be gauged from the output-power plot. The hybrid inverter was found to have a peak-instantaneous-power output ranging from 41–69 kW, depending on the amplitude modulation index. When the amplitude modulation index was set at 0.8, the peak-power output was found to be 55 kW.

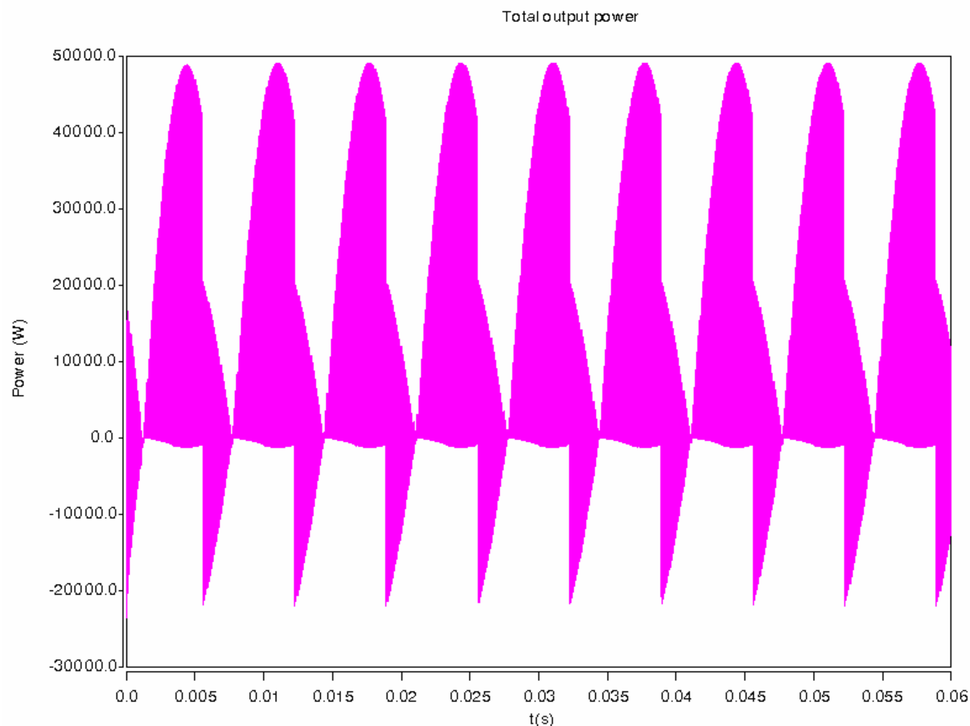

Fig. 3.9. Total instantaneous output power from the three phases of the hybrid inverter.

The difference in efficiencies between the simulated inverters is clearly visible in Figs. 3.10 and 3.11. When the Si diode in the all-Si inverter was replaced with the SiC Schottky diode, a 1.5–2% increase in the operational efficiency was observed.

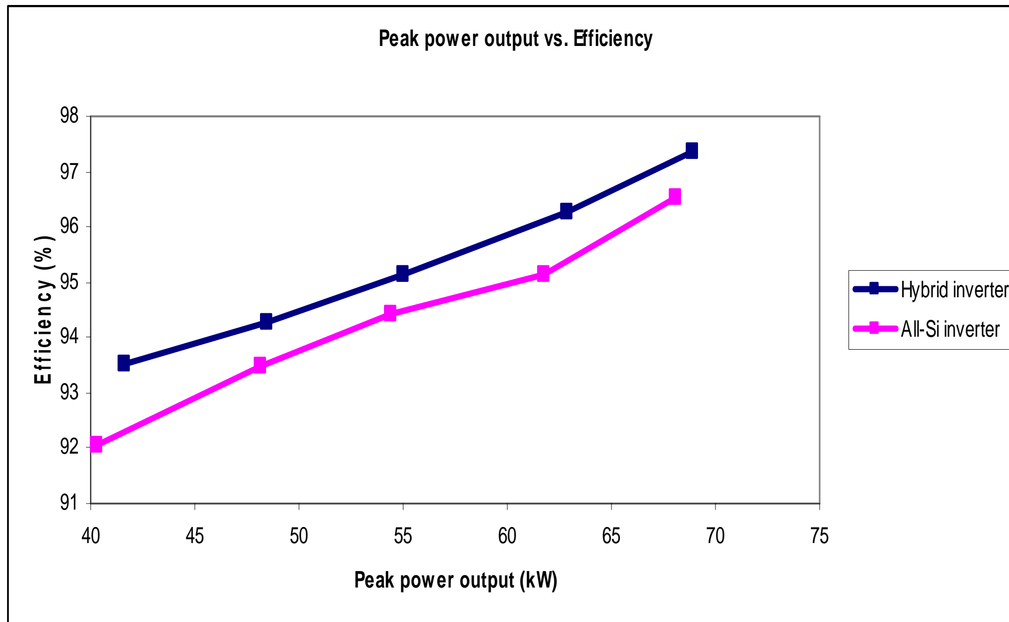

Fig. 3.10. Comparison of peak-power output vs. efficiencies for hybrid and all-Si inverter.

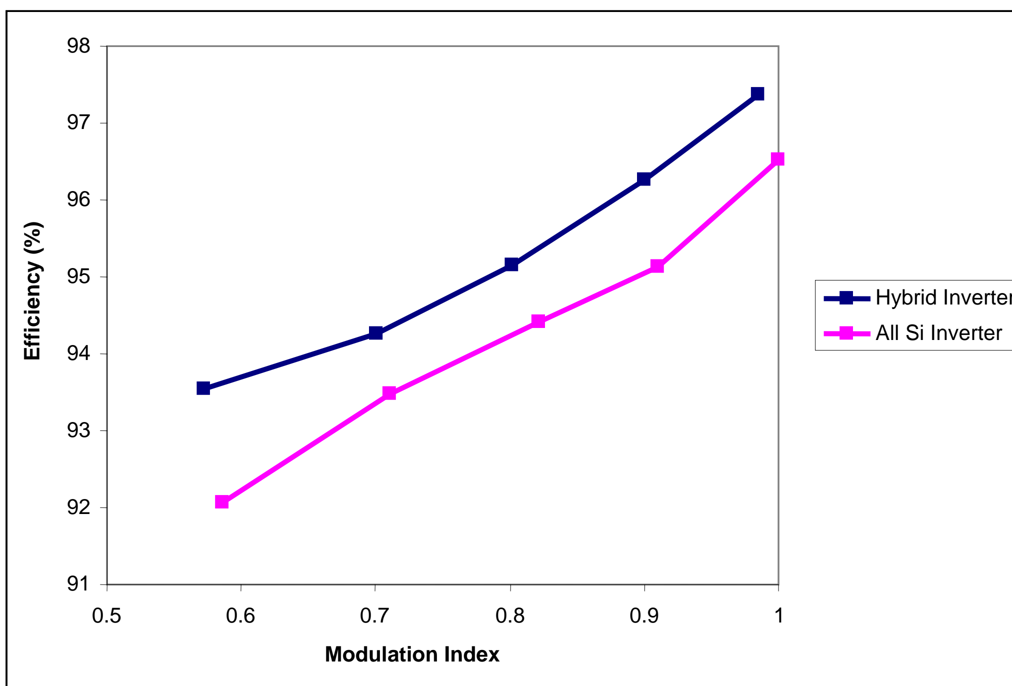

Fig. 3.11. Comparison of efficiencies (from simulation) of hybrid and all-Si inverter.

3.6 CONFIGURATION OF THE INVERTER

The inverter module SKAI (Semikron Advanced Integration) from Semikron was developed for hybrid electric vehicle traction drives. It is a three-phase 55-kW inverter unit (Figs. 3.12 and 3.13) built using 600-V, 600-A IGBT and 600-V, 450-A pn diode modules. Cree has developed 75-A, 600-V, 4 × 6.65m SiC Schottky diodes as shown in Fig. 3.14. The 3–in. wafer is also shown in Fig. 3.14. The yield for the wafer was about 46.7%, with 67 good devices from the wafer. Semikron has replaced each Si pn diode (9 × 9mm) in its automotive integrated power module (AIPM) with two 75-A SiC Schottky diodes.

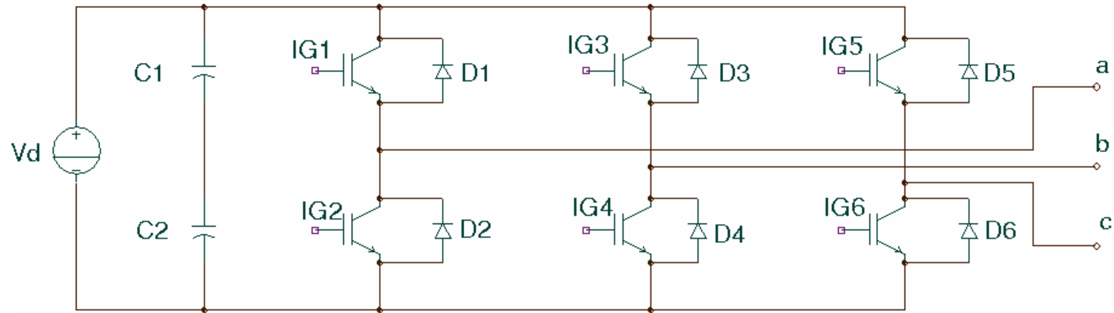

Fig. 3.12. Inverter topology.

Fig. 3.13. Semikron inverter unit.

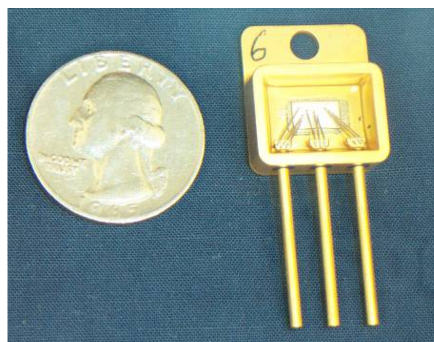

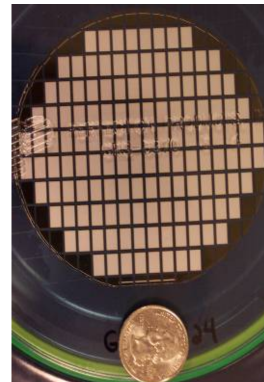

Fig. 3.14. 75-A Schottky diodes developed by Cree.

The inverter is liquid-cooled with a recommended coolant-flow rate of 2.5 gal per minute (gpm). The Semikron unit shown in Fig. 3.13 is roughly rectangular in shape, but it has irregular dimensions and weighs approximately 17 lb (7.7 kg). The maximum length, including mounting flanges and hose connections, is 17.6 in. (449 mm). Excluding the mounting flanges and hose connections, the unit measures 16.1 in. (410 mm). The maximum width of the unit is 8.2 in. (210 mm) and the minimal width is 7.2 in. (185 mm). The maximum height of the unit is about 4 in. (100 mm). The volume of the unit is approximately 6.9 L. The unit has built-in current sensors and dc-link capacitors. It has a CAN bus interface with a built-in digital signal processor (DSP) controller and gate drivers.

The control system implemented uses indirect field-oriented control techniques with a closed-current loop feedback. The speed and torque controls are achieved by a space vector pulse-width modulation (SVPWM) control scheme with current and speed as feedback parameters. A control-system block diagram is shown in Fig. 3.15 [19]. The control firmware module was provided by Semikron with user interface software as shown in Fig. 3.16. Different modes of operation are possible with the controller.

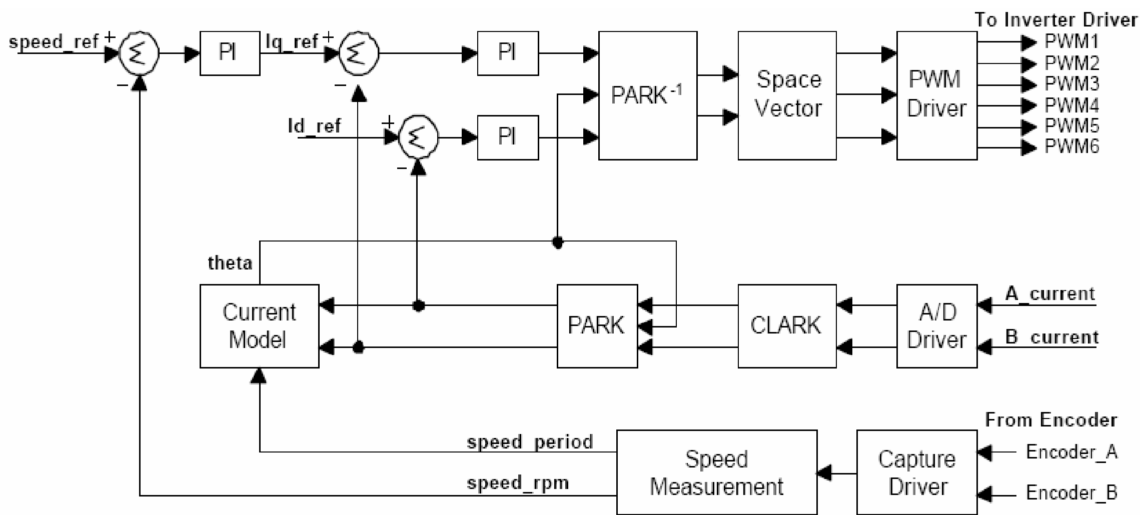

Fig. 3.15. Block diagram of the control system.

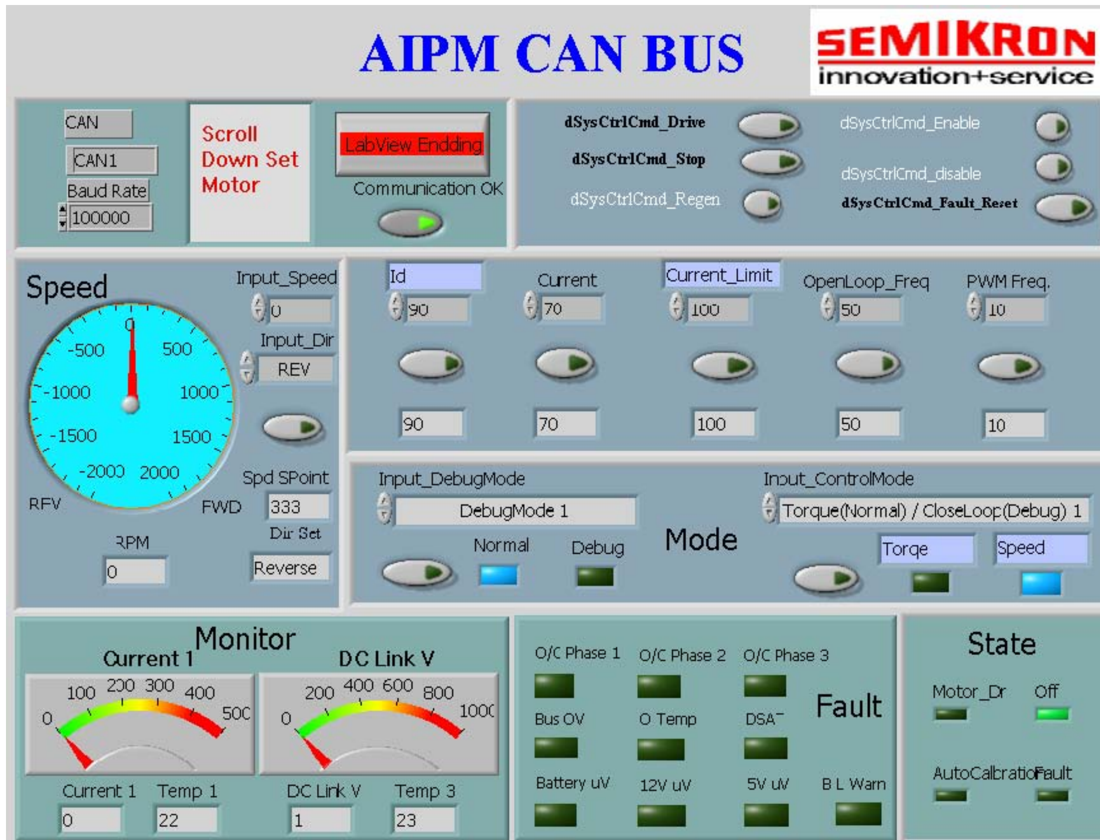

Fig. 3.16. A screen shot of the user interface software.

3.6.1 Normal Mode

The controller operates as a closed-loop system and has two control modes

- Speed mode
- Torque mode

3.6.2 Debug Mode

The controller operates as an open-loop system, and the pulse-width modulation (PWM) frequency and the open-loop frequency can be adjusted. There are several user control parameters that can be accessed through the software interface to set the values for different operating conditions. A fault monitoring system provides protection to the system from faults such as over-current, bus over-voltage, over-temperature, and desaturation.

3.7 INVERTER TESTING

There are two major tests to be performed, an R-L load test to evaluate the inverter's power handling capability and the dynamometer test for dynamic performance. Both the hybrid inverter and the all-Si inverter were tested with the same procedure. As discussed in the previous section, the modes of operation were controlled using the manufacturer-supplied user interface software. The inverter efficiency curves were obtained using the speed mode of operation, and the power handling capability was tested

using the debug mode of operation. The coolant temperature of the inverter was varied (20–70°C) to stress the wire bonds and bond joints in the inverter and to test for strength.

3.7.1 Isolation Impedance

As a safety measure, prior to the start of electrical testing, the unit was checked for a fault condition that could have occurred as a result of shipping or handling damage. The isolation impedance between the inverter terminals and case was measured with a multi-meter to verify proper isolation. The isolation impedance between the terminals and case of the inverter was measured as being greater than 1 MΩ.

3.7.2 R-L Load Test

3.7.2.1 Test setup

The output leads of the inverter are connected to a three-phase star-connected variable resistor bank with a three-phase inductor in series. The dc inputs are connected to a voltage source capable of supplying the maximum rated operating voltage and current levels for the inverter. The test setup uses the following equipment, as shown in Fig. 3.17.

- Yokogawa PZ4000 power analyzer for power measurement.
- Variable resistor load with a capacity of 24 kW.
- Inductor with 400-A capacity.
- Coolant pump with a temperature controller.
- A dc power supply with four-quadrant operation (not seen in the figure).

3.7.2.2 Operation

During this test, the inverter unit was operated in the debug mode instead of the normal mode. In this mode, the open-loop frequency and the PWM frequency can be adjusted and the power capability of the inverter can be tested.

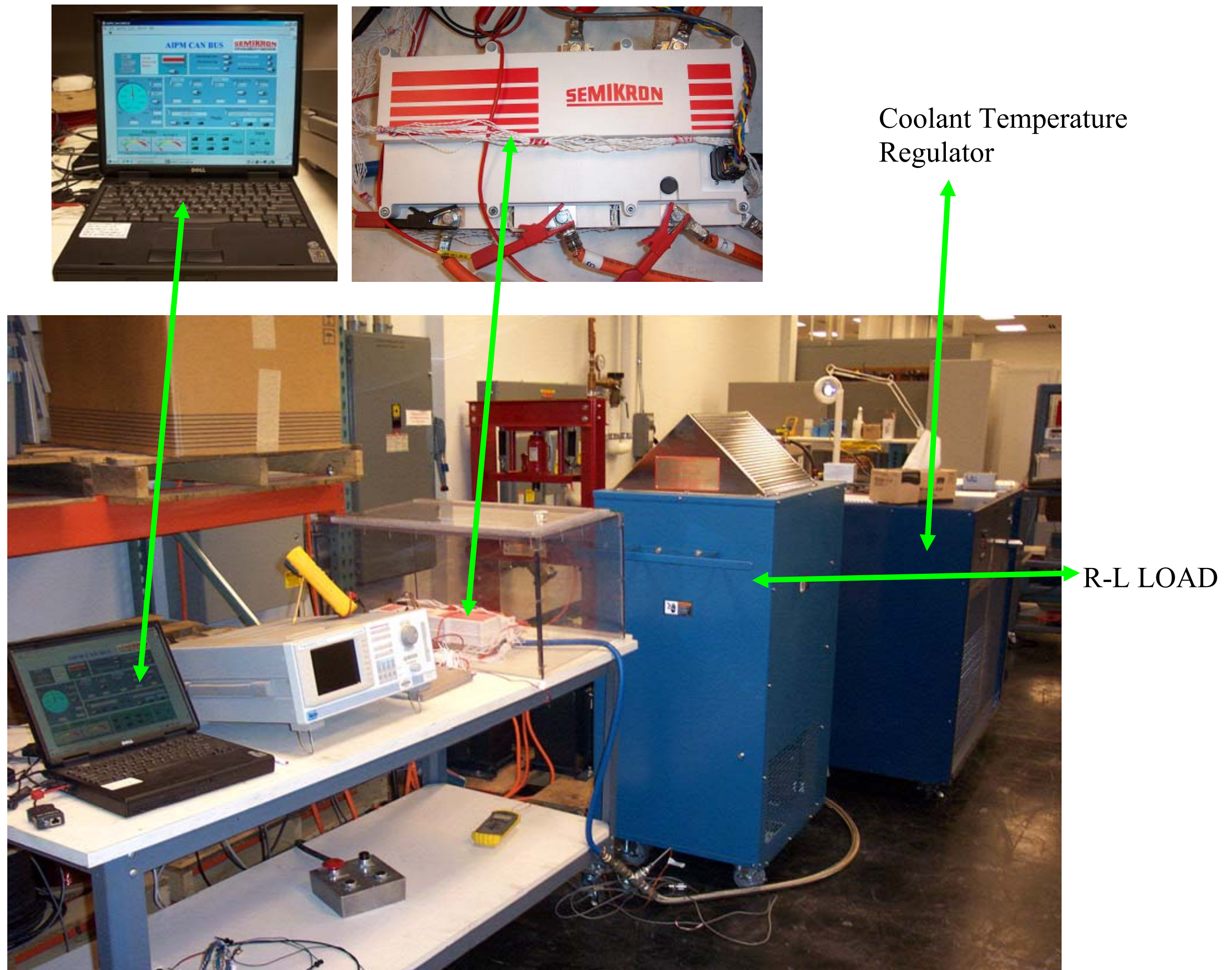

Fig. 3.17. R-L load test setup.

For this test, the dc-link voltage was varied from the minimum operating voltage (200 V) to the maximum bus voltage (450 V). The bus voltage trip fault occurs for voltages beyond 450 V. The load resistance was set to the minimum value, and the current was controlled using the current controller. The coolant was set at 20°C and at a flow rate of 2.5 gpm. The open-loop frequency of operation and the PWM frequency were fixed, and the current command was varied for a particular dc-link voltage. For each value of the current command and open-loop frequency, the dc-link voltage, dc-link current, input power, output power, efficiency, and output-line currents and voltages were recorded. The three-phase power was measured using the two-wattmeter method. The command current was increased in steps of 10 A without exceeding the power rating of the inverter or the power rating of the load.

The procedure was repeated by increasing the open-loop frequency in steps of 25 Hz. The coolant temperature was changed to 70°C, and the data were recorded for a wide range of current and open-loop frequencies.

3.7.2.3 Results

The operating waveforms for two specific operating conditions of one phase of the hybrid inverter are shown in Fig. 3.18. The data obtained for both the inverters were analyzed and the corresponding efficiencies were calculated. The efficiency versus output-power plots for several operating conditions comparing the inverters are shown in Fig. 3.19 (a) and (b). The hybrid inverter efficiencies are higher than the all-Si inverter efficiencies for all operating conditions. The results show a reduction of up to 33.6% in the losses when everything is kept the same and SiC Schottky diodes are used instead of Si pn diodes. The percentage of loss reduction was calculated by comparing the power losses between the hybrid inverter and the all-Si inverter as follows:

$$\text{Percentage loss reduction} = \left(d_{ploss(Si)} - d_{ploss(SiC)}\right)/\left(d_{ploss(Si)}\right) \times 100$$

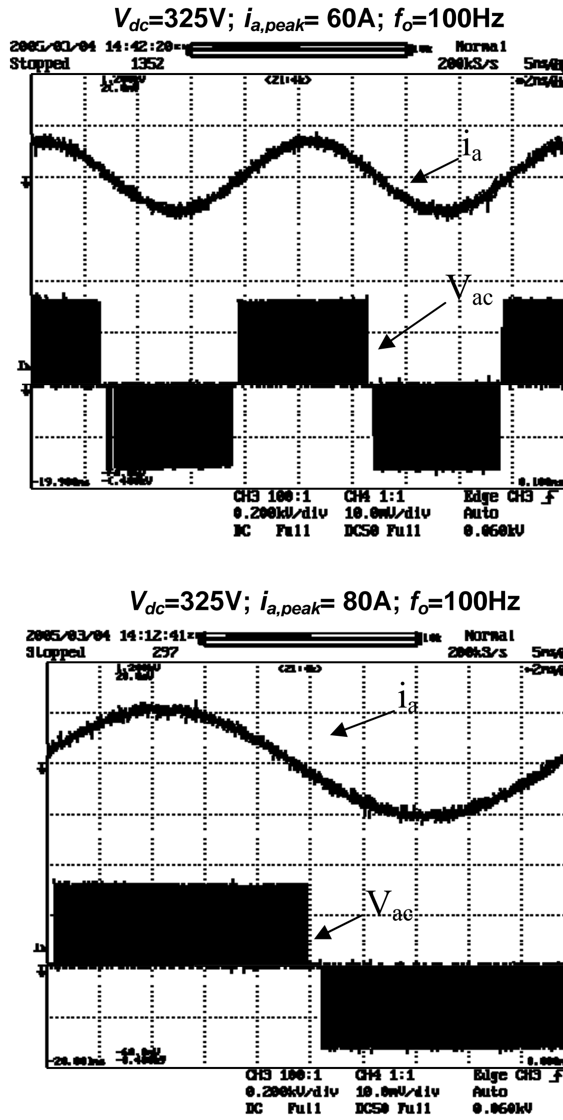

Fig. 3.18. R-L load test operating waveforms.

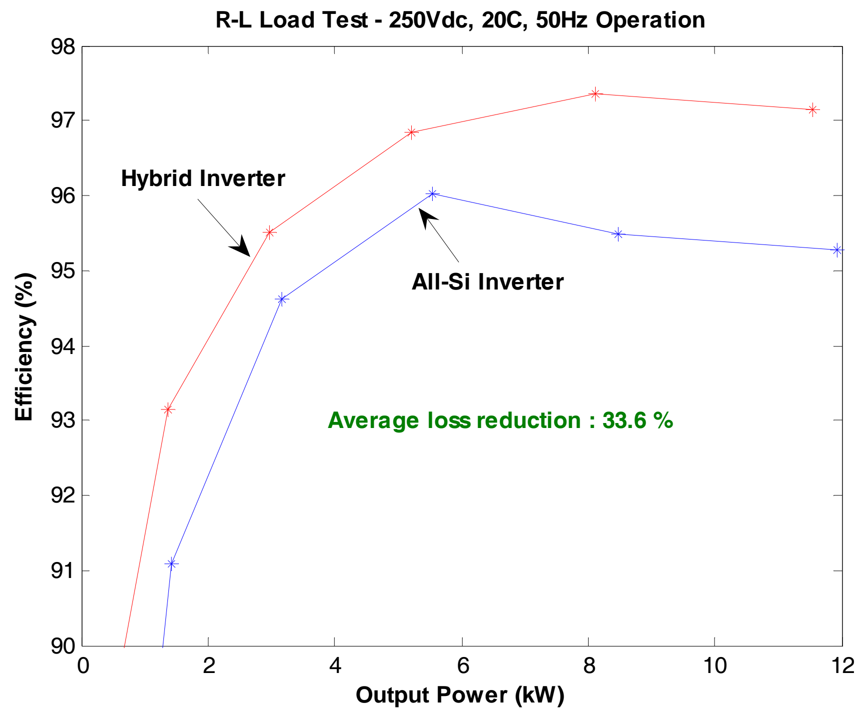

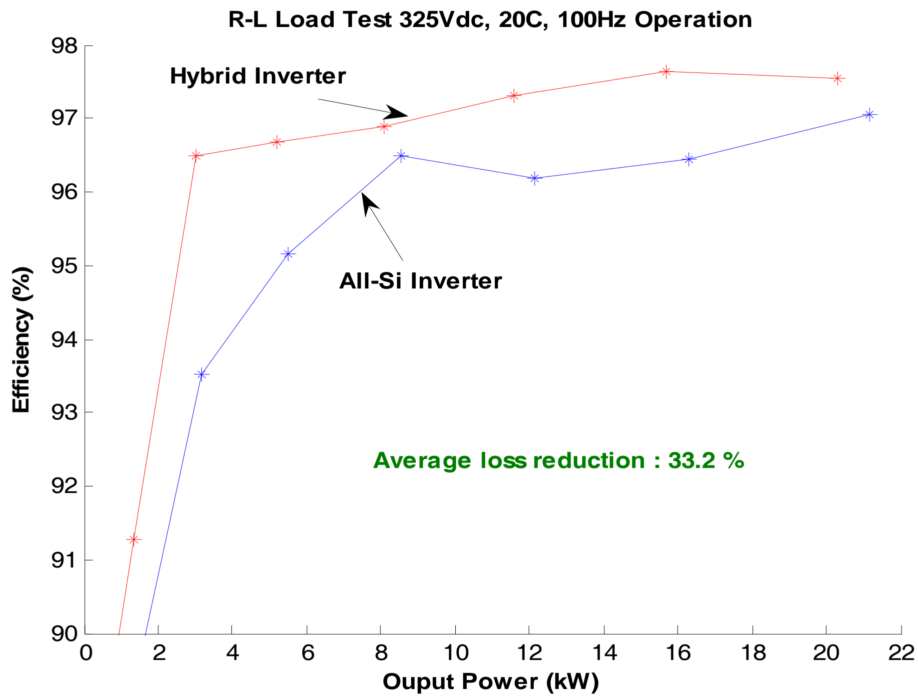

Fig. 3.19. R-L load test efficiency curves for various load conditions.

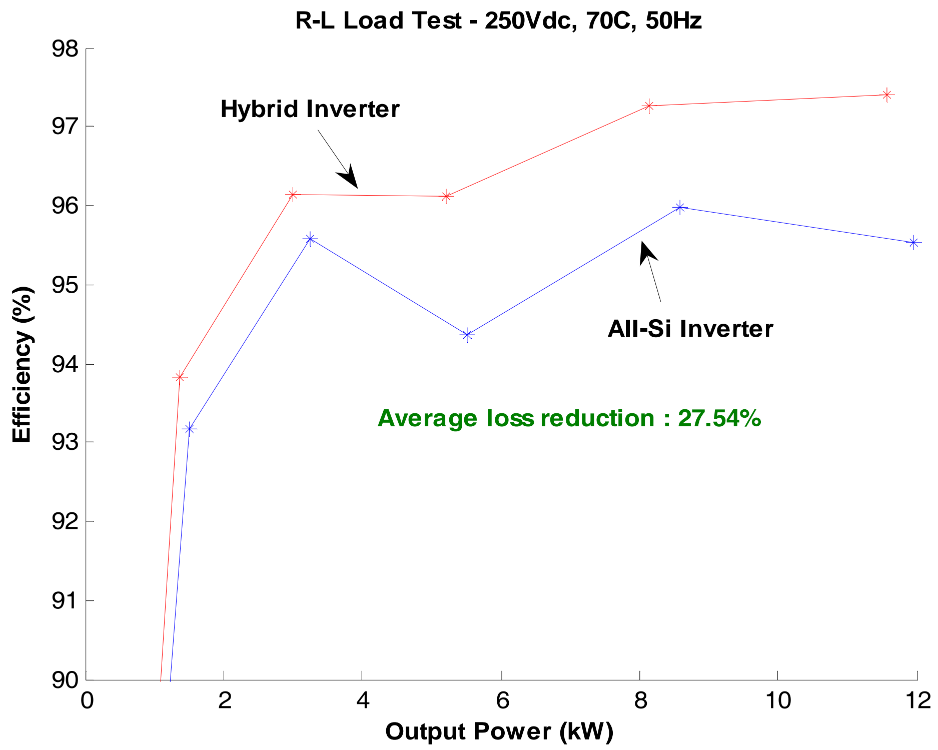

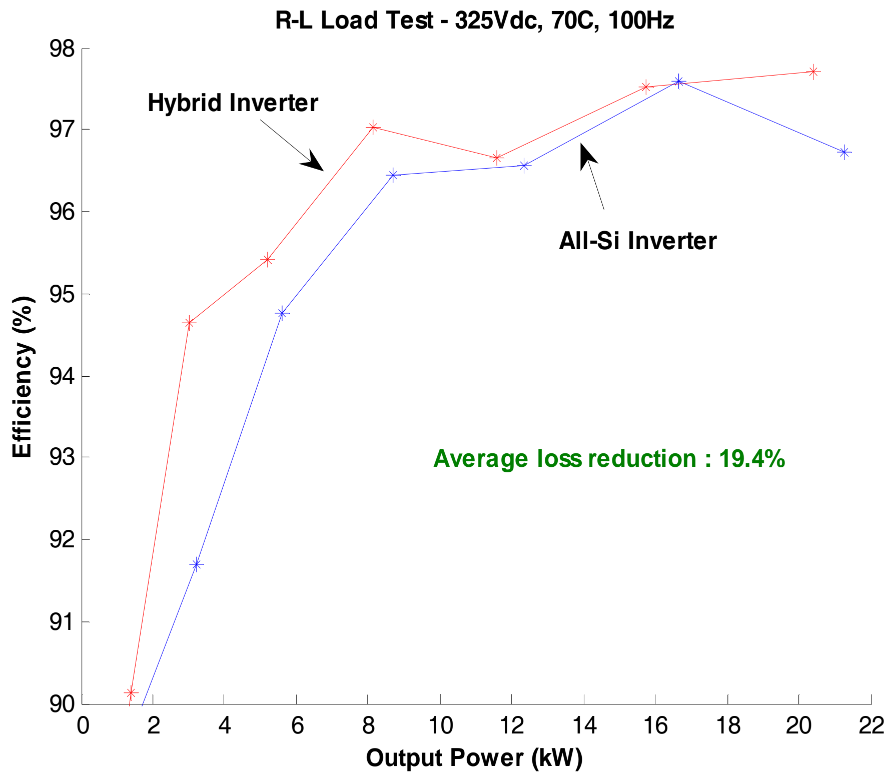

Fig. 3.19. R-L load test efficiency curves for various load conditions (cont'd).

3.7.3 Dynamometer Test

3.7.3.1 Test setup

The inverter was connected to a Solectria motor and setup in a dynamometer test cell to test the dynamic performance of the inverter in the motoring and regeneration modes. The Solectria motor is a four-pole induction motor with a base speed of 2500 rpm, and the dynamometer has 100-hp capacity. The setup is shown in Figs. 3.20 and 3.21. The tests were performed with the inverters supplied with 70°C coolant at a flow rate of 2.5 gpm.

Fig. 3.20. Inverter dyne test setup.

Fig. 3.21. 100-hp dyne cell.

3.7.3.2 Motoring mode

The test setup connections were verified in the test cell. During this test, the inverter unit was operated in the normal mode instead of the debug mode, and the control mode was set to speed instead of torque. In this mode, the speed set point, the magnetizing current, the direction of rotation, and the current limit were adjustable parameters. The dc-voltage input to the inverter was set at the nominal battery operating voltage (325 Vdc).

The closed-loop speed controller gains were adjusted for a given magnetizing current value and current limit to achieve stable operation of the system for a wide range of speeds. The direction of rotation was set to forward, and the motor speed was increased from 750 rpm to the rated base speed for a specific continuous-load torque. The data were obtained for a wide range of speed and torque values by changing the load torque (from 100, 150, 200 Nm) using the dynamometer controller. The following information was recorded at each speed increment: motor shaft speed (rpm and rad/second); motor torque; input voltage and current to the inverter; and output voltages and currents from the inverter. The output voltage and current waveforms for 40% and 80% of rated speed and several load-torque values were obtained.

The waveforms for two different loads are shown in Fig. 3.22. The efficiency plots for various speeds and load-torque values are shown in Fig. 3.23. The average loss reduction in motoring mode was up to 10.7%. The difference in the efficiencies of the inverters is higher at low-load torque because the diodes conduct for relatively longer periods. The reduction in losses becomes smaller at higher-load torques as the conduction time of the power switches increases. Note that one of the reasons the average loss reduction is less in the motoring than in the R-L load test is that the power levels achieved are much lower in motoring.

Figure 3.24 shows a screen shot of the test data obtained from the power meter PZ4000 for one of the operating conditions.

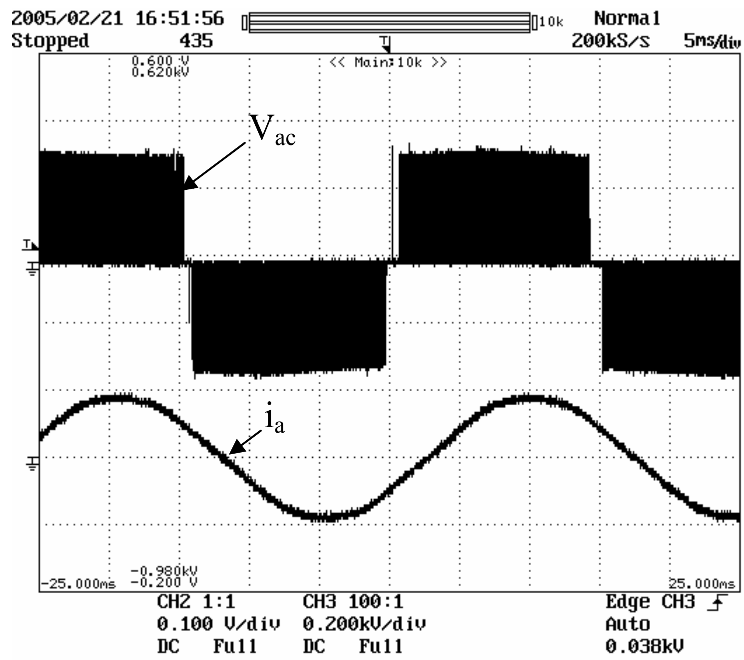

(a) 1000 rpm and 50 Nm.

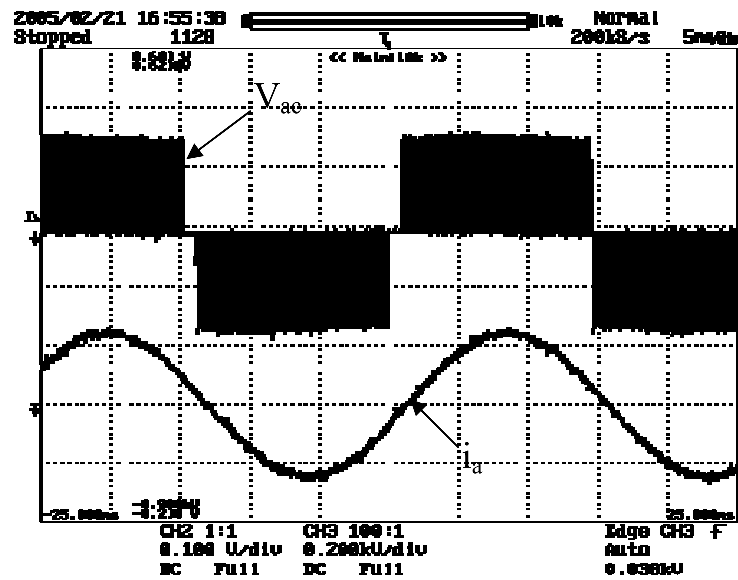

(b) 1000 rpm and 150 Nm.

Fig. 3.22. Dynamometer test–motoring mode operating waveforms.

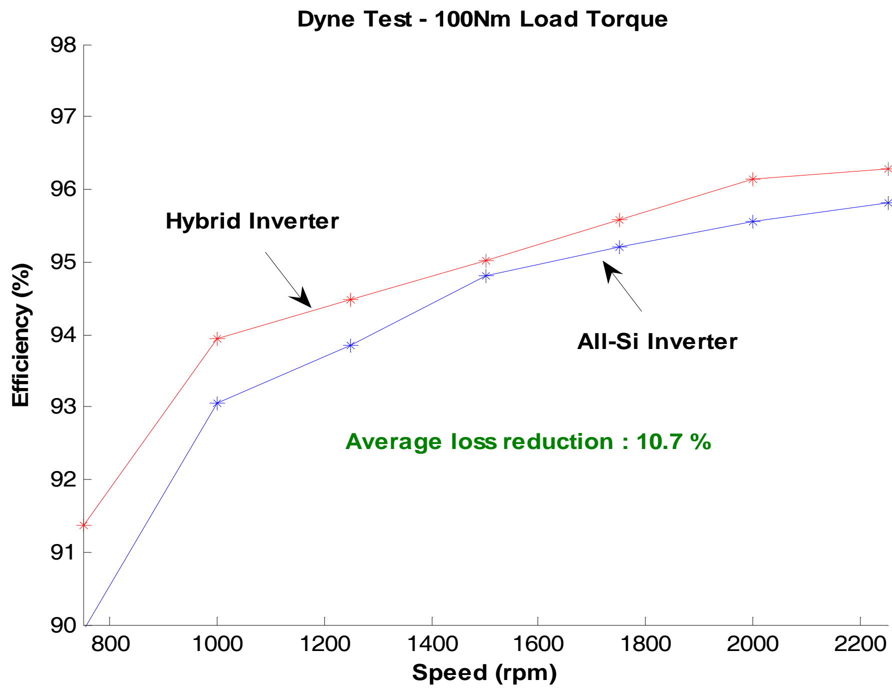

(a) 100 Nm load torque.

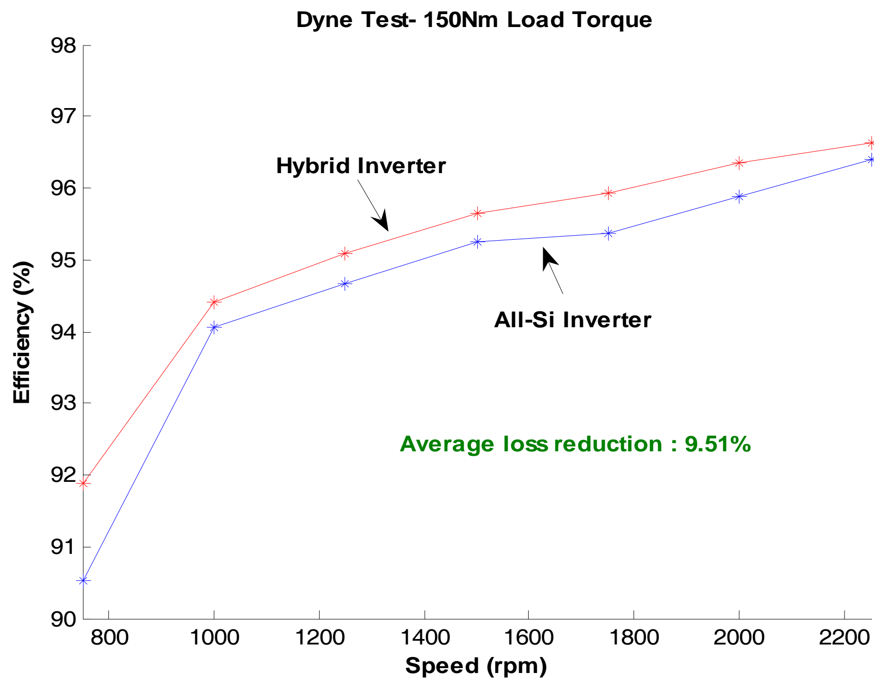

(b) 150 Nm load torque.

Fig. 3.23. Dynamometer test–motoring mode efficiency plots at 70°C.

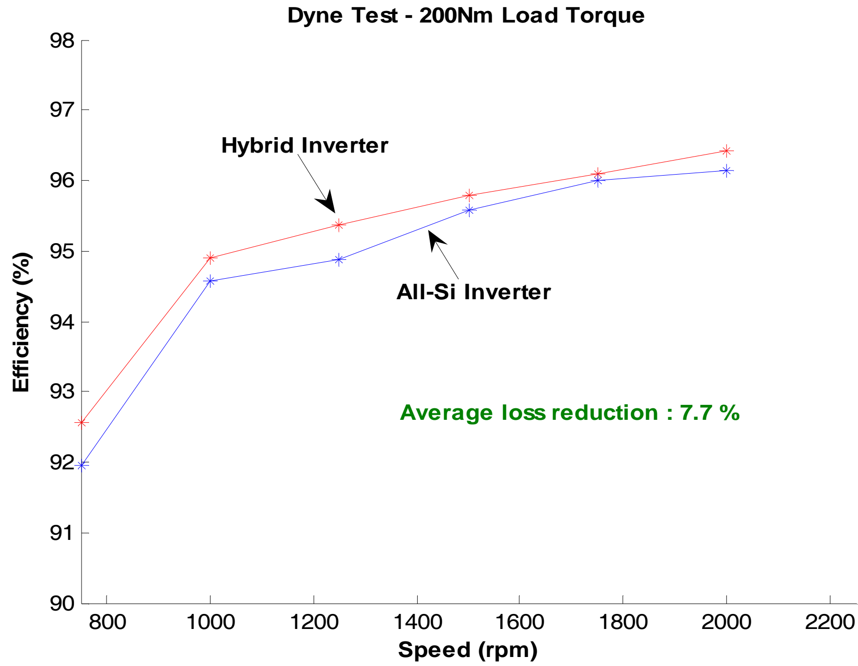

(c) 200 Nm load torque.

Fig. 3.23. Dynamometer test–motoring mode efficiency plots at 70°C (cont'd).

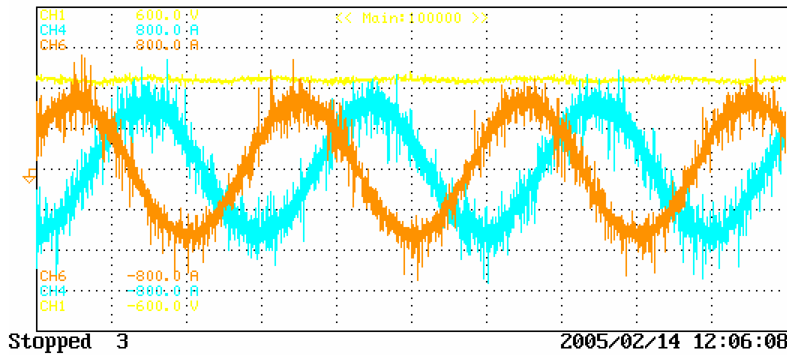

	Element1	Element2	Element3	Element4	Σ A	Σ B
Urms[V]	329.07	172.84	174.31	0.00	329.07	173.58
Umn [V]	365.49	103.22	104.55	0.00	365.49	103.88
Udc [V]	329.05	1.61	-10.86	0.01	329.05	-4.63
Uac [V]	3.82	172.84	173.97	0.00	3.82	173.40
Irms[A]	23.63	224.52	230.34	0.00	23.63	227.43
Imn [A]	22.16	222.83	227.55	0.00	22.16	225.19
Idc [A]	19.05	-1.24	-38.11	0.16	19.05	-19.68
Iac [A]	13.98	224.52	227.17	0.00	13.98	225.84
P [W]	6.27k	-8.29k	12.45k	-0.00k	6.27k	4.16k
S [VA]	7.78k	38.81k	40.15k	0.00k	7.78k	68.38k
Q [var]	4.60k	37.91k	-38.17k	0.00k	4.60k	-0.26k
λ [ ]	0.8058	-0.2135	0.3100	Error	0.8058	0.0609

Fig. 3.24. Dynamometer test–motoring mode data obtained from the power meter.

3.7.3.3 Regeneration mode

During this test, the inverter unit was operated in the normal mode instead of the debug mode, and the control mode was set to torque instead of speed. With these settings, the torque limit and the operating current can be adjusted. The dc-voltage input to the inverter was set at the nominal battery-operating voltage (325 V). The direction of rotation was set to be forward. The dynamometer controller was adjusted to control the speed. The motor speed was increased from 750 rpm to the rated speed for a specific operating current of the inverter to achieve a specific load torque. The current was varied from zero to the values corresponding to different torque values and then decreased to zero. The procedure was repeated to obtain the data for a wide range of speed and torque values. At each speed increment, motor-shaft speed (rpm and rad/second), motor torque, input voltage and current to the inverter, and output voltages and currents from the inverter were recorded. The output voltage and current waveforms for 40% and 80% of rated speed and several load-torque values were obtained. The operating waveforms for the regeneration mode are shown at two different speeds in Fig. 3.25. The curves comparing the efficiency of the inverters at 70ºC coolant temperature are shown in Fig. 3.26 (a–c). The results show a reduction of up to 12.71% in average losses, similar to the results obtained in the motoring mode.

The IGBTs used in the actual inverter and in the simulation are not the same. Therefore, a direct comparison of the efficiencies of the simulation and the testing would not be accurate. But it is seen that the efficiencies of the simulation and the testing do have the same trend.

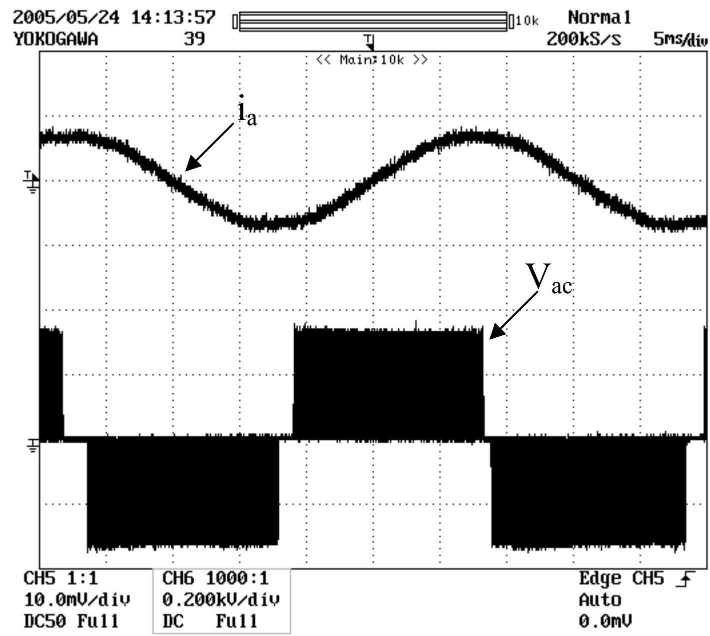

(a) 1000 rpm and 50 Nm.

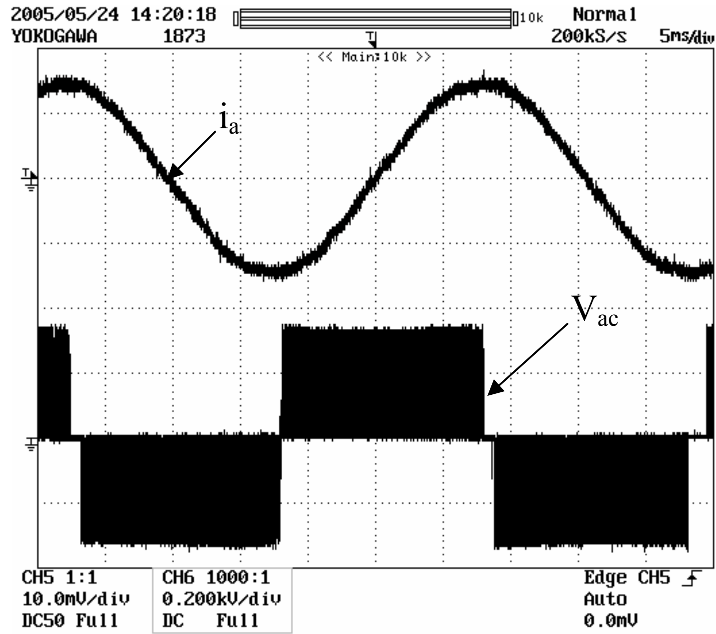

(b) 1000 rpm and 150 Nm.

Fig. 3.25. Dynamometer test–regeneration mode operating waveforms.

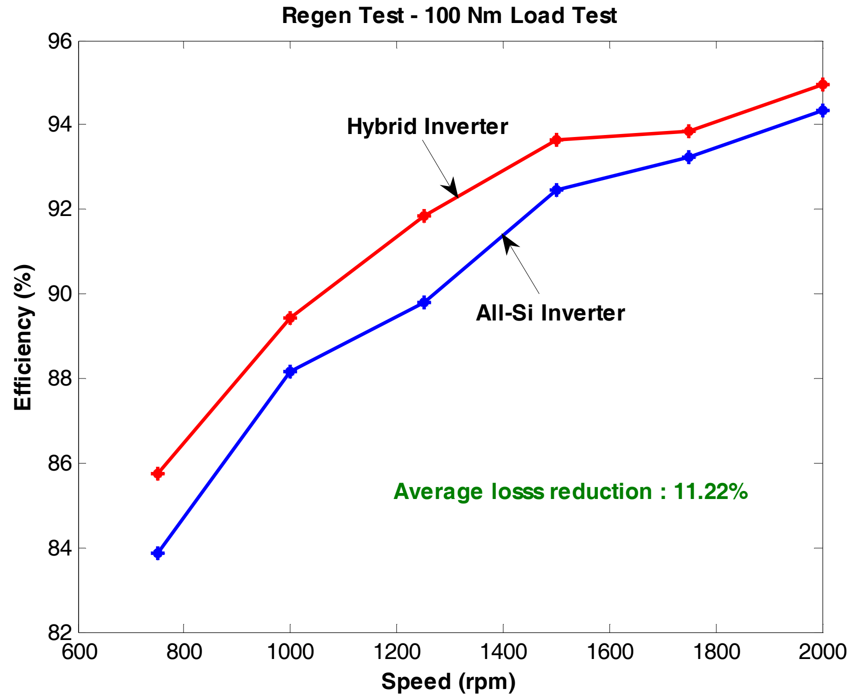

(a) 100 Nm load torque.

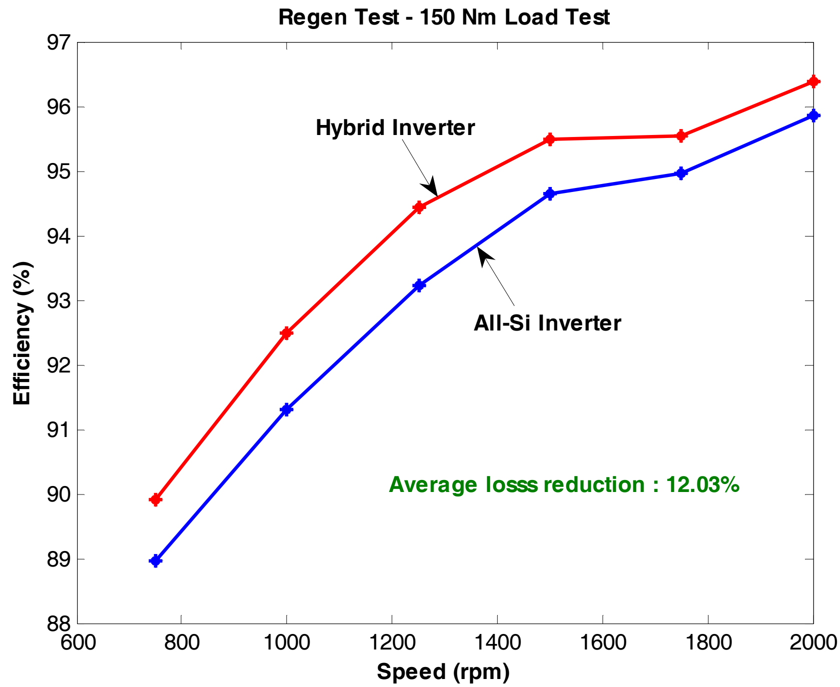

(b) 150 Nm load torque.

Fig. 3.26. Dynamometer test–regeneration mode efficiency plots at 70ºC.

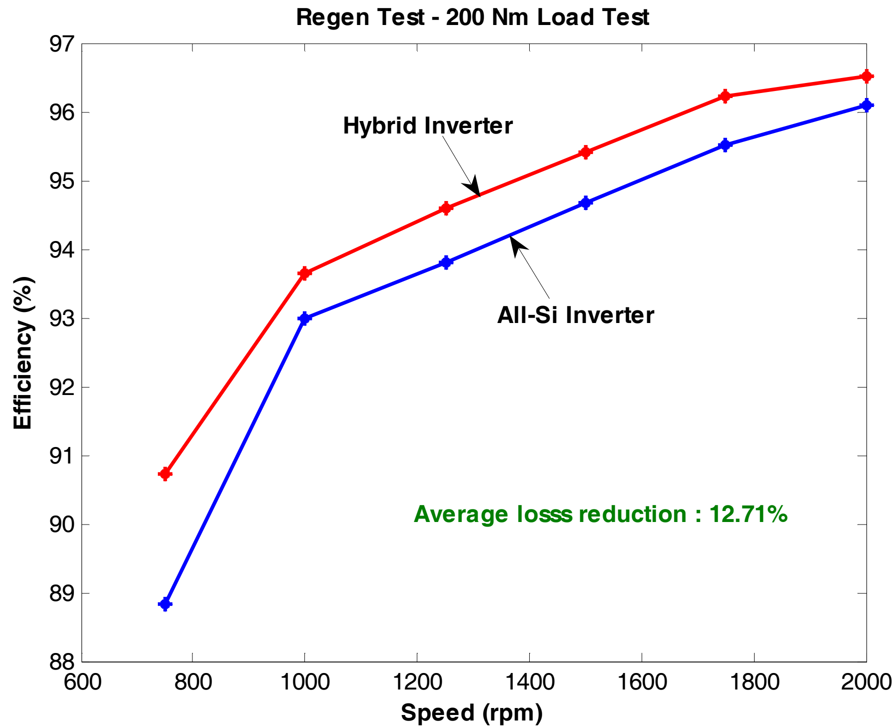

(c) 200 Nm load torque.

Fig. 3.26. Dynamometer test–regeneration mode efficiency plots at 70ºC (cont'd).

3.8 EXPLANATION FOR THE POWER LOSS DIFFERENCE BETWEEN THE INVERTERS

The results for the all-Si and the hybrid inverters for the various tests conducted have proved that the Si IGBT–SiC Schottky diode hybrid inverter has better performance than the all-Si inverter. The effect of replacing the Si pn diodes with the SiC Schottky diodes resulted in improved inverter efficiency.

The difference in efficiencies for the various operating conditions of the two inverters can be explained by the static and dynamic characteristics of the diodes. A comparison of the static characteristics of the Si pn diodes and SiC Schottky diodes obtained from one of the inverter phase legs is shown in Fig. 3.27. The built-in forward voltage drop of the SiC and Si diodes is almost the same; however, the on-state resistance of the Si pn diode at higher currents is much higher (slope of the static characteristics much lower) than that of the SiC Schottky diode. Therefore, the conduction losses of the SiC diode will be less compared with the Si pn diode at higher currents.

The SiC diode has lower reverse-recovery losses than the Si pn diode, as shown in Fig. 3.28. It should be noted that the package for the SiC diode is not a commercial package; hence the turn-off of the SiC Schottky diode has more oscillations because of the package capacitance. The superior reverse-recovery characteristics of the SiC diode also results in reduced losses in the IGBT. This is because when a diode in an inverter is turning off, the diode-reverse-recovery current passes through the other IGBT in the same phase leg causing additional losses. The effect of this difference in diode-switching losses becomes significant as the frequency increases; therefore, for the same operating conditions (same load current, operating voltage, operating frequency, and coolant temperature) the losses in the hybrid inverter will be less than in the all-Si inverter.

Some other observations and explanations for loss difference between the inverters in different modes are as follows

1. The average loss reduction is much higher in the regeneration mode than the motoring mode because the diodes conduct more in the regeneration mode, which is evident from Fig. 3.29.

2. At higher load torques in the motoring mode, the displacement factor is higher and hence the average loss reduction is less. The reason is that at higher power factors in motoring mode, the main switches conduct more than the diodes.

3. During the regeneration mode at higher torques, the average losses increase as the displacement factor increases and the diodes conduct more.

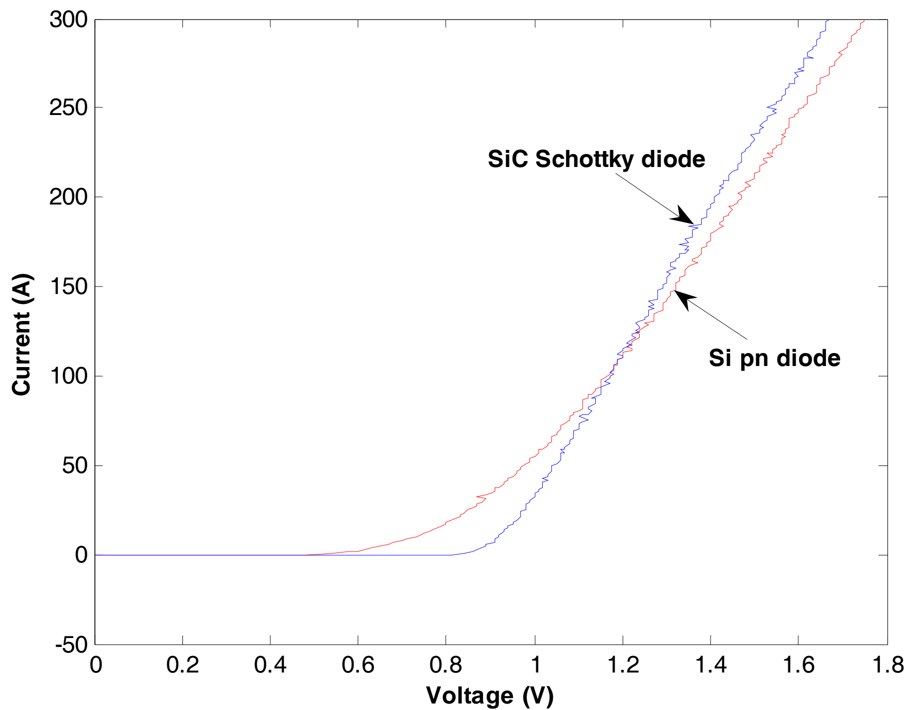

Fig. 3.27. Comparison of static characteristics of Si pn diode and SiC Schottky diodes.

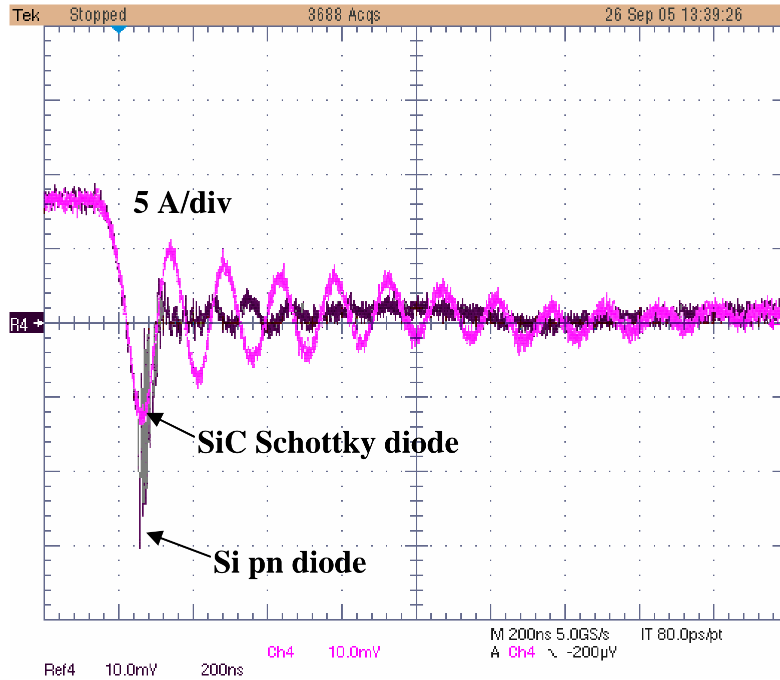

Fig. 3.28. Comparison of reverse-recovery characteristics of Si pn diode and SiC Schottky diode.

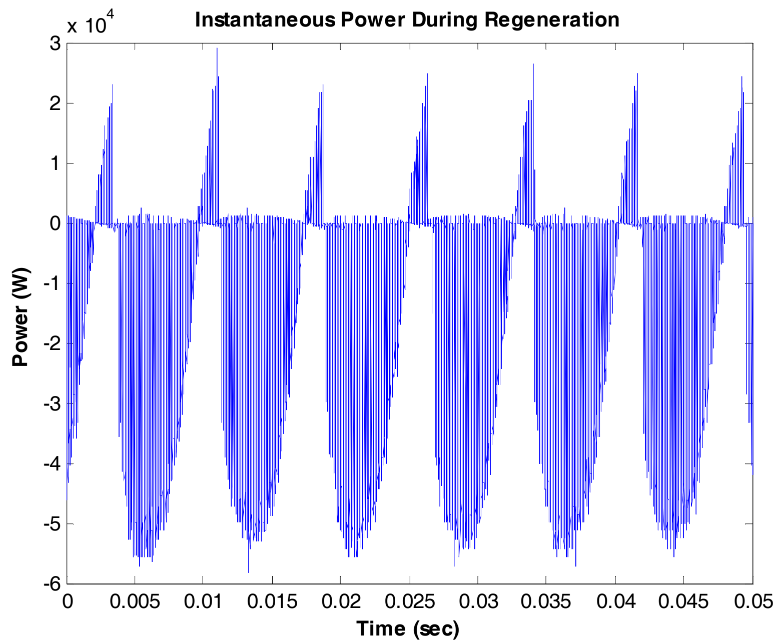

Fig. 3.29. Instantaneous output power during regeneration.

3.9 CONCLUSIONS

The 75-A SiC Schottky diodes used in the Si IGBT–SiC Schottky diode hybrid inverter were characterized and the parameter extraction was conducted to build a model using Saber. The model was used in an inverter model with Si IGBTs, and the performance of the inverter was studied with Si and SiC

diodes. The efficiencies of the hybrid inverter were 1.5–2% higher than in the all-Si inverter, similar to the test data.

The testing of both the hybrid and the all-Si inverters was completed successfully. The inverters were able to operate at peak power levels with efficiencies of greater than 90%. The inverters were tested for a maximum continuous power of 47 kW. The hybrid inverter had an average loss reduction of up to 33.6% compared with the all-Si inverter for the R-L load test. The motoring and regeneration tests were done at lower power levels and showed a reduction of around 10% in the average power losses. These test results show a trend similar to the results obtained in the simulation.

4. ALL-SiC INVERTER

4.1 INTRODUCTION

SiC power switches have been demonstrated to have better performance compared with the equivalent Si power switches. Simulation studies have proved that SiC devices, when compared with their Si counterparts, have a better effect on the total system performance. SiC diodes are the only commercialized devices available in the market. The SiC power switches are only available as some experimental samples.

A 7.5-kW all-SiC inverter was built in collaboration with Rockwell Scientific to study the effect of replacing the Si devices with SiC devices in the inverters. The module was built using JFETs as the main power switches and SiC Schottky diodes. The performance of the all-SiC inverter was compared with a similarly rated all-Si inverter.

4.2 JFET CHARACTERIZATION AND MODELING

4.2.1 SiC JFET Characterization

JFETs have reached a high level of maturity in SiC technology beyond that of other transistors, but they still require further improvements for commercialization. Power JFETs are built with vertical topologies, as shown in Fig. 4.1, and can support higher breakdown voltages as a result of their thick drift layer.

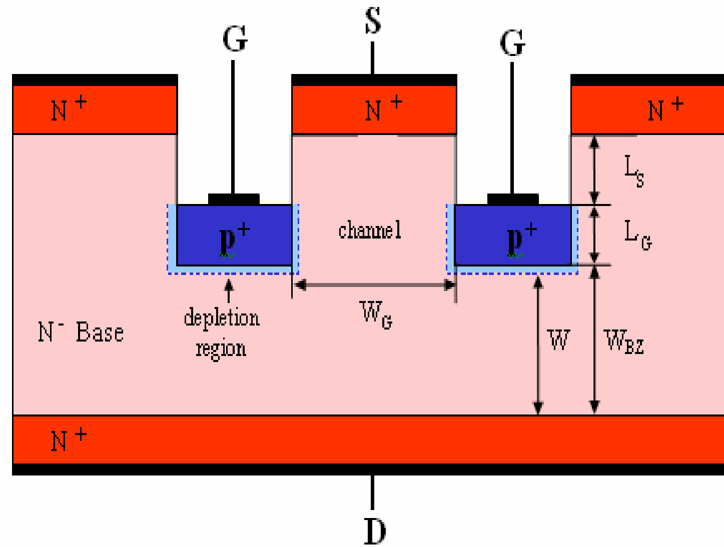

Fig. 4.1. Cross-section of the SiC VJFET structure.

One of the SiC JFETs from Rockwell (rated at 1200 V, 15 A) was tested for on-state and switching characteristics to obtain data for modeling. The JFET was placed in the Tek371B curve tracer and the on-state characteristics were measured in the unipolar and the bipolar mode.

The SiC JFETs from Rockwell are normally-on devices, meaning a negative-gate voltage is required to turn them off. The gate voltage, V_{gs}, at which the JFET actually stops conducting (drain current $I_{ds} = 0$ for any value of V_{ds}) is known as the pinch-off voltage. In the unipolar configuration, the gate is negatively biased with respect to the source. Figure 4.2 shows the measured data of the JFETs in the unipolar region

of operation. In the unipolar mode, the JFET acts as a majority-carrier device and hence only the electrons are carriers. On the other hand, in the bipolar mode of operation, the gate is positively biased with respect to the source. In this case, both electrons and holes conduct and the total current is higher than in the unipolar mode as a result of the increased conduction. The JFET was also tested in the bipolar mode; the results are shown in Fig. 4.3.

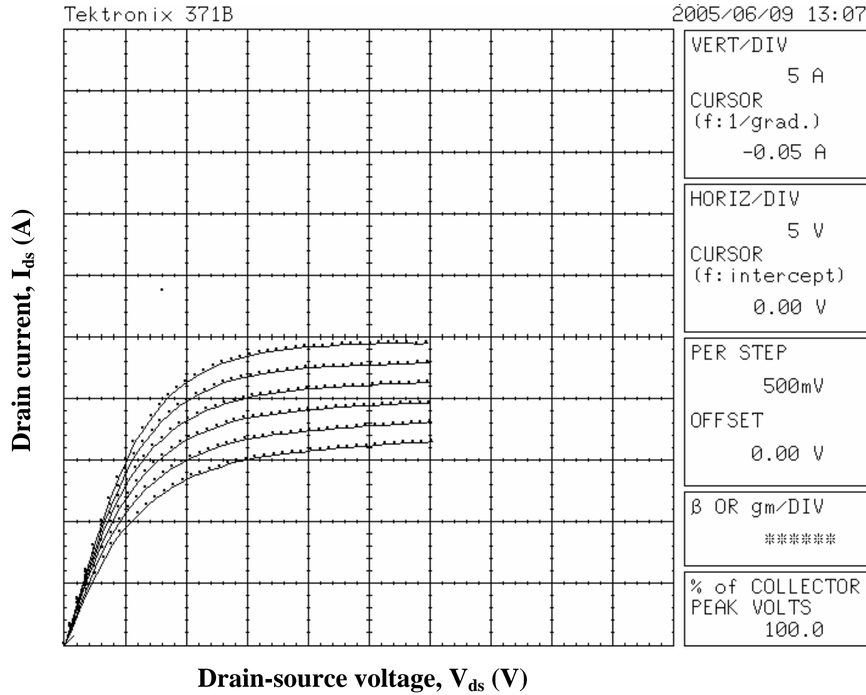

Fig. 4.2. Unipolar operation of the Rockwell SiC JFET.

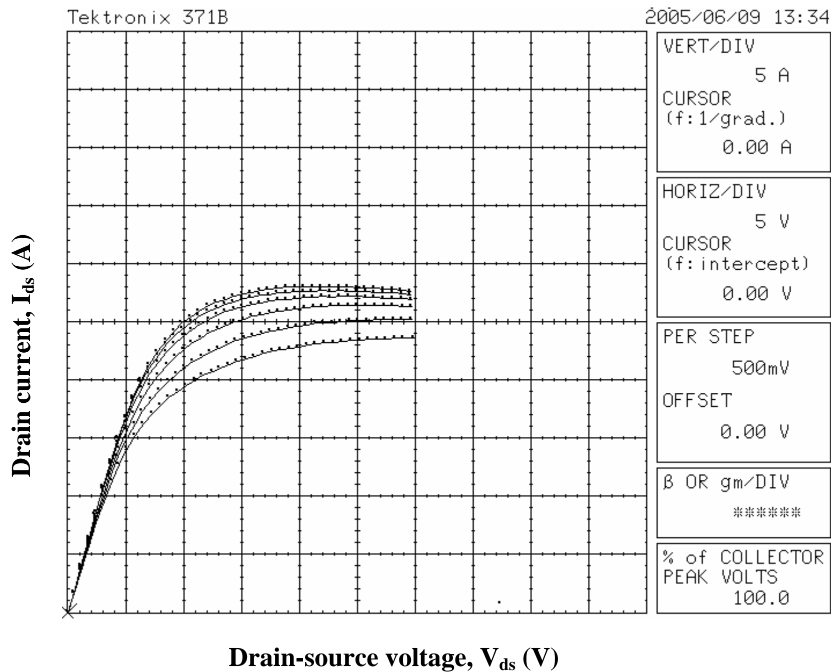

Fig. 4.3. Bipolar operation of the Rockwell SiC JFET.

An interesting observation from Figs. 4.2 and 4.3 is that even though the JFETs are rated only for 15 A, they were able to operate at nearly twice the rated current. This is because the curve tracer uses a pulsed-voltage supply that greatly decreases the self-heating of the device.

The pinch-off voltage is an important parameter in the model, and it must be evaluated by performing a separate test. To find the pinch-off voltage, a constant drain-to-source voltage (V_{ds}) is imposed on the device and the gate-to-source voltage is swept. This is also known as the transfer characteristic. The V_{gs} at which the JFET just stops conducting is known as the pinch-off voltage, which was found to be approximately –25 V for this particular JFET. Figure 4.4 shows the results of the pinch-off voltage test.

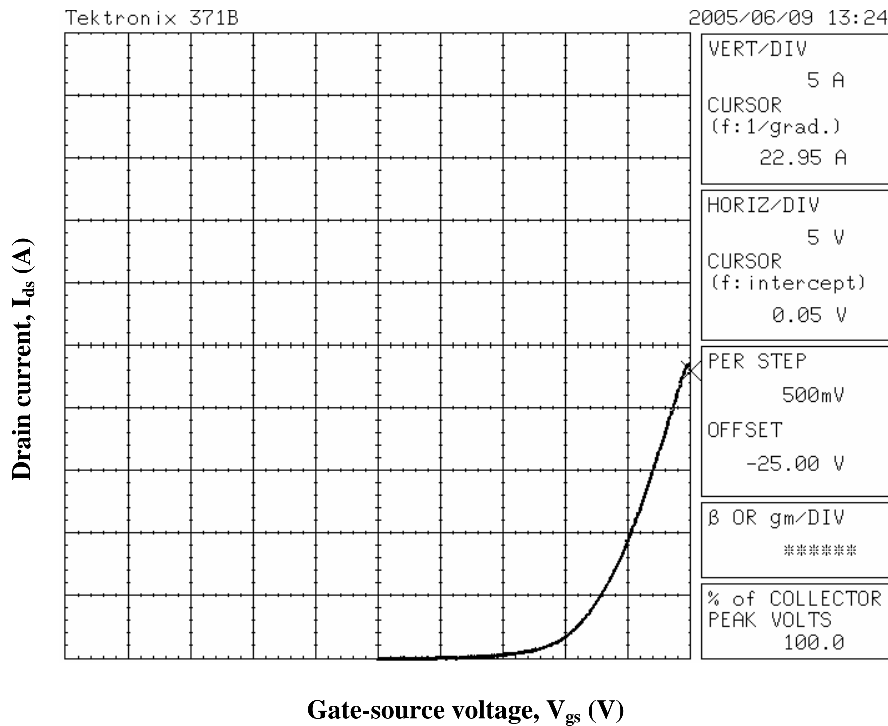

Fig. 4.4. Test for obtaining the pinch-off voltage.

After the dc characteristics were tested, the transient characteristics were tested. A high-speed gate-driver circuit developed at ORNL was used to drive the JFETs. The turn-on and the turn-off characteristics were tested to accurately model the switching characteristics. The circuit consists of a constant dc supply (40 V) connected to the drain. The load consists of a 40-Ω resistor and a parasitic inductance of 13 μH. The gate had a series resistance of 25 Ω and parasitic inductance of 0.5 μH. To ensure that the JFET was completely turned off, the gate voltage was switched between –25 and 0 V. The turn-on and turn-off waveforms are shown in Figs. 4.5 and 4.6.

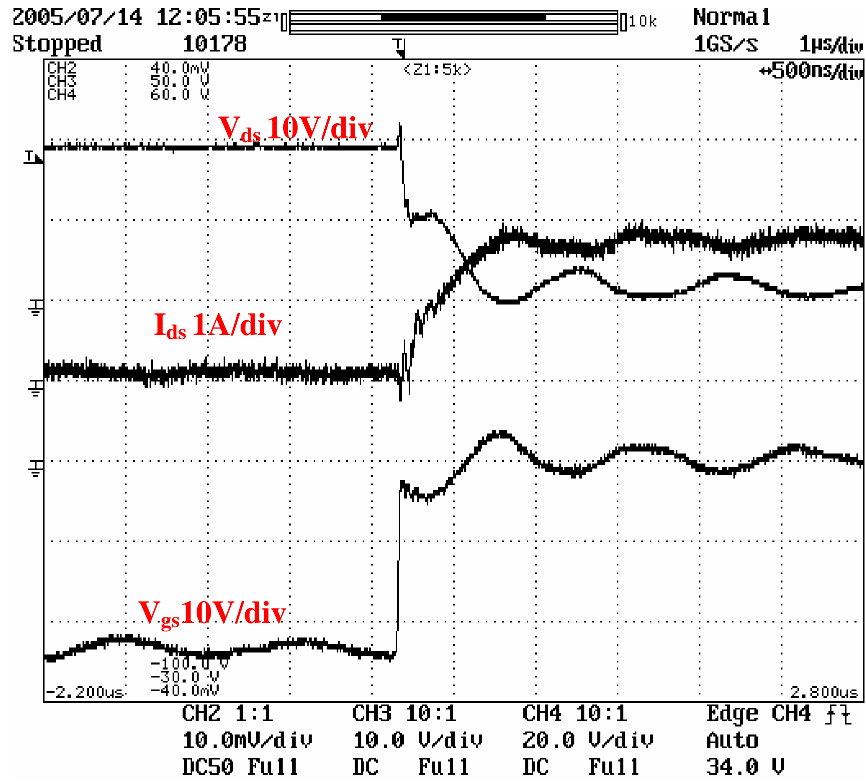

Fig. 4.5. Turn-on waveforms of the SiC JFET.

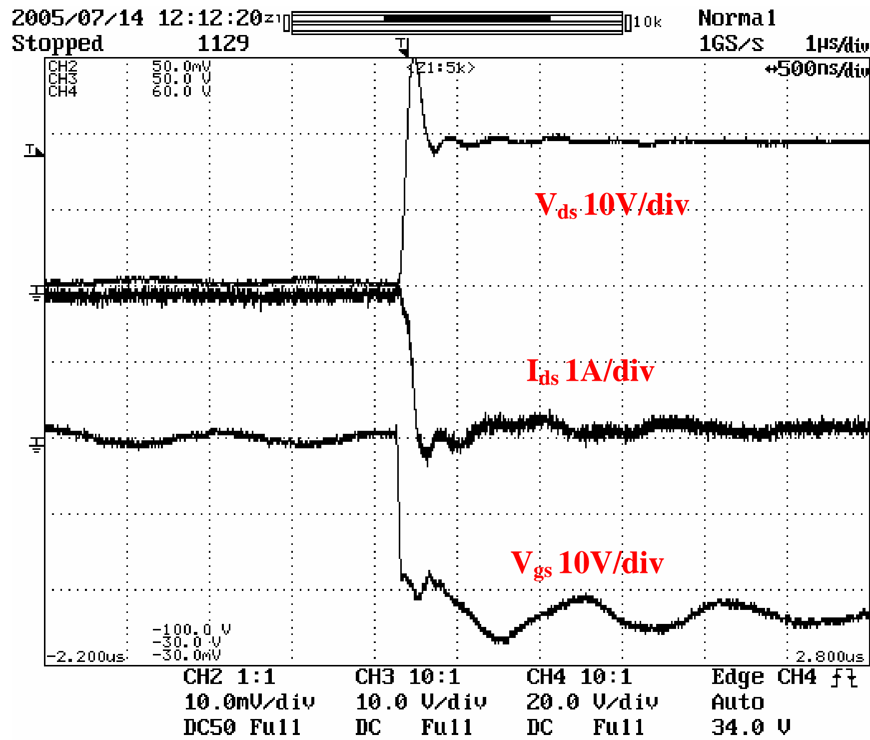

Fig. 4.6. Turn-off waveforms of the SiC JFET.

4.2.2 SiC JFET Modeling

The device physics-based analytical SiC JFET model (Fig. 4.7) used for this project was developed by the University of Arkansas. It is a flexible model that can predict the unipolar and bipolar operation of SiC JFETs. This circuit representation allows the modeler to visualize and qualitatively assign equations for all the branches and elements. It should be noted that the topology does not represent a sub-circuit of any kind.

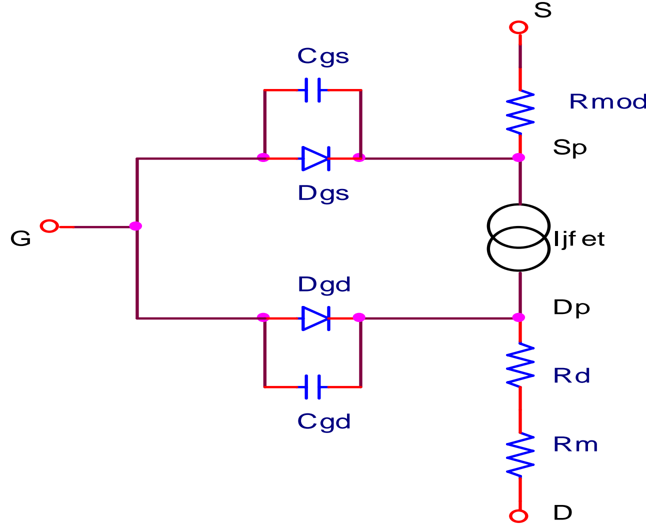

Fig. 4.7. Internal topology of the SiC JFET [20].

The model can be visualized as consisting of a source-region resistance, R_{mod}, that is conductivity modulated by i_{mod} for positive-gate voltages; an ideal JFET that describes the channel current, I_{JFET}; a bias-dependent series base or drift-region resistance, R_d; and a series-contact resistance, R_m. D_{gs} and D_{gd} are representations of the gate-source and gate-drain pn junctions. C_{gs} and C_{gd} are the corresponding junction capacitances. D_p and S_p, seen in the topology as shown in Fig. 4.7, are the internal nodes in the model.

The major equations used to model the on-state characteristics are as follows

$$I_g + I_d = I_s \,. \tag{4.1}$$

(i) Pre-turn-on: if $V_{gs} + V_p - V_{bi} <= 0$,

$$Ids = 0. \tag{4.2}$$

(ii) Linear: if $V_{ds} < (V_{gs} + V_p - V_{bi})$,

$$I_{ds} = G_o \left\{ V_{ds} - \frac{2}{3}\sqrt{\frac{1}{V_p}}\left[\sqrt{\left(V_{bi} - V_{gs} + V_{ds}\right)^3} - \sqrt{\left(V_{bi} - V_{gs}\right)^3}\right]\right\}. \tag{4.3}$$

(iii) Saturation: if $V_{ds} \geq (V_{gs} + V_p - V_{bi})$,

$$I_{ds} = \frac{G_o V_p}{3}\left[1 - 3\frac{V_{bi} - V_{gs}}{V_p} + 2\sqrt{\left(\frac{V_{bi} - V_{gs}}{V_p}\right)^3}\right]. \quad (4.4)$$

In many cases, parameters involving device geometry and dimensions may not be available to the modeler. Those parameters are lumped together to form an extractable parameter called G_o, which is defined as the conductance of the device with which the modeler or the circuit designer can adjust the saturation current of the device. The metallurgical base width of the Static induction transistor (SIT) is given by the equation:

$$W = W_{bz} - W_{gd}, \quad (4.5)$$

where W_{bz} is the zero-bias value of the depletion width and W_{gd} is the gate-drain junction depletion width. As only the unipolar operating mode is considered, the only carriers are electrons, and their mobility is given by the relation

$$\mu_n = \frac{947}{\left(1 + \left(\frac{N_b}{1.94x10^{17}}\right)\right)^{0.61}}\left(\frac{T}{300}\right)^{-2.15}. \quad (4.6)$$

For the bipolar mode, the mobility of the holes should also be considered. It is given as

$$\mu_p = 15.9 + \frac{108.1}{\left(1 + \left(\frac{N_b}{1.76x10^{19}}\right)\right)^{0.34}}\left(\frac{T}{300}\right)^{-2.15}. \quad (4.7)$$

The bias-dependent drift-region resistance is given as

$$R_d = \frac{W}{qN_b\mu_n\left(A_g + A_s\right)}. \quad (4.8)$$

The conduction charge due to background doping is

$$q_m = \tau \cdot I_{gs}, \quad (4.9)$$

where τ is the minority-carrier lifetime and I_{gs} is the gate-source current.

The modulation current in the bipolar mode is

$$i_{mod} = \frac{(\mu_n + \mu_p) V_{gs} q_m}{W_{gd}^2} \quad . \tag{4.10}$$

The current flow in the gate-drain pn junction:

$$I_{gd} = I_{sgd}(exp(V_{gd}/ngd \cdot V_t)-1) \ . \tag{4.11}$$

The current flow in the gate-source pn junction:

$$I_{gs} = I_{sgs}(exp(V_{gs}/ngs \cdot V_t) - 1) \ . \tag{4.12}$$

While the above equations describe the operation of the model under dc conditions, a separate set of equations must be developed for predicting the transient response. The turn-on and turn-off mechanisms are mainly dominated by the junction capacitances between the gate-source and gate-drain areas. They are mathematically described as follows in Eq. (4.13). The gate-source depletion width is given by the relation

$$W_{gs} = \sqrt{\frac{2\varepsilon_{SiC}(V_{gs} + V_{bi})}{qN_D}} \quad . \tag{4.13}$$

The associated capacitance is

$$C_{gs} = \frac{f_{csj} A_s \varepsilon_{SiC}}{W_{gs}} \quad . \tag{4.14}$$

Similarly, the gate-drain depletion area is given by the relation

$$W_{gd} = \sqrt{\frac{2\varepsilon_{SiC}(V_{gd} + V_{bi})}{qN_D}} \quad . \tag{4.15}$$

And the capacitance of the depletion region is

$$C_{gd} = \frac{A_g \varepsilon_{SiC}}{W_{gd}} \quad . \tag{4.16}$$

4.2.3 Parameter Extraction and Model Validation of the Rockwell SiC JFET

The first parameter that was evaluated was the pinch-off voltage (*VP*) that determines the voltage at which the JFET is completely turned off.

The base doping *Nb* was set at the default value of 2 × 10^{15}/cm^3, which is the typical doping for the drift layer in SiC devices.

The conductance *Go* is found in an empirical way. Its value is set at the highest-current value divided by 2. In the unipolar mode, the highest-current value was found to be 24 A. Therefore, *Go* was set at 12.

The constant-series resistance *RS* is found from the inverse of the slope (taken at the medium- to high-current region) from the transfer characteristic as seen in Fig. 4.8. The ideality factor *NGS* and *NGD* for the gate-source and gate-drain pn junctions are set at the default value of 2.

The channel modulation factor *LAMBDA* can be extracted as seen in Fig. 4.9.

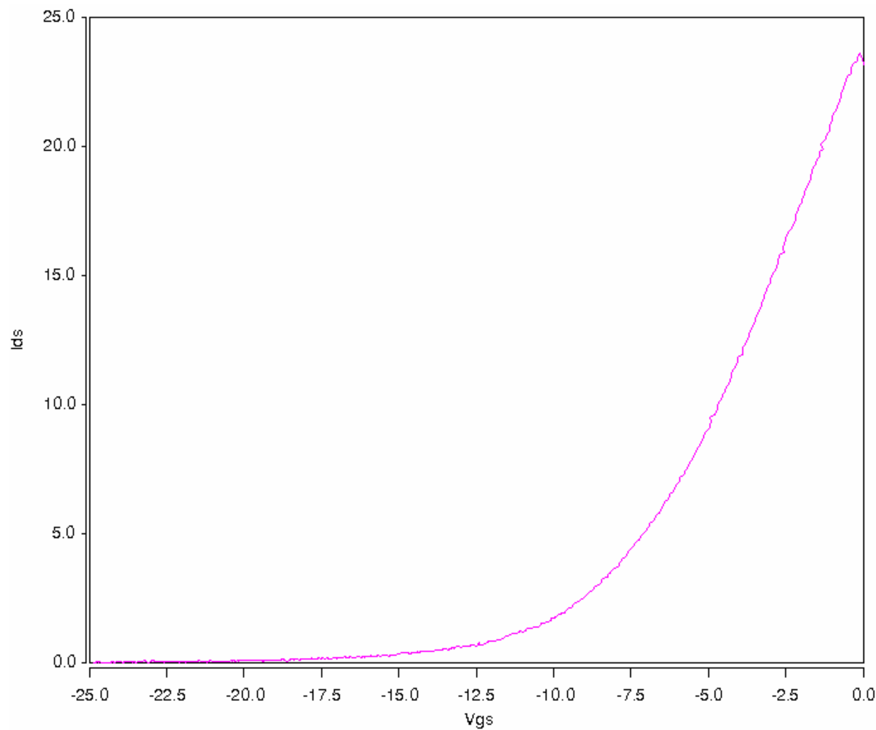

Fig. 4.8. Transfer characteristics of the Rockwell JFET.

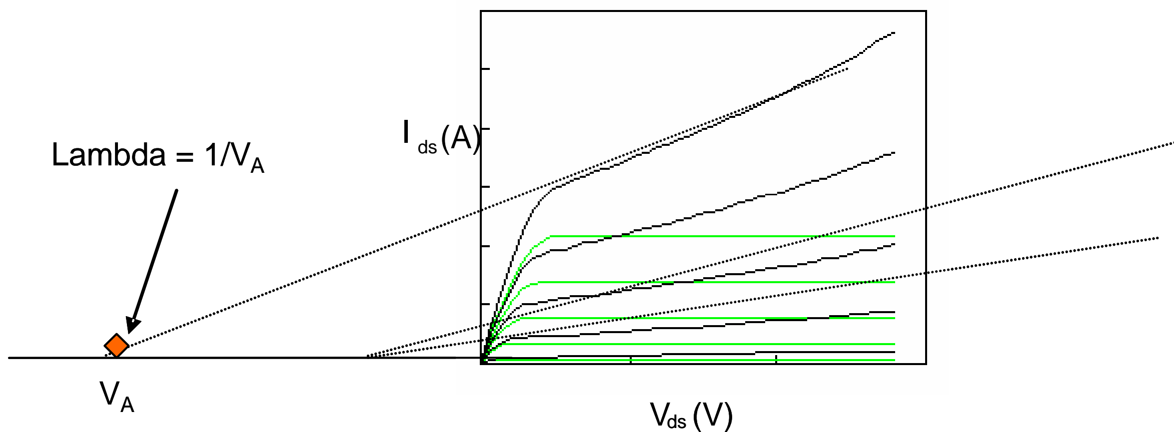

Fig. 4.9. Extraction of channel modulation factor LAMBDA.

In Fig. 4.9, the green waveforms are the ones where *LAMBDA* is set to zero (ideal condition). But in most transistors, the drain current never stays the same during saturation; there is a slight increase, as seen in the on-state curves shown in black. When extrapolated, it is seen that the linear waveforms converge at a point in the x-axis denoted as V_A (or the "early" voltage in MOSFET parlance). The inverse of V_A is taken as the value of *LAMBDA*. The constant gate-source metallization capacitance (*CGSM*) can be obtained from the switching waveforms.

The on-state validation was done only for the unipolar operation, as the JFET is mainly used in that area, as shown in Fig. 4.10. The simulated values agree with the measured value, the fitting error being approximately 2–3%.

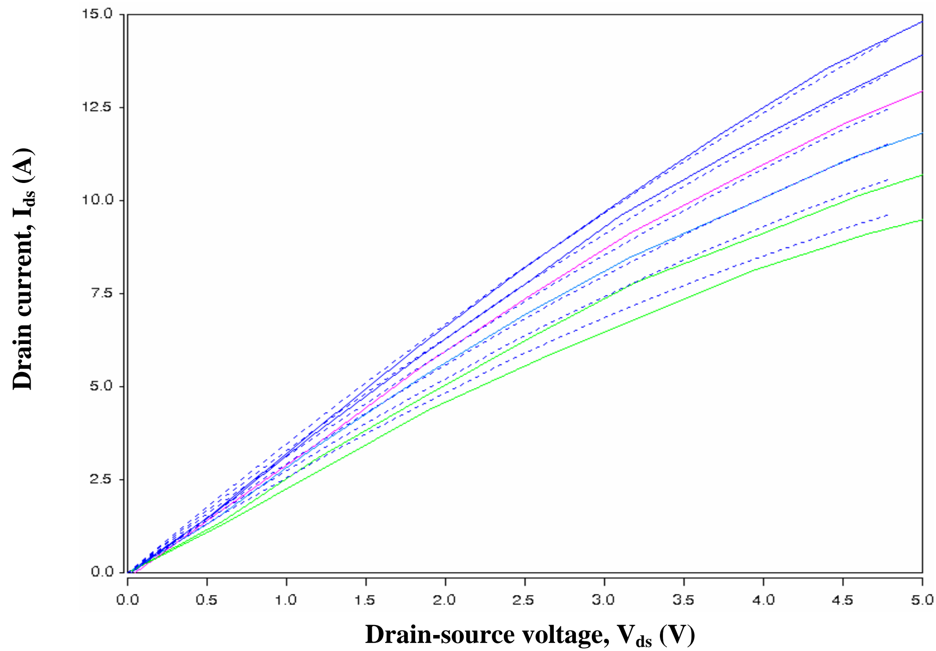

Fig. 4.10. Rockwell SiC JFET measured (solid) and simulated (dotted) on-state waveforms at 25°C for different gate voltages (V_{gs} ranging from 0V to –2.5V).

The transient response validation was done in Saber by building a behavioral model of the experimental test-bench as seen in Fig. 4.11.

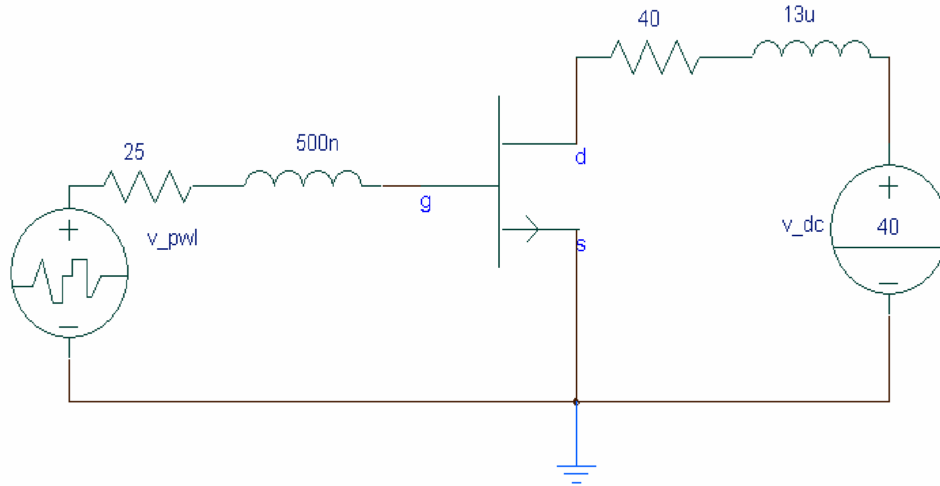

Fig. 4.11. Extraction of channel modulation factor LAMBDA.

The switching characteristics seen in Figs. 4.12 and 4.13 can be explained by the capacitance effects among the various internal model nodes. The gate-source capacitance can be described as a constant-metallization capacitance, C_{gsm}, and a voltage-dependent capacitance, C_{gsj}, because of the gate junction relative to the source. From the gate to drain, there exists a voltage-dependent gate-N$^-$ base junction capacitance C_{gdj}. For the case of the turn-on waveforms in Fig. 4.12, the gate-voltage waveform is represented by a two-phase capacitive response. During the initial rise of the gate voltage, the constant C_{gsm} and small junction capacitance, C_{gsj}, are charged yielding the initial slope in V_{gs}

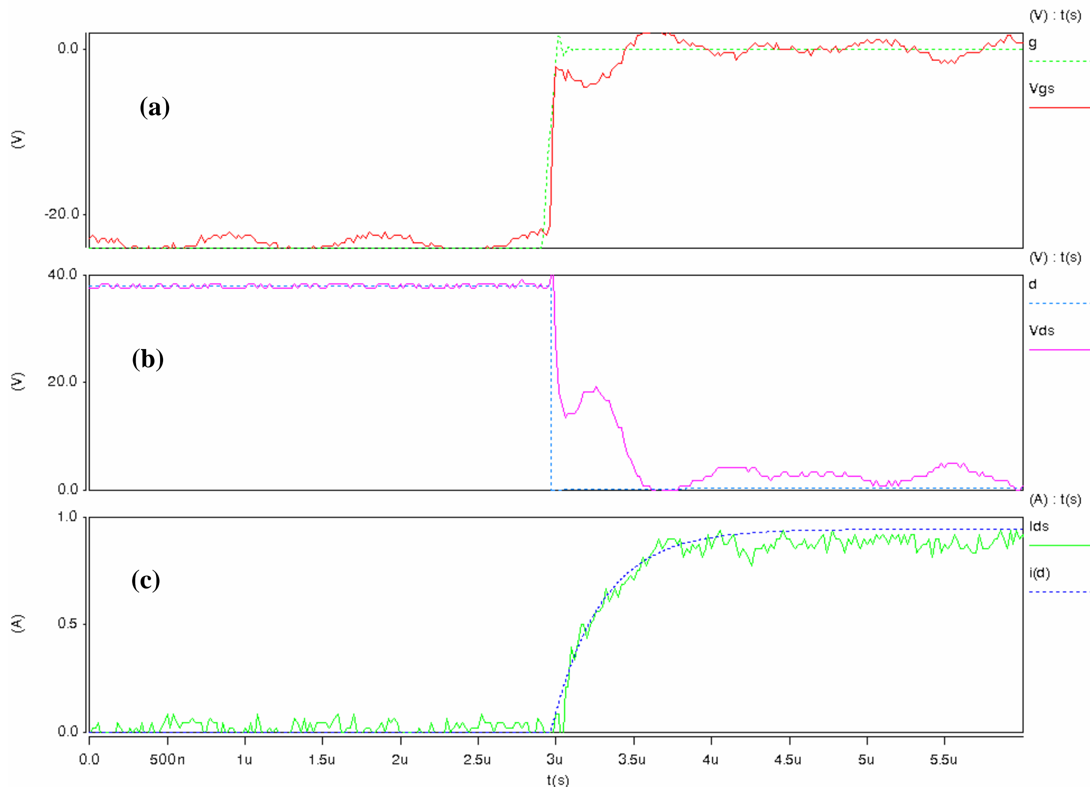

Fig. 4.12. SiC JFET simulated (dashed) and measured (solid) turn-on waveforms at 25°C: (a) gate voltage, (b) drain voltage, and (c) drain current.

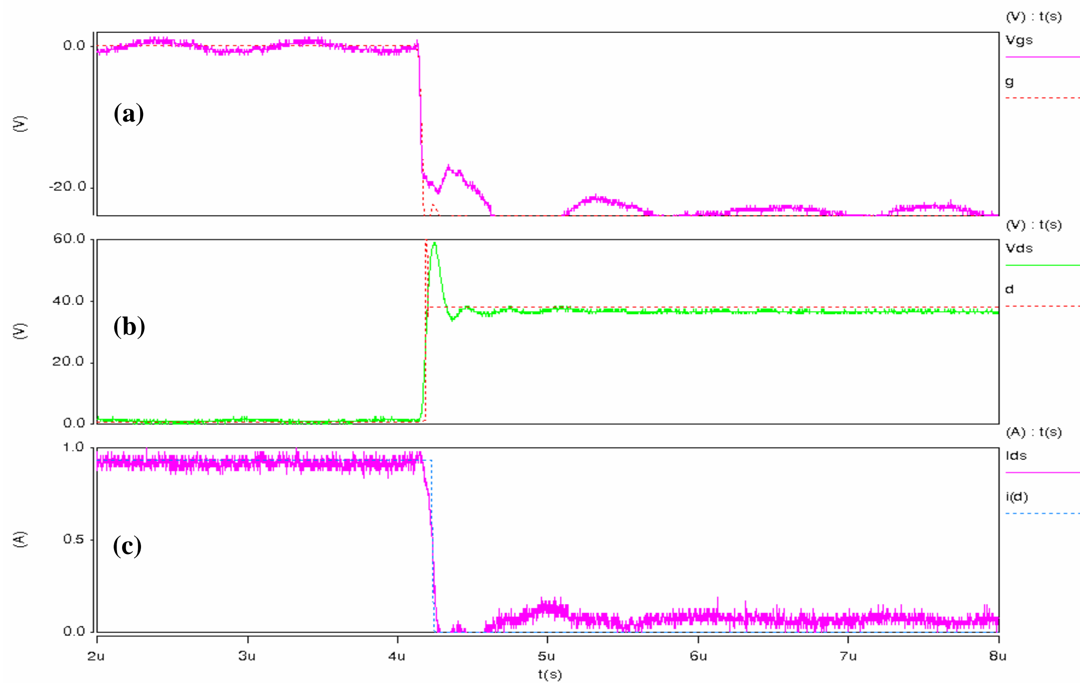

Fig. 4.13. SiC JFET simulated (dashed) and measured (solid) turn-off waveforms at 25°C: (a) gate voltage, (b) drain voltage, and (c) drain current.

Once the gate-source capacitance is charged, V_{gs} rises according to the larger gate-drain depletion capacitance C_{gdj}. The gate-drain capacitance, C_{gdj}, is charged until the threshold voltage V_t ($V_t = V_p - V_{bi}$) is reached, at which point the drain current flows as C_{gdj} continues charging. The higher the gate resistance, the more time it takes to charge the capacitances; therefore, the switching response gets slower. As observed in the transient modeling results, the switching time is on the order of 0.1 µs for a 25-Ω gate resistance. The various depletion capacitances described in the model can accurately predict the switching characteristics of the SiC JFET. The turn-off waveforms are shown in Fig. 4.13. The turn-off waveforms are seen to be much faster than the turn-on as the discharging of the junction and package capacitances happens over a shorter interval of time. Table 4.1 shows the extracted parameters of the SiC JFET.

Table. 4.1. SiC power JFET model parameters and extraction characteristics for the Rockwell 15-A JFET

Parameter	Parameter name	Extraction characteristic	Value
VP	Pinch-off voltage	Measured	–18 V
Go	Conductance of the JFET	Device-specific	12 S
NB	Doping density	Device-specific	$2e^{15}$ cm^{-3}
ISGS	Gate-source junction saturation current	High- to medium current on-state region	$1e^{-30}$ A
ISGD	Gate-drain junction saturation current	High- to medium-current on-state region	$1e^{-30}$ A
VBI	Built-in junction potential	Technology-specific	2.8 V
RS	Metallurgical resistance	Slope of high-current area in transfer curve	0.3 Ω
LAMBDA	Channel modulation parameter	Extrapolation of output characteristics	$3e^{-4}$
NGS	Gate-source junction emission coefficient	High- to medium-current on-state region	2
NGD	Gate-drain junction emission coefficient	High- to medium-current on-state region	2
CGSM	Gate-source metallization capacitance	Device-specific	100pF
FCSJ	Gate-source area factor	Device-specific	0.5
MUN	Electron mobility multiplier	Constant for 4H-SiC	947 cm^2/Vs

4.3 SIMULATION OF ALL-SiC INVERTER

The SiC JFET and diode models were used to simulate an all-SiC inverter. This is a technology demonstrator that shows a full power electronic system in SiC being successfully simulated. The validated models were used to construct the inverter system as seen in Fig. 4.14. The all-SiC inverter from Rockwell was first tested to ascertain the performance and collect test data for the inverter model validation.

A balanced three-phase 15-Ω resistive load was used to simulate the operating conditions. The switching frequency was set at 10 kHz, and the output frequency was set to 50 Hz. The inverter was simulated for different values of dc voltages and modulation indices. As explained before, the SiC JFETs used in the inverter were modeled and all the parameters were extracted. The 1200-V, 15-A SiC diode in the inverter was also modeled by the procedure explained previously. The results of the diode fitting are seen in Figs. 4.15 and 4.16. Figure 4.17 shows the output voltage of phase 1 of the inverter. The efficiency of the all-SiC inverter ranged from 83.2–87.8%.

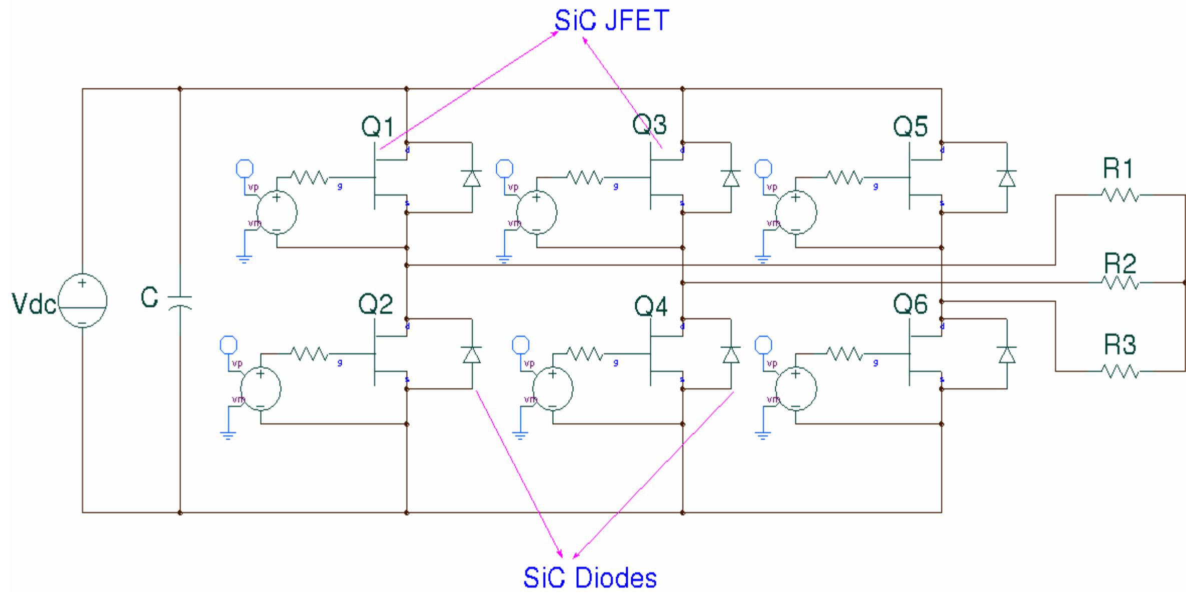

Fig. 4.14. Schematic representation of the all-SiC inverter.

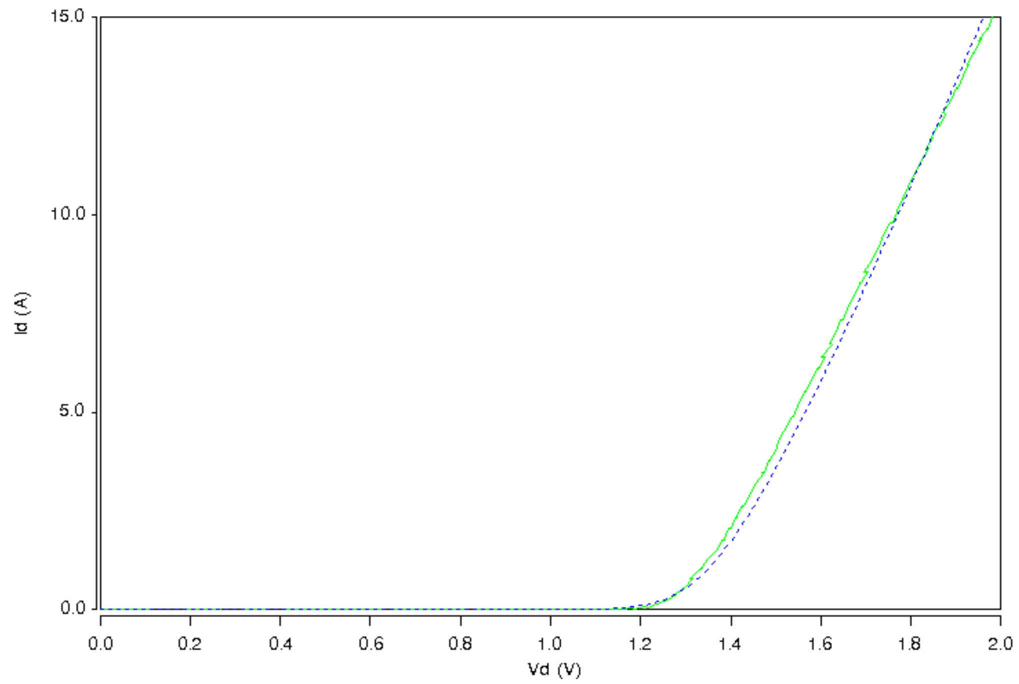

Fig. 4.15. On-state validation of SiC diode at 25°C—measured (solid) and simulated (dashed).

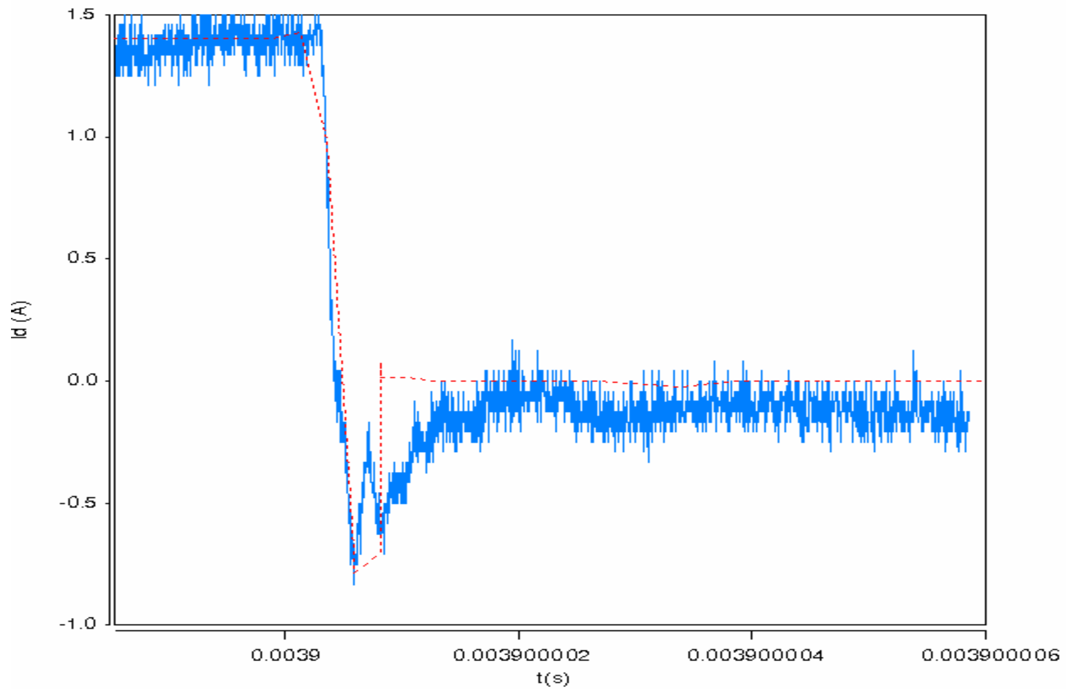

Fig. 4.16. Reverse-recovery validation of SiC diode at 25°C—measured (solid) and simulated (dashed).

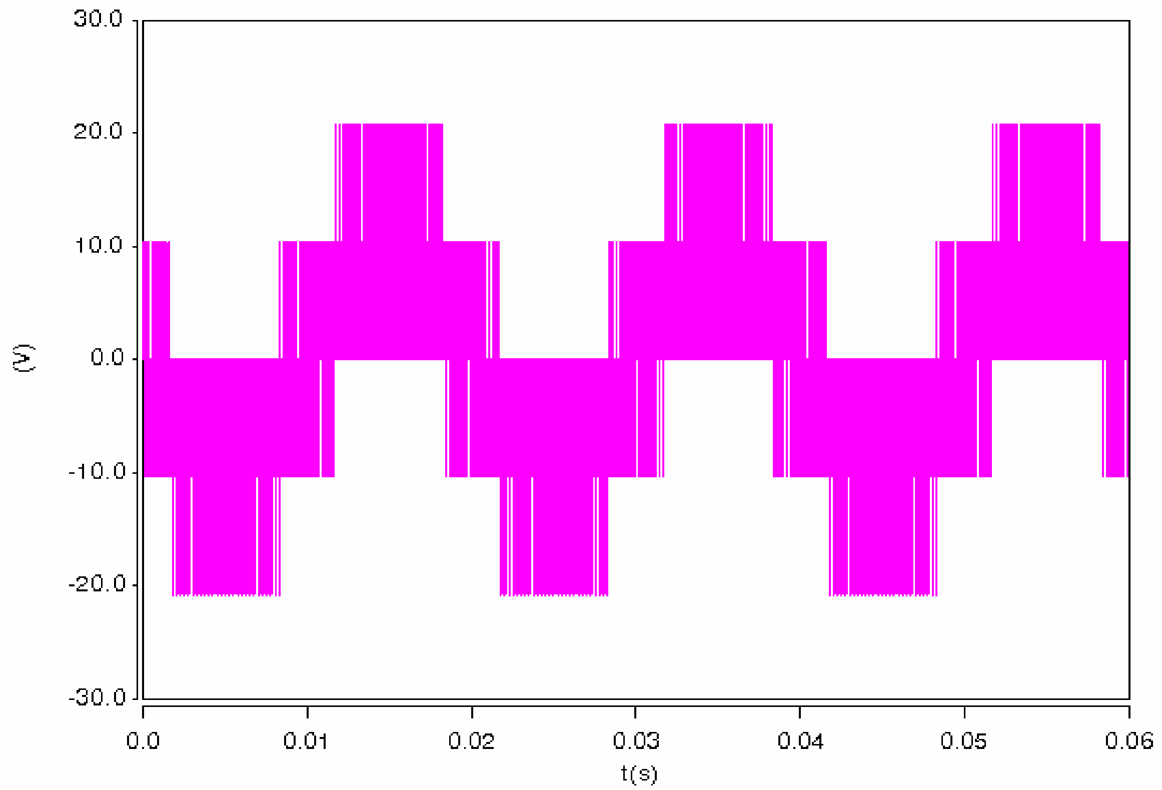

Fig. 4.17. Simulated output voltage in phase 1 of the all-SiC inverter with resistive load.

4.4 CONFIGURATION OF THE INVERTERS

The SiCinverter module was built using 1200-V, 7.5-A JFETs and 1200-V, 15-A SiC Schottky diodes. The main switches in each phase leg consisted of two JFETs with 7.5-A ratings in parallel. Three modules were developed by Rockwell Scientific and delivered to ORNL.

A Si inverter module with similar ratings was selected for a performance comparison with the all-SiC unit. Pictures of the SiC and the Si modules are shown in Figs. 4.18 and 4.19.

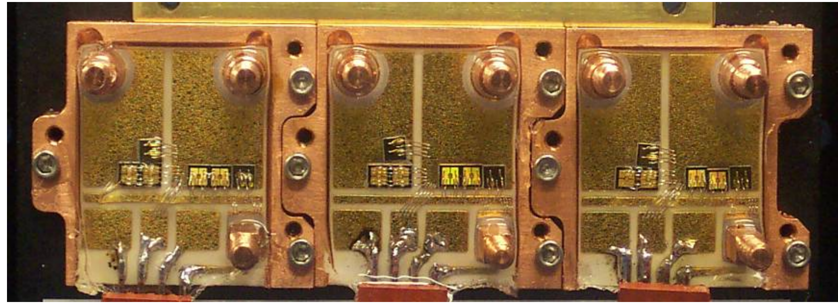

Fig. 4.18. All-SiC module.

Fig. 4.19. All-Si module.

4.5 INVERTER TESTING

4.5.1 Testing the Controller

A modified motor-drive controller shown in Fig. 4.20 was delivered by Rockwell to be used as the inverter controller. This is an open-loop controller that features two different gate-driver outputs, one for driving Si IGBTs (20-V swing) and another for driving SiC JFETs (30-V swing). Figures 4.21 and 4.22 show typical 30-V and 20-V swing output voltages supplied by the controller. The controller has a keypad to adjust the frequency of operation.

Fig. 4.20. Gate-drive control unit.

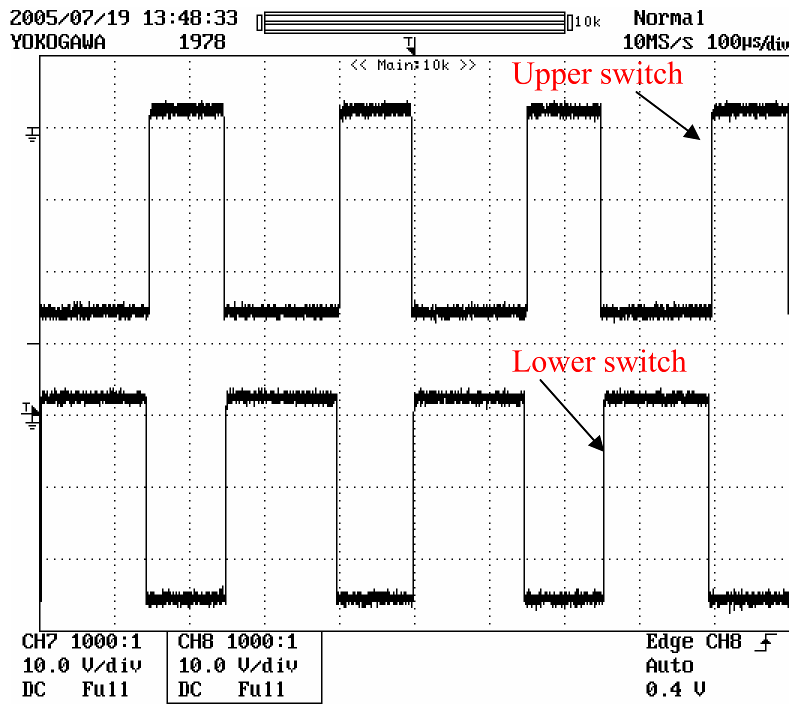

Fig. 4.21. Controller output voltage with 30-V swing for SiC module.

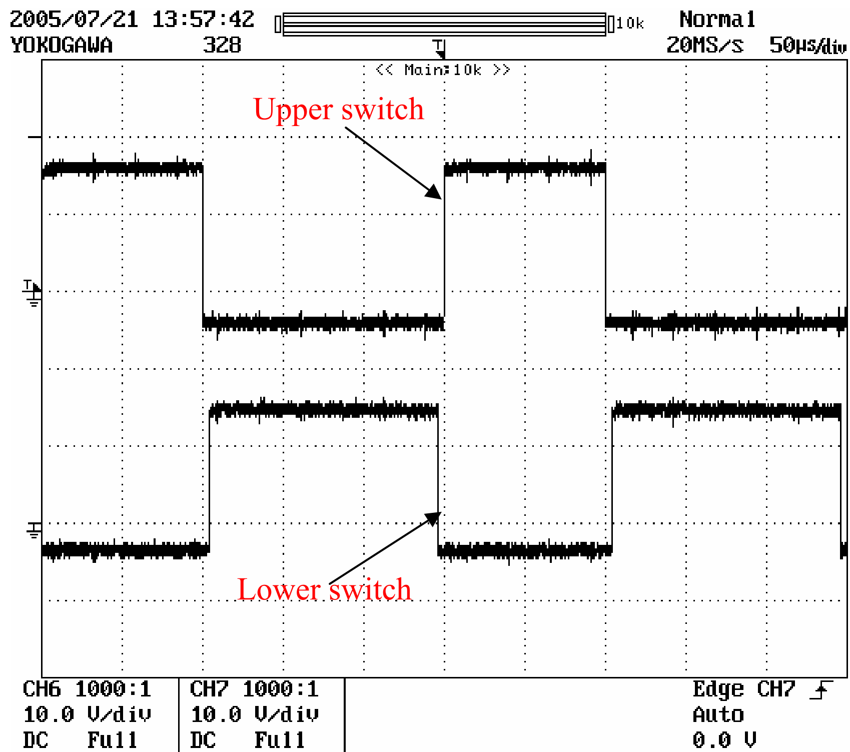

Fig. 4.22. Controller output voltage with 20-V swing for Si module.

4.5.2 Resistive- and Inductive-Load Tests

The test setup used the following equipment, as shown in Fig. 4.23.

- Yokogawa PZ4000 power analyzer for power measurement
- Variable resistor load with a capacity of 24 kW
- Inductor with 400-A capacity
- Coolant pump with a temperature controller
- A dc power supply

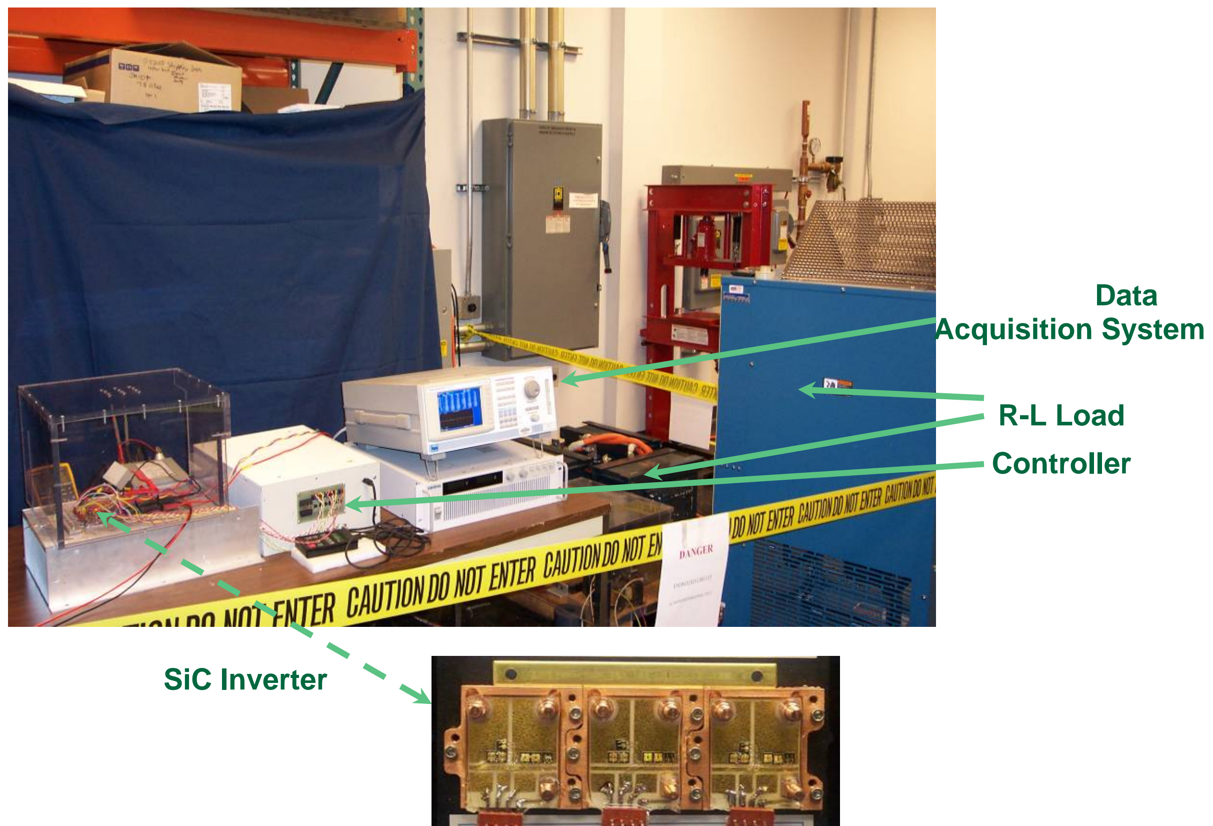

Fig. 4.23. Test setup for R-L load test.

4.5.2.1 Operation

The gate signals to the inverter modules were checked with no load on the inverter. The inverters were connected to a three-phase R-L load. The operating current was controlled by varying the load resistance. The dc-link voltage was varied from 0 to a maximum bus voltage of 400 V. The frequency of operation was fixed, and the load was varied for a particular dc-link voltage. For each setting of the load and frequency, the dc-link voltage, dc-link current, input power, output power, efficiency, output currents, and phase voltages were recorded. The load was increased in steps without exceeding the power rating of the inverter or exceeding the power rating of the load. The procedure was repeated, increasing the output frequency command in steps of 10 Hz from 10–100 Hz.

4.5.2.2 Results

The operating waveforms for the SiC inverter at different load settings are shown in Fig. 4.24. The plots of efficiency curves for different operating conditions are shown in Figs. 4.25 and 4.26. It can be seen from the plots that the efficiency of the Si inverter module is much higher than the SiC module.

To investigate the reasons for this difference, the inverters were tested with a resistive load only. With a resistive load, only the JFETs and IGBTs conduct, not the diodes. The efficiency plots for different resistive-load settings of the inverters are shown in Figs. 4.27, 4.28, and 4.29. Again, the efficiency of the all-SiC inverter was lower.

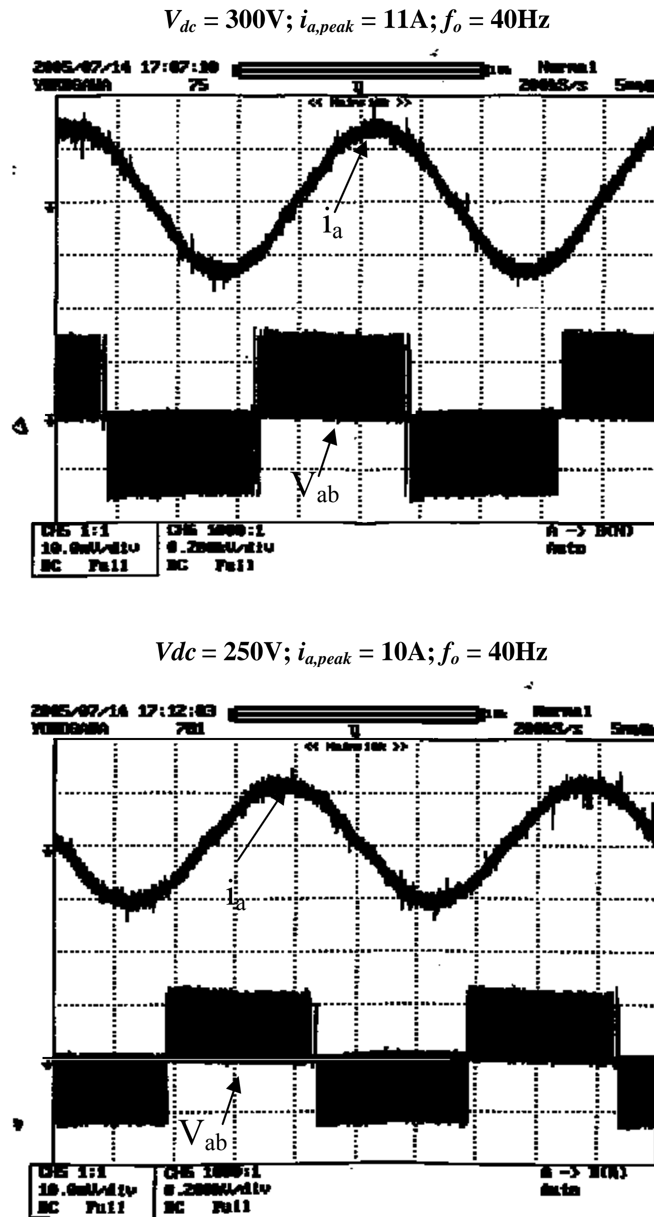

Fig. 4.24. Operating waveforms of SiC module for R-L load test.

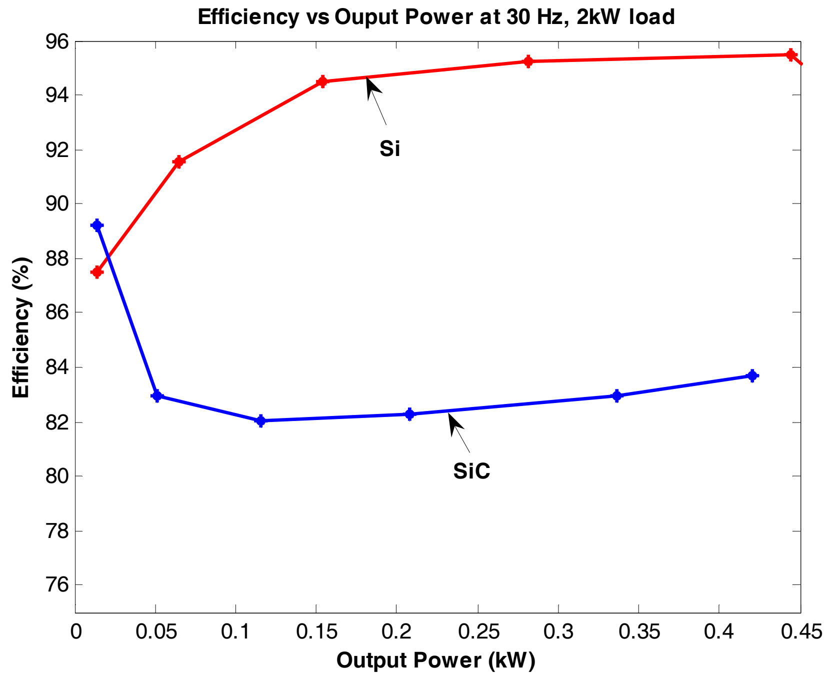

Fig. 4.25. Efficiencies comparison plot at 30-Hz operation for R-L load test.

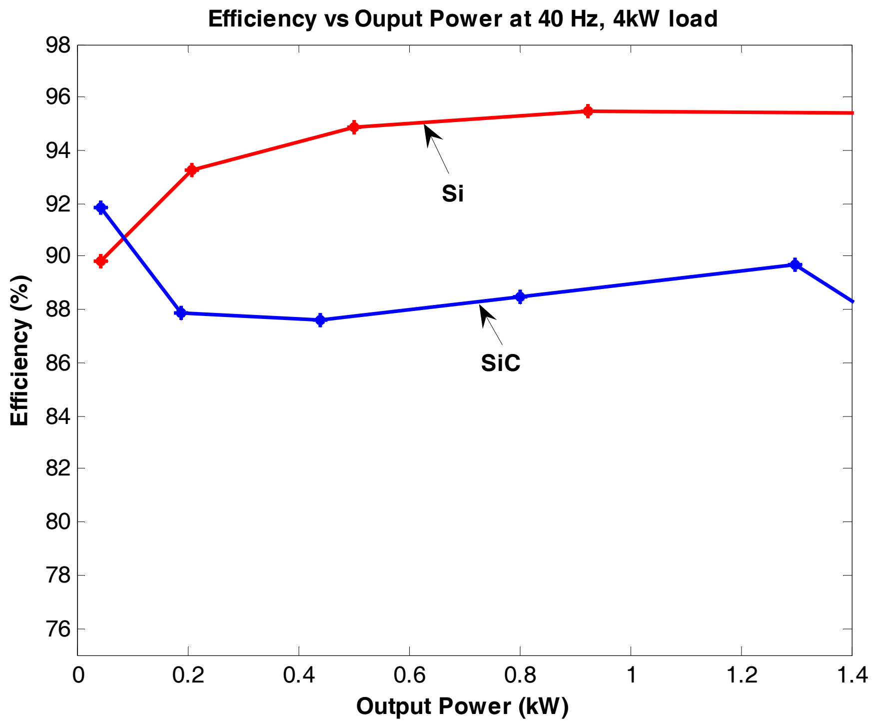

Fig. 4.26. Efficiencies comparison plot at 40-Hz operation for R-L load test.

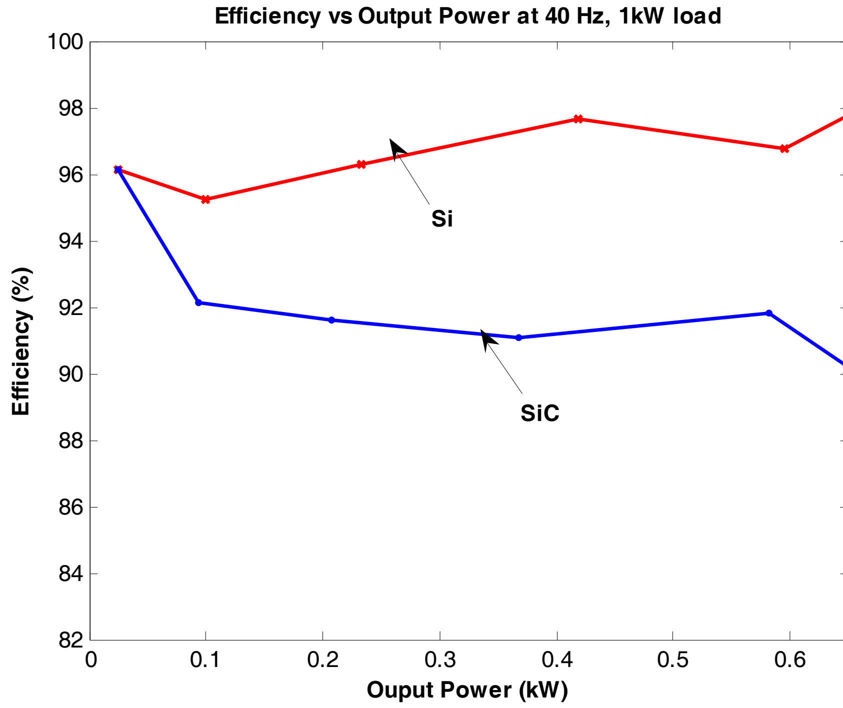

Fig. 4.27. Efficiencies comparison plot at 40-Hz operation for resistive-load test.

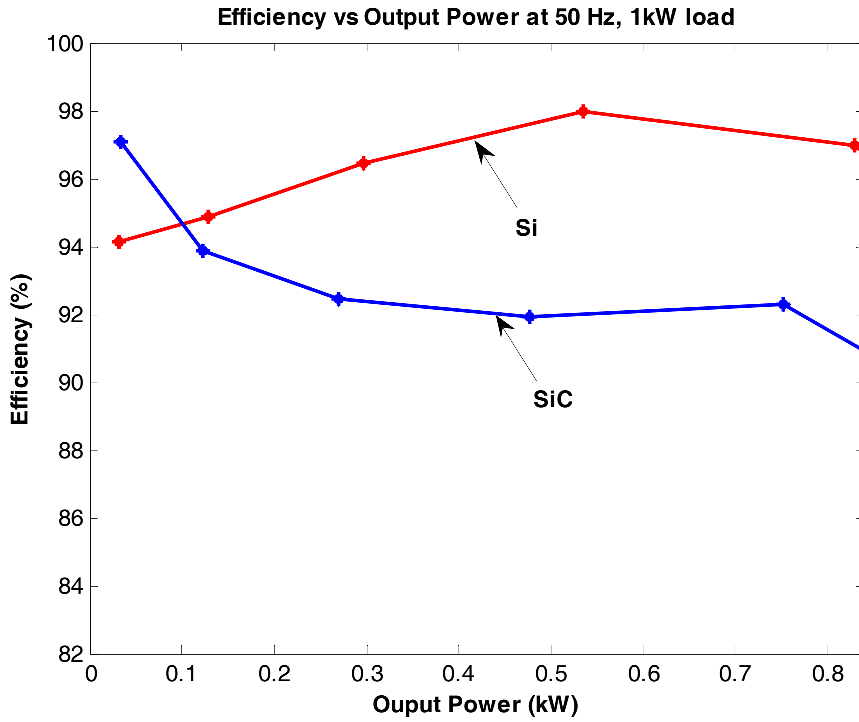

Fig. 4.28. Efficiencies comparison plot at 50-Hz operation for resistive-load test.

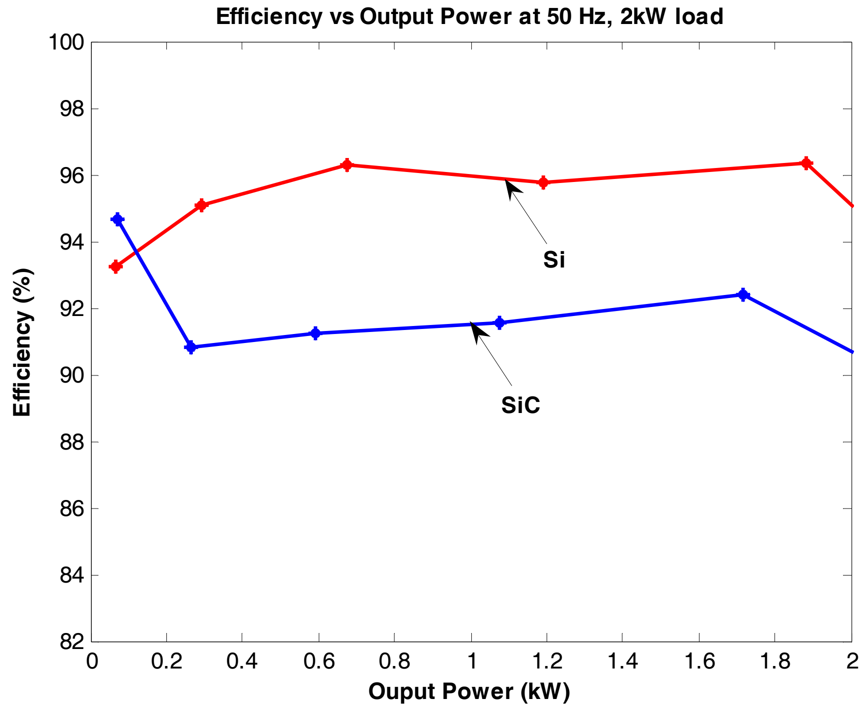

Fig. 4.29. Efficiencies comparison plot at 50-Hz operation for resistive-load test.

To get a better understanding of the reason why the all-SiC inverter efficiency was worse than that of the all-Si inverter, a comparison of the static characteristics of the IGBT, the SiC JFET, and the diodes in the inverter modules are shown in Fig. 4.30 and 4.31.

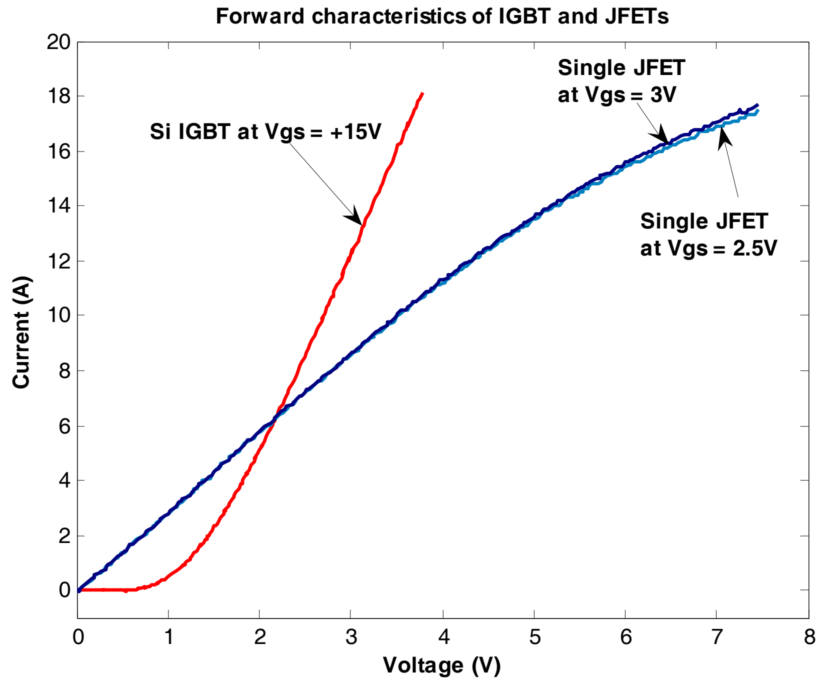

Fig. 4.30. Forward characteristics of IGBT and JFET in the Si and SiC modules.

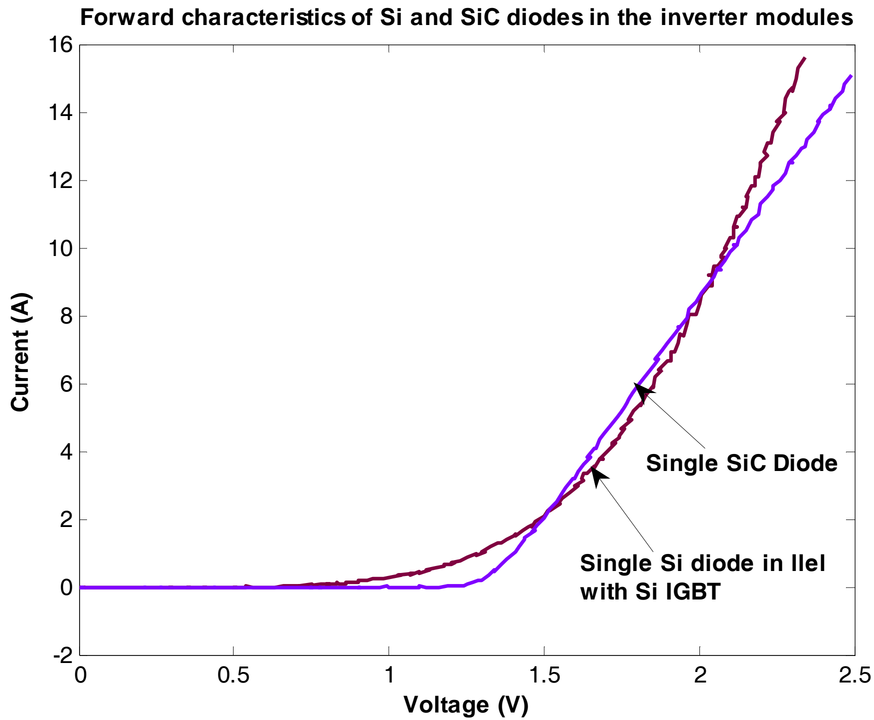

Fig. 4.31. Forward characteristics of diodes in the Si and SiC modules.

The on-state voltage drop of the Si IGBT is much less than that of the SiC JFET at higher-current levels because of the higher on-resistance of the SiC JFET. The high value of this resistance is attributed to the fact that it is a prototype device and there are still some material and processing issues to be resolved. Note that at lower currents, the SiC JFET has a lower on-state voltage drop. Considering that these particular Si pn and SiC Schottky diodes have similar static characteristics, an all-SiC inverter is expected to have higher conduction losses.

The turn-on and turn-off waveforms for the SiC JFET and Si IGBT for 4-kHz operation are shown in Figs. 4.32 and 4.33. These waveforms show that the SiC JFETs in the all-SiC inverter are much slower than the Si IGBTs tested; therefore, they have much higher switching losses.

The analysis of the conduction and switching losses of the devices shows that the devices in the all-SiC inverter are not as efficient as the devices in the off-the-shelf all-Si inverter module.

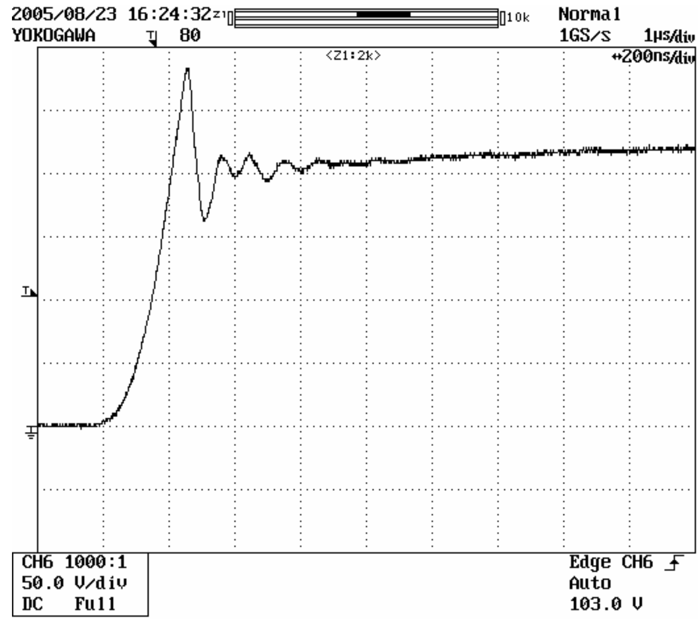

Fig. 4.32(a). Turn-off voltage waveform of SiC JFET.

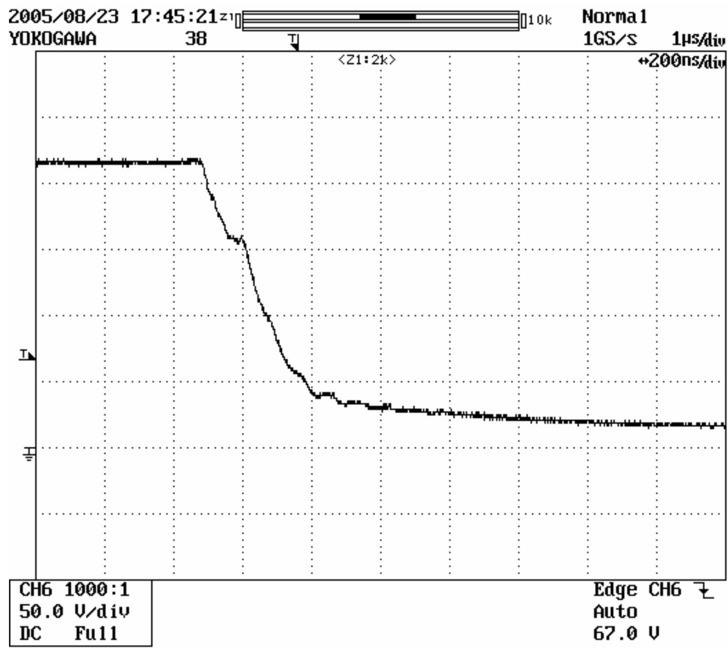

Fig. 4.32(b). Turn-on voltage waveform of SiC JFET.

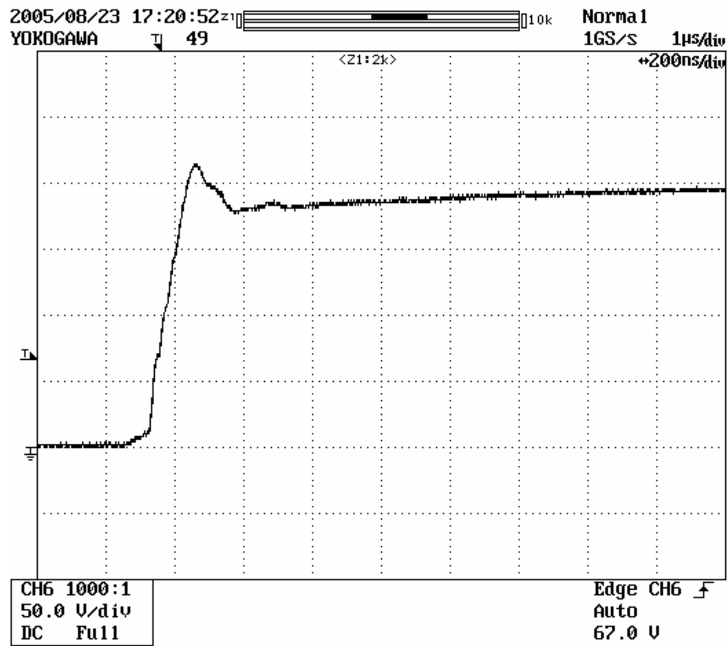

Fig. 4.33(a). Turn-off voltage waveform of Si IGBT.

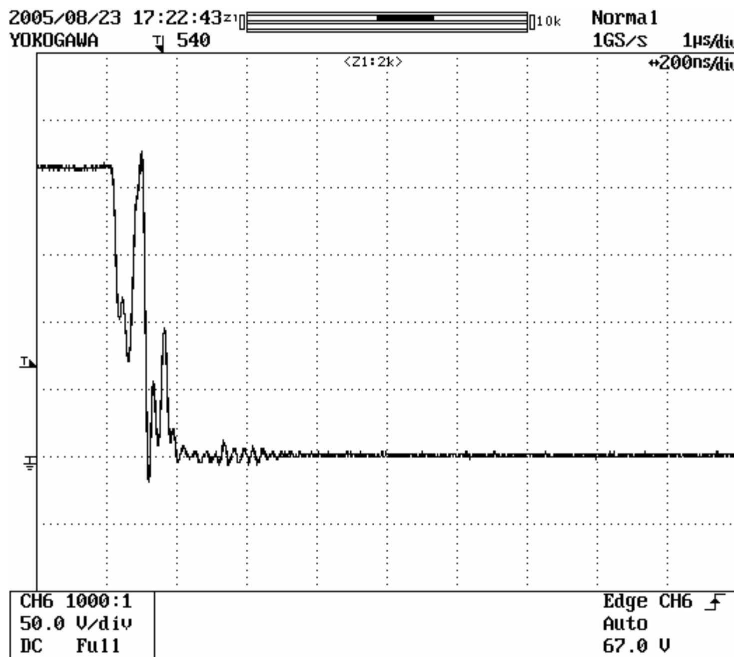

Fig. 4.33(b). Turn-on voltage waveform of Si IGBT.

4.6 CONCLUSIONS

The all-Si and all-SiC inverter modules were successfully simulated and tested with various loads. The SiC JFET and the SiC diode used in the module were characterized and the parameters were extracted to build their models. These models were used in the simulation of the inverter, and the efficiencies were found to be low.

The efficiencies of the all-SiC inverter were at least 2–3% less in the 83–95% range. The analysis of the conduction and switching losses of the devices showed that the devices in the all-SiC inverter are not as efficient as the devices in the off-the-shelf all-Si inverter module.

It should be noted that the SiC JFETs used in the all-SiC inverter were experimental samples. They still have room for improvement. The test results in this chapter should not be viewed as discouraging. The next chapter will discuss the performance of some other, more promising SiC JFETs with respect to Si IGBTs.

5. DURATION TESTS

5.1 INTRODUCTION

Reliable operation of power modules exposed to the high-temperature requirements in under the hood conditions is an important automotive requirement. Most common failures in power modules are due to temperature cycling over high-operating temperatures. Several SiC Schottky diodes and SiC power switches were tested at ORNL and their performances evaluated under different operating conditions. Even though it has been claimed that SiC devices have superior characteristics compared with Si devices, the reliability of the material quality has always been questionable.

To test the reliability of selected SiC power devices, four different buck converters were developed with Si IGBTs, Si pn diodes, SiC JFETs, and SiC Schottky diodes. The devices in the converters were operated at different voltage and current levels and at different frequencies in order to subject them to thermal stress and study their behavior. The results and analysis of the test data will be presented in the following sections.

5.2 TEST SETUP

The test setup for the duration tests is shown in Fig. 5.1. The four buck converters were enclosed in a box for higher ambient temperature and also as a protective feature. The four different buck converters are shown in Fig. 5.2.

Fig. 5.1. Test setup for duration testing.

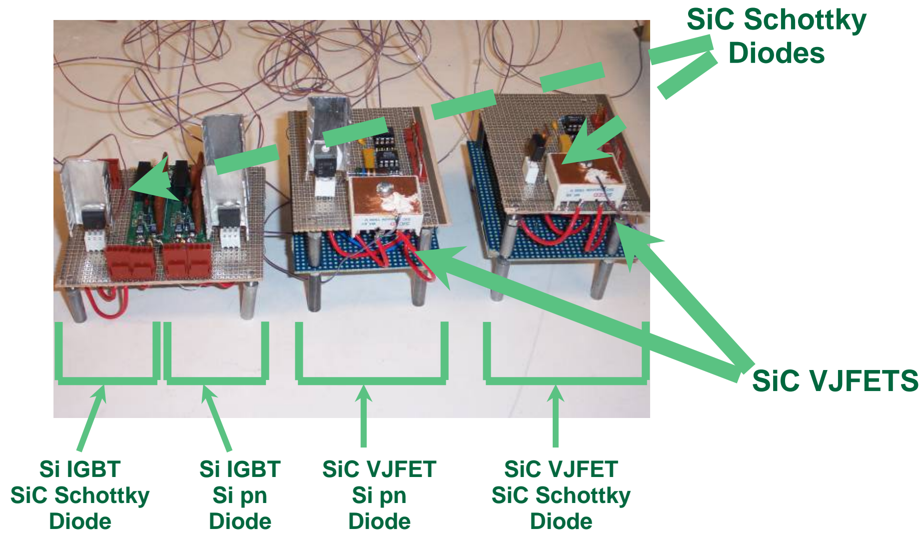

Fig. 5.2. Four different buck converters.

The specifications of the devices and components used in the converters are shown in Table 5.1, and the circuit topology is shown in Fig. 5 3. The static, dynamic, and gate characteristics of the SiC devices used in these converters were presented previously in Chapter 2.

Thermocouples were attached to the cases of these devices to monitor their thermal responses. All the devices except the SiC JFETs were attached to a heat sink.

Table 5.1. Specifications of the devices and components used in the buck converters

SiC JFET (SiCED)	**1200 V, 2 A**
SiC Schottky diode (Cree)	**600 V, 10 A**
Si IGBT (IRF)	**1200 V, 11 A**
Si pn diode (Harris)	**600 V, 10A**
Inductor	**1.2 mH**
Thermocouple	**type T**

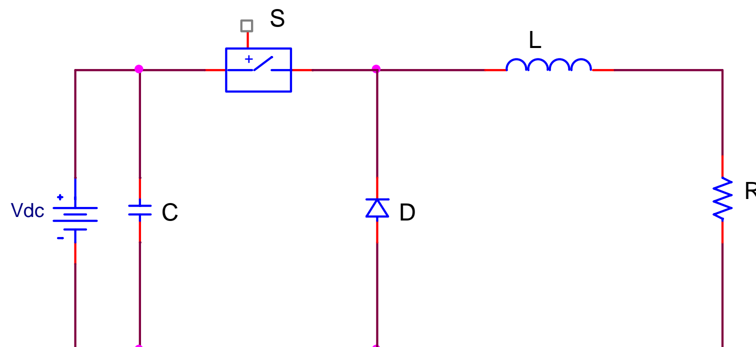

Fig. 5.3. The buck converter topology.

5.3 OPERATION

The buck converters were fed from a single dc supply source, and the load current was varied by changing the input voltage. The operating current was limited to a maximum of 2 A because of the SiC JFET current rating. They were operated continuously for 7.5 hours every day for 6 months. During this time, their operation was closely observed and their case temperature data were recorded. The following section will show some of these temperature profiles and will draw conclusions.

Note that the device temperature data obtained from the thermocouples also recorded noise over long periods of operation. The thermocouples are generally very sensitive to the noise around the measuring surface. Typical temperature profiles of switches and diodes obtained during testing are shown in Figs. 5.4 and 5.5. Only the temperature profiles of the devices in the all-SiC converter were clean. Also, the Si IGBT with the SiC diode is less noisy than the ones with Si diodes because the SiC diode has better reverse-recovery characteristics than Si pn diodes. For improved visualization, a moving average filter was used (Appendix B) to filter the noise from the signals.

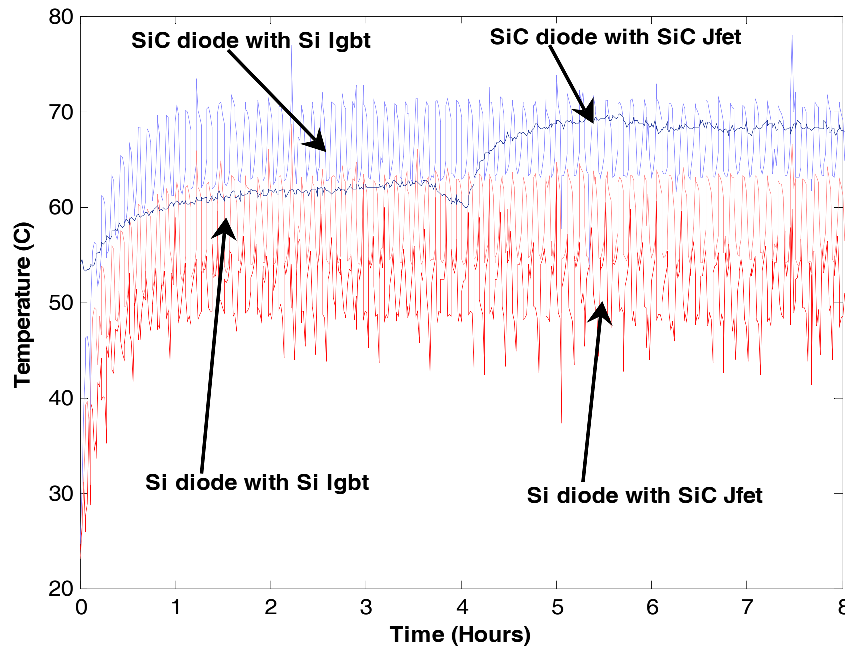

Fig. 5.4. Plot of temperature data for diodes without the filter.

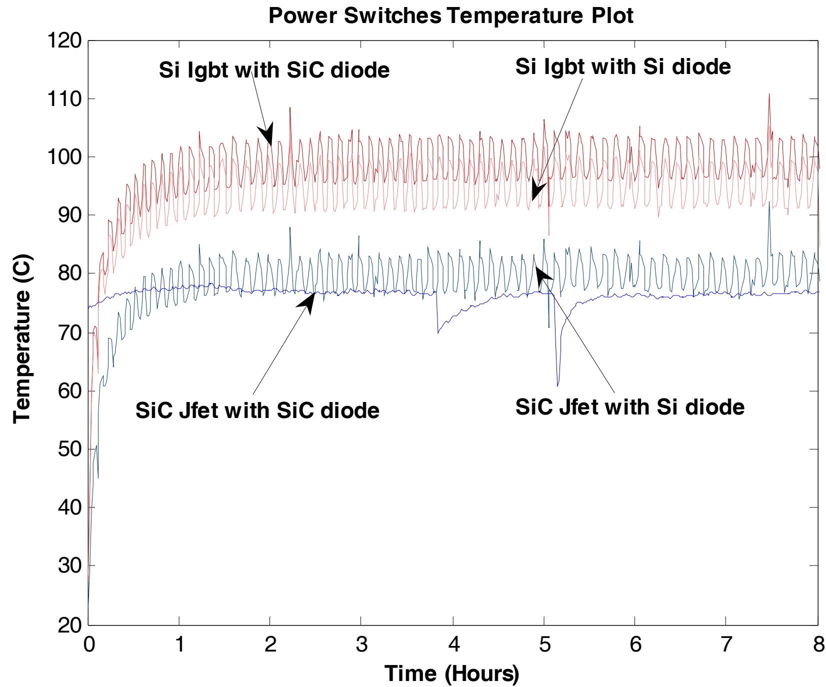

Fig. 5.5. Plot of temperature data for switches without the filter.

Case 1

The converters were first operated at 250 V, 50% duty cycle, and 10 kHz. All the devices, except the SiC JFETs ,were mounted on a heat sink. The temperature profiles for the main power switches in all the buck converters are shown in Fig. 5.6. The Si IGBTs operated at 108°C and 97°C, and the SiC JFETs were operating at much lower temperatures–around 60°C. The SiC JFETs without heat sinks were operating at lower temperatures compared with the Si IGBTs with the heat sinks.

To stress the devices to their maximum continuous operating conditions without exceeding the operating temperature, the power levels were increased in the following cases.

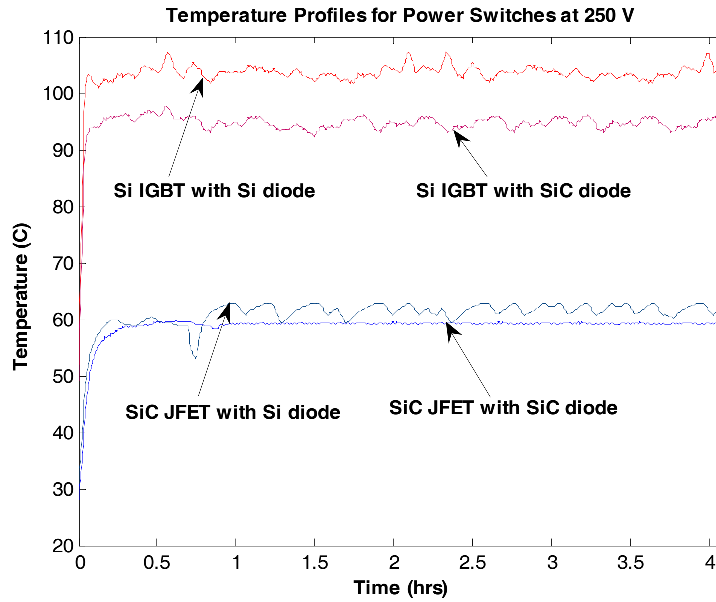

Fig. 5.6. Temperature profile for power switches at 250-V, 10-kHz operation.

Case 2

The dc input voltage was increased to 300 V, keeping all other parameters the same. The Si IGBT in the all-Si converter failed at 300-V, 1.5-A; however, the other IGBT and SiC JFETs kept operating. Table 5.2 shows the temperature at which the IGBT failed with a drain-source short because the temperature was beyond the thermal capability of the device. Note that the Si IGBT with the SiC diode did not fail. To find the reason why one IGBT failed and not the other, the turn-on current waveforms of both IGBTs were compared and are shown in Fig. 5.7.

Table 5.2. Temperature data of power devices at 300-V, 10-kHz operation

SiC JFET with Si diode, C	SiC JFET with SiC diode, C	Si IGBT with SiC diode, C	Si IGBT with Si diode, C	Time (min)
40.8	38	68.6	69.7	
64.8	60.8	116	125.1	5
82.6	75.6	141.1	168.9	10
79.6	70.6	115.7	263.3	15
82.7	71.1	118.5	287.2	20
85.3	72.4	121.5	298.9	25
86.1	72.9	122.3	293.1	30

As seen in Fig. 5.7, the Si IGBT has a current spike during turn-on because of the effect of the reverse-recovery current of the diodes. Note that to stress the devices, no snubbers are used. As expected, the peak value of the current spike is less when a SiC Schottky diode is used instead of a Si pn diode because the peak reverse-recovery current of the SiC diode is smaller. Since the reverse recovery of the diode adversely affects switching and consequently the switching losses of the IGBT, a Si pn diode will cause higher losses on the IGBT than the SiC Schottky diode. This is why a Si IGBT will be hotter when used

with a Si pn diode as opposed to a SiC Schottky diode. This effect will be more significant at higher switching frequencies because the switching losses are proportional to the switching frequency.

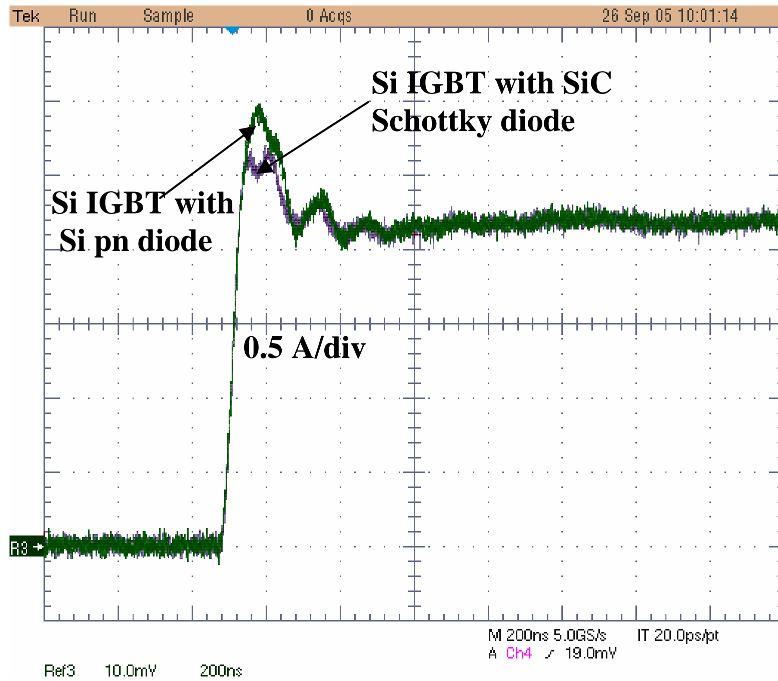

Fig. 5.7. Turn-on current waveforms of Si IGBTs with SiC and Si diodes.

Case 3

After experimenting with several test conditions, the operating voltage was fixed at 200 V for safe operation without device failure and the duration tests were continued. The converters were operated at 10 kHz, 50% duty cycle, and 200 V. The temperature profiles were obtained for different frequencies.

The temperature profiles recorded for each device for 7.5 hours are shown in Fig. 5.8. These profiles show that the SiC diodes were operating at higher temperatures than the Si diodes. Even though this seems to contradict what was said about SiC Schottky diodes earlier in this report, a previous ORNL simulation study [2] has shown that the conduction losses of SiC Schottky diodes dominate at lower switching frequencies, and they are much higher than those of the Si pn diodes. The static characteristics shown in Fig. 2.14 indicate that the on-state resistances of the SiC diodes are much higher than those of the Si pn diodes, and hence they have higher conduction losses. This confirms the results of the simulation study.

SiC JFETs, without heat sinks, operate at much lower temperatures than Si IGBTs, which indicates that the SiC devices have lower losses than the Si IGBTs. The comparison of the static characteristics of the SiC JFET and the Si IGBT is shown in Fig. 5.9. It is interesting to note that the Si IGBT and the SiC JFET with the SiC diodes operate at lower temperatures than the ones with the Si pn diodes. This is again because of the better reverse-recovery characteristics of the SiC Schottky diodes.

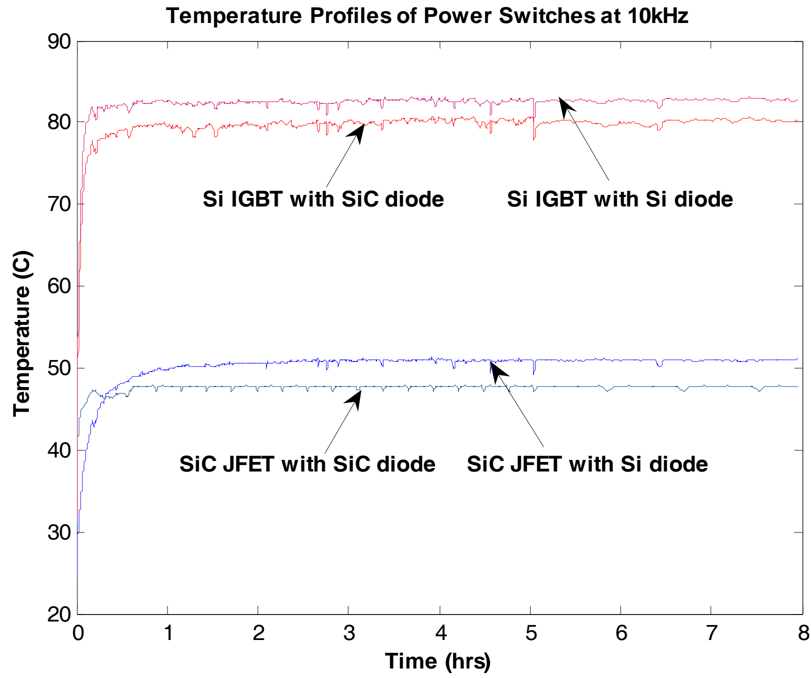

(a) Switches.

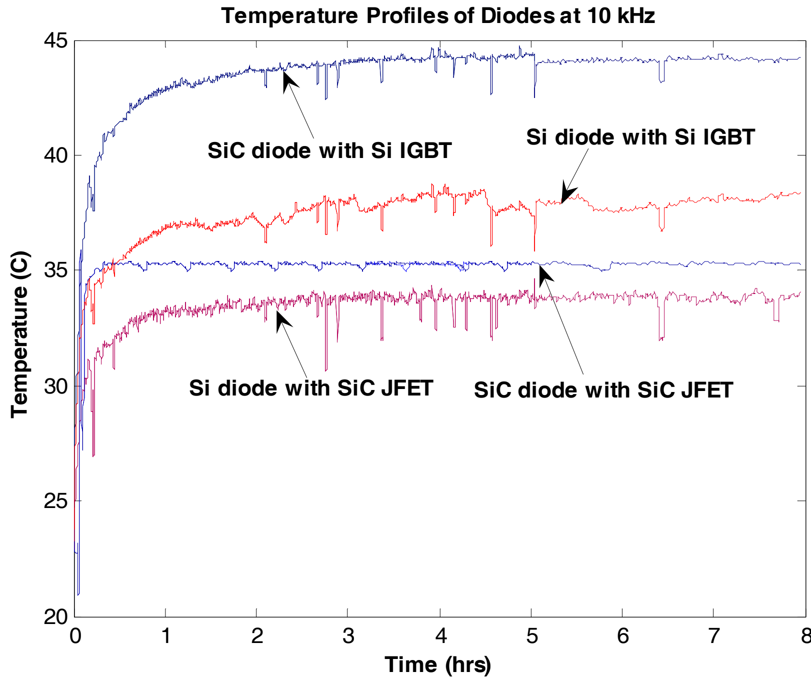

(b) Diodes.

Fig. 5.8. Temperature profile for 10-kHz operation.

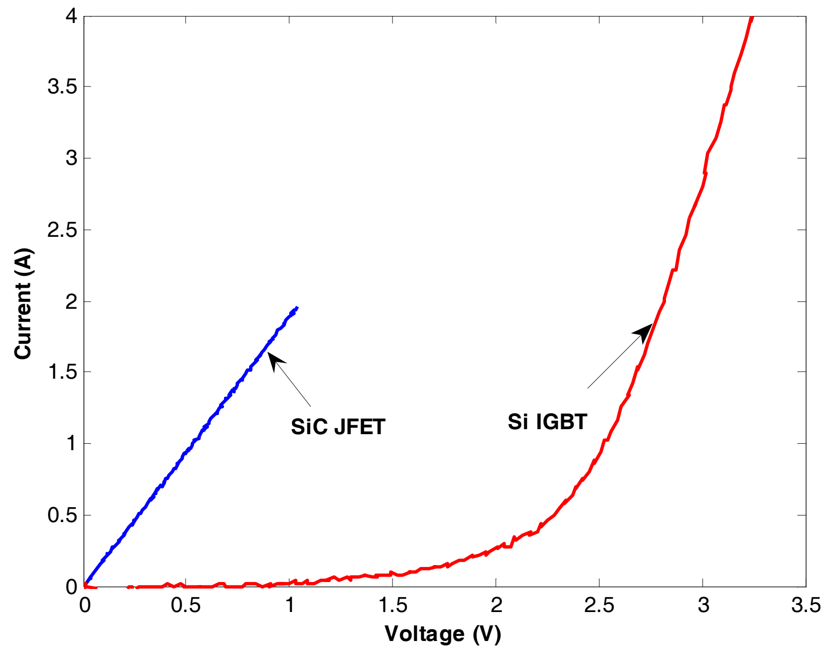

Fig. 5.9. Comparison of static characteristics for Si IGBT and SiC JFET.

Figures 5.10–5.15 show temperature profiles of the switches and diodes for different switching frequencies. Figures 5.16 and 5.17 show all the profiles in Figs. 5.10–5.15 plotted together. This figure shows that the operating temperatures of the SiC diodes do not change much with an increase in switching frequency because the switching losses of SiC Schottky diodes are significantly lower than those of the Si pn diodes. However, the Si diodes have higher switching losses, and hence their operating temperatures get higher as the frequency increases.

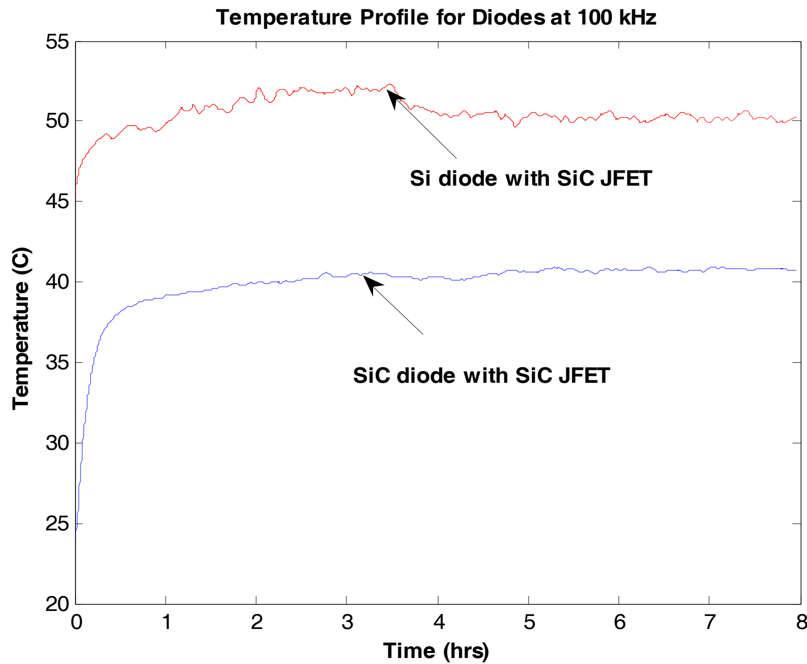

Fig. 5.10. Temperature profile for diodes at 100-kHz operation.

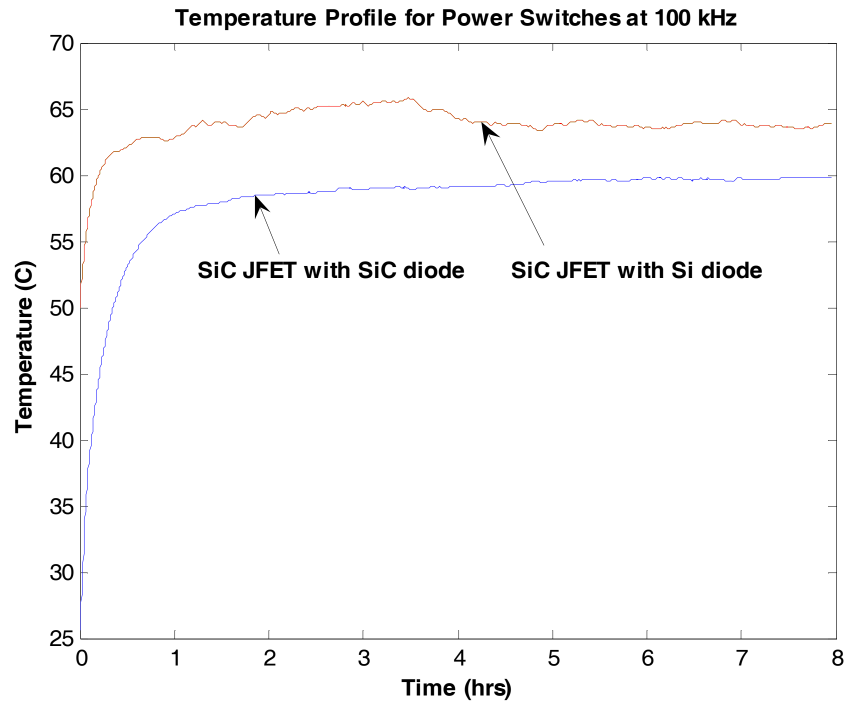

Fig. 5.11. Temperature profile for power switches at 100 kHz.

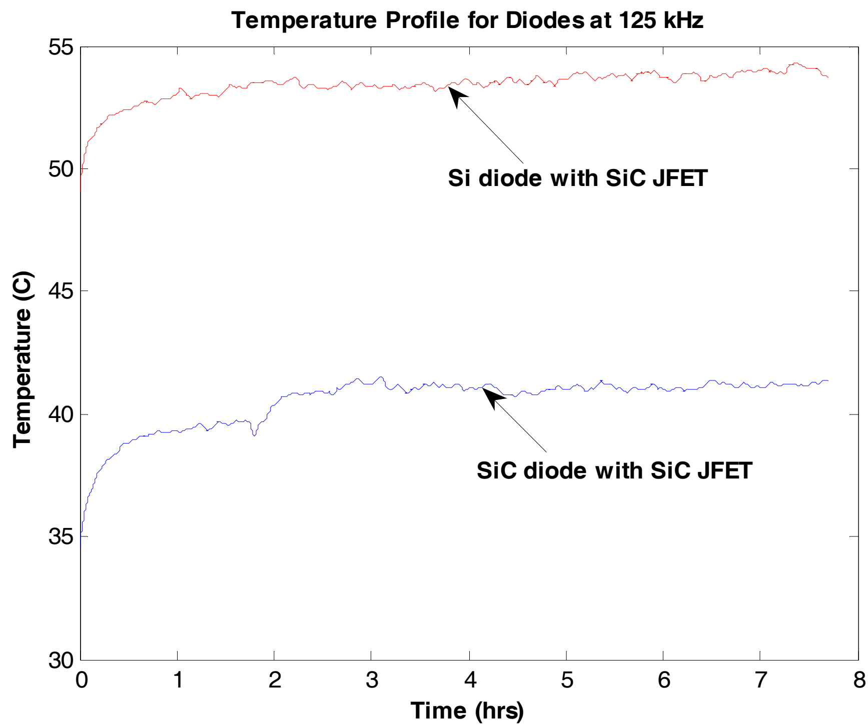

Fig. 5.12. Temperature profile for diodes at 125 kHz.

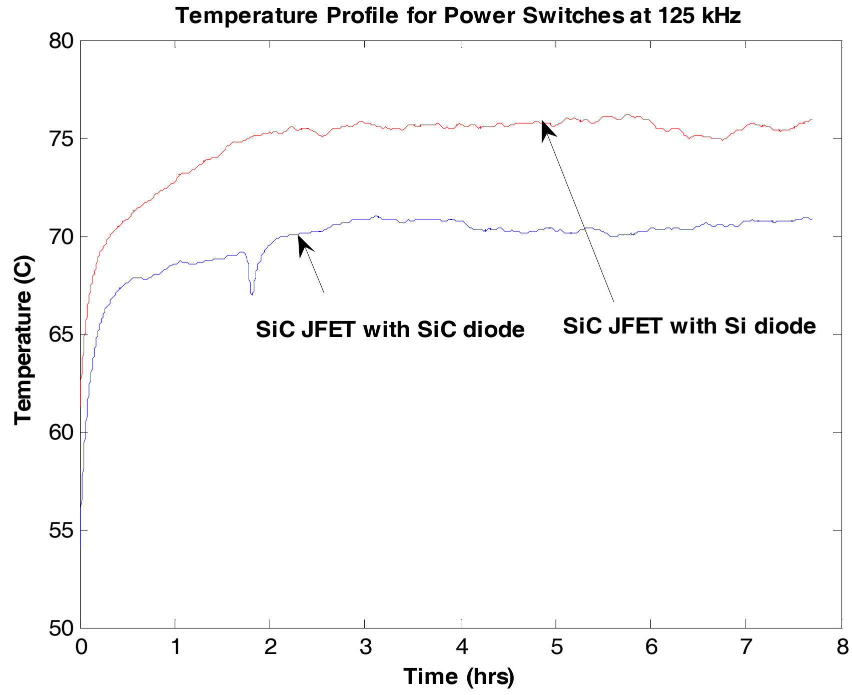

Fig. 5.13. Temperature profile for power switches at 125 kHz.

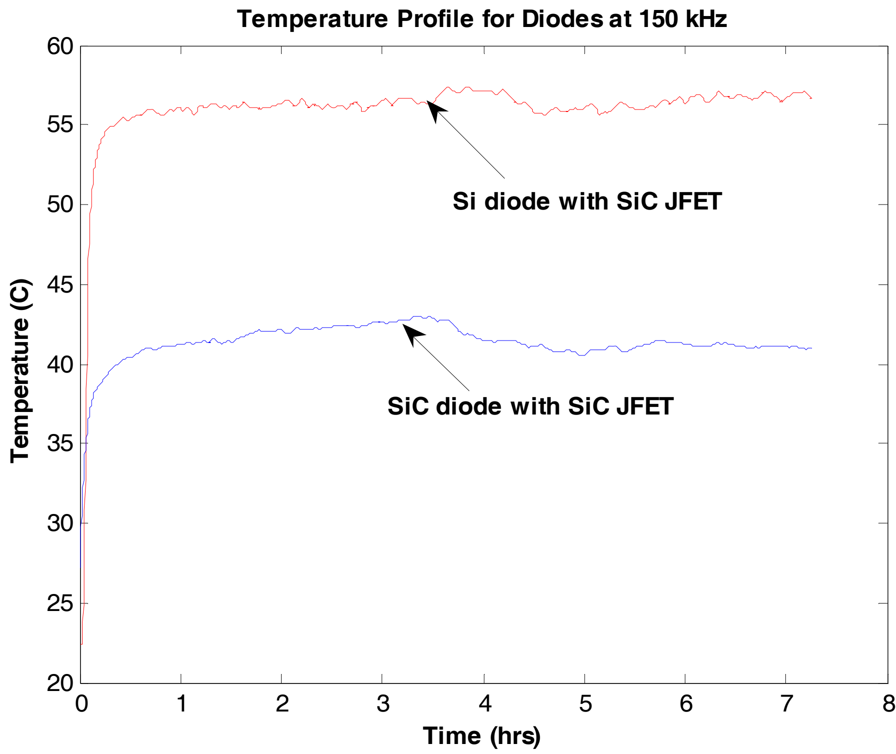

Fig. 5.14. Temperature profile for diodes at 150 kHz.

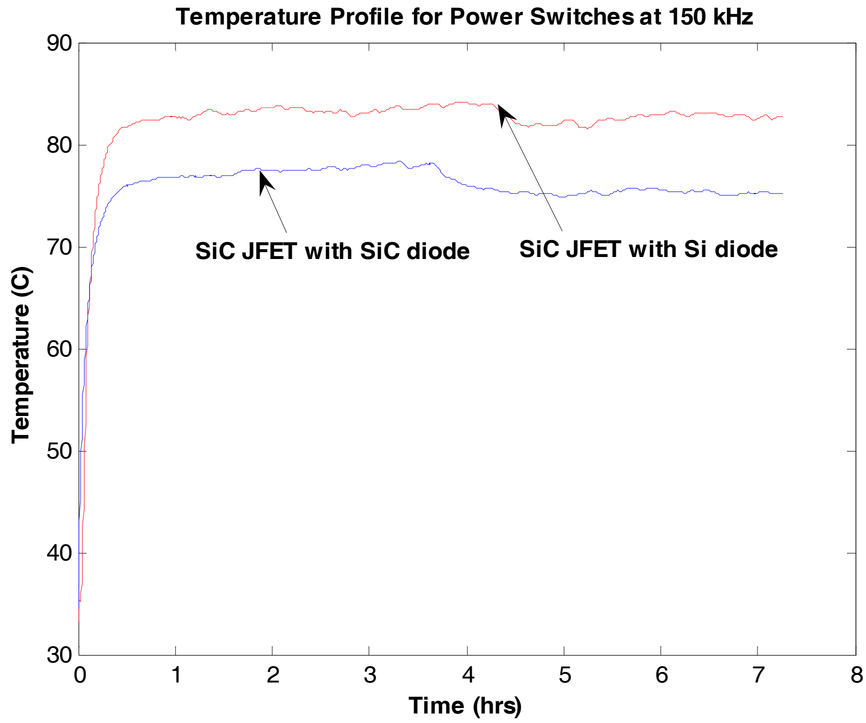

Fig. 5.15. Temperature profile for power switches at 150 kHz.

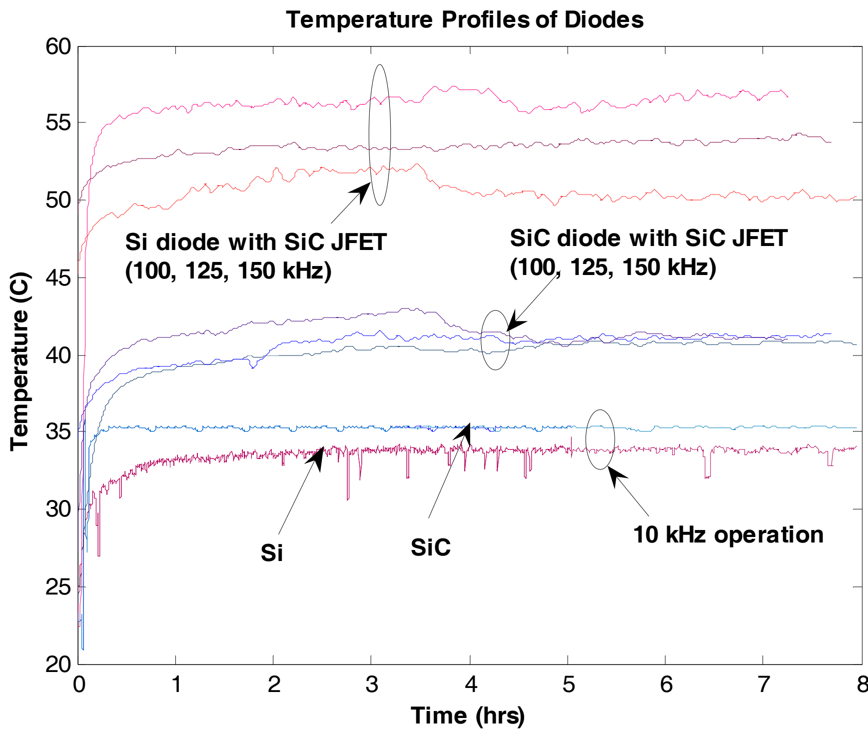

Fig. 5.16. Temperature profile for diodes at different operating frequencies.

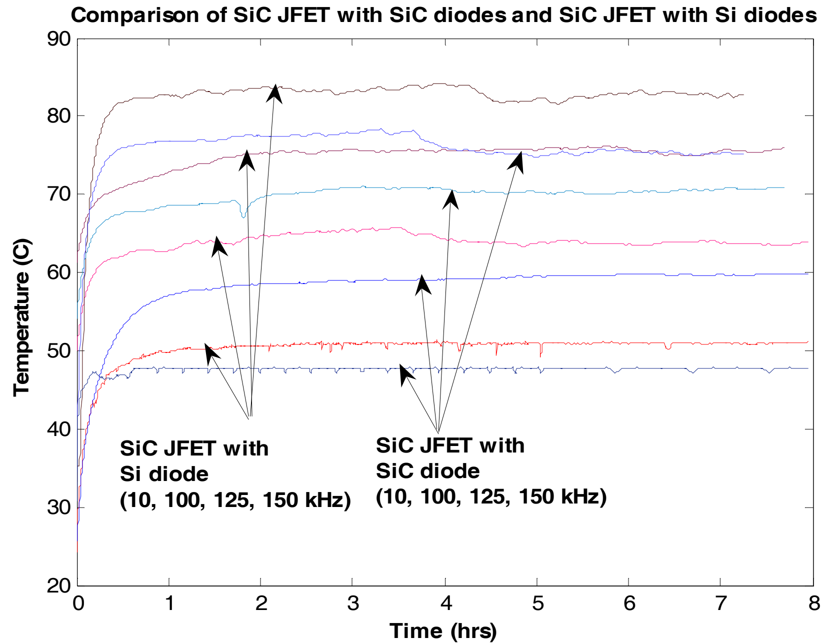

Fig. 5.17. Temperature profile for switches at different operating frequencies.

Case 4

Since Si IGBTs are limited in their switching frequency, the buck converters with Si IGBTs were tested separately at lower switching frequencies. The temperature profiles of the switches and diodes for 200 V, 50% duty cycle and in a frequency range of 15–25 kHz are shown in Figs. 5.18–5.23. Figure 5.24 shows that the temperature profile of the Si IGBT with a SiC Schottky diode does not change much with switching frequency. However, the temperature of the IGBT with a Si diode increases with switching frequency. This also shows that the SiC diodes have less effect on the main power switch because of the negligible reverse-recovery losses. Even though the temperatures of the Si IGBT in the all-Si converter increase as the switching frequency increases, the Si pn diode compared with the SiC Schottky diode still operates at a slightly lower temperature.

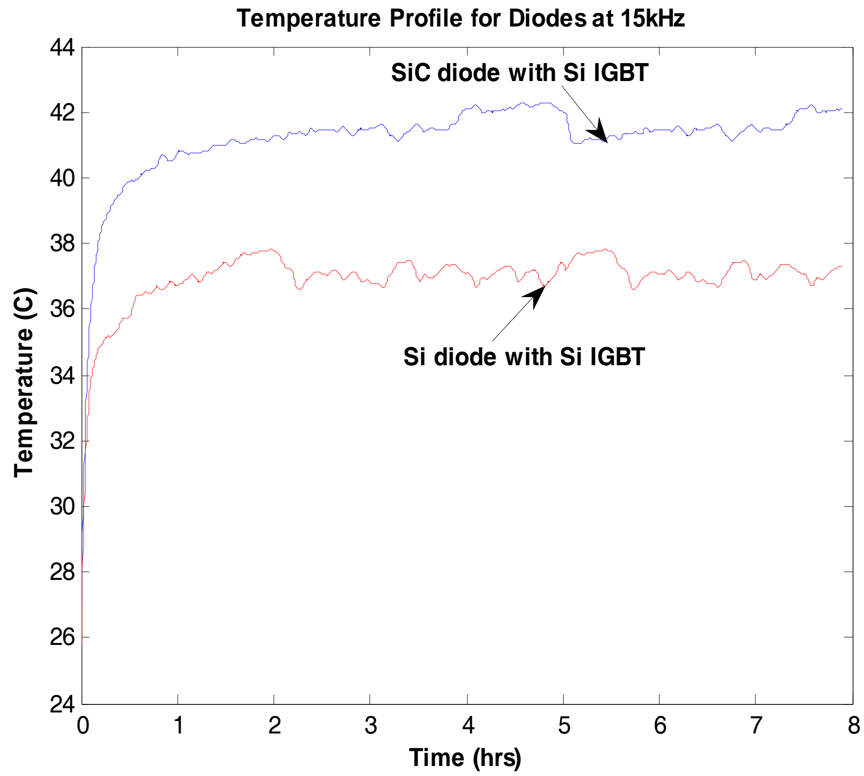

Fig. 5.18. Plot of temperature profile for diodes at 15 kHz.

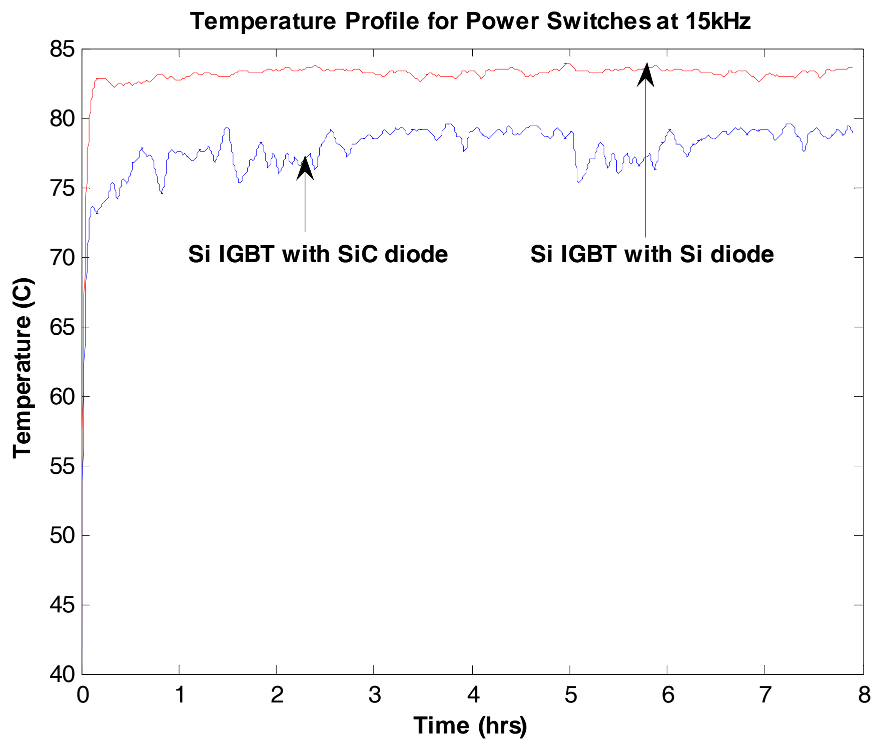

Fig. 5.19. Plot of temperature profile for power switches at 15 kHz.

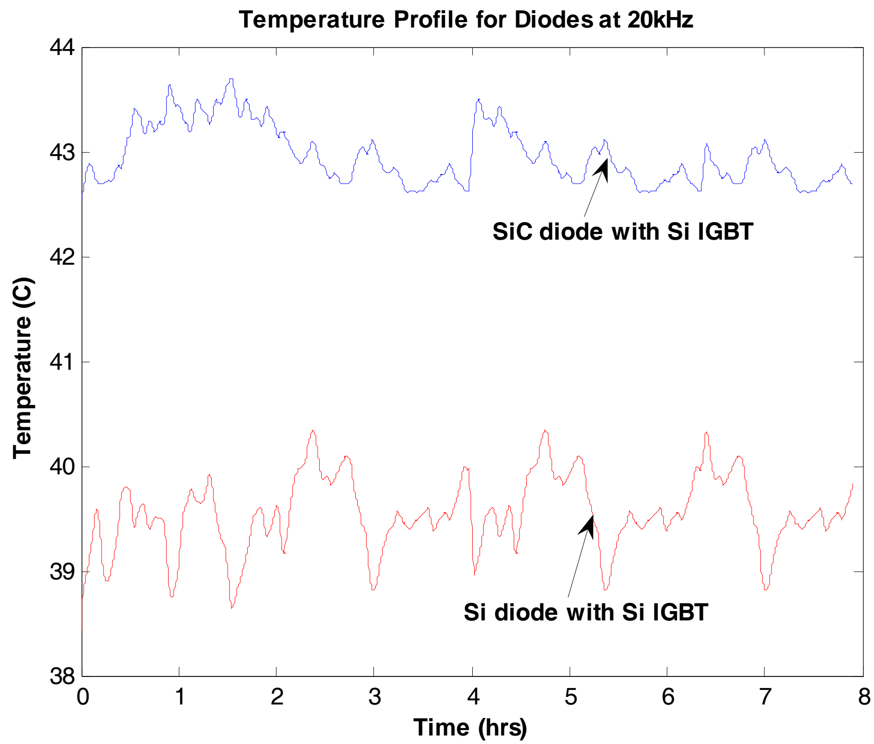

Fig. 5.20. Plot of temperature profile for diodes at 20 kHz.

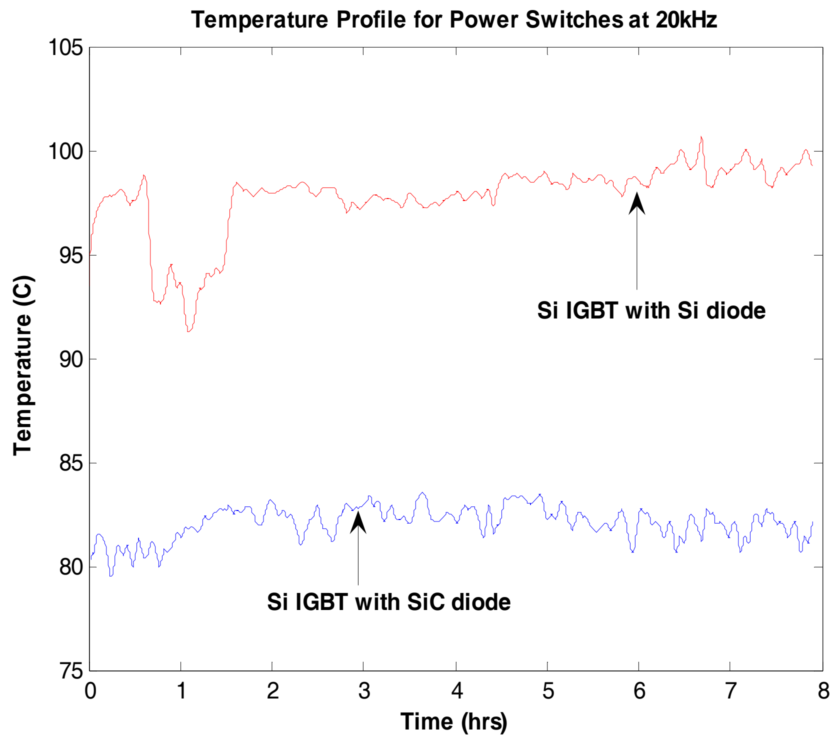

Fig. 5.21. Plot of temperature profile for power switches at 20 kHz.

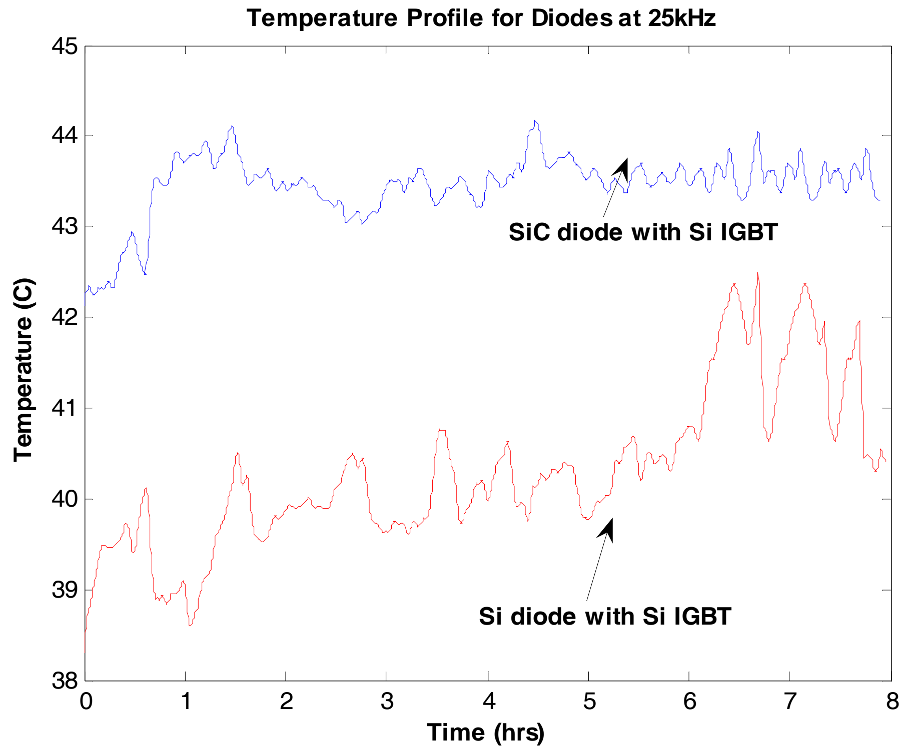

Fig. 5.22. Plot of temperature profile for diodes at 25 kHz.

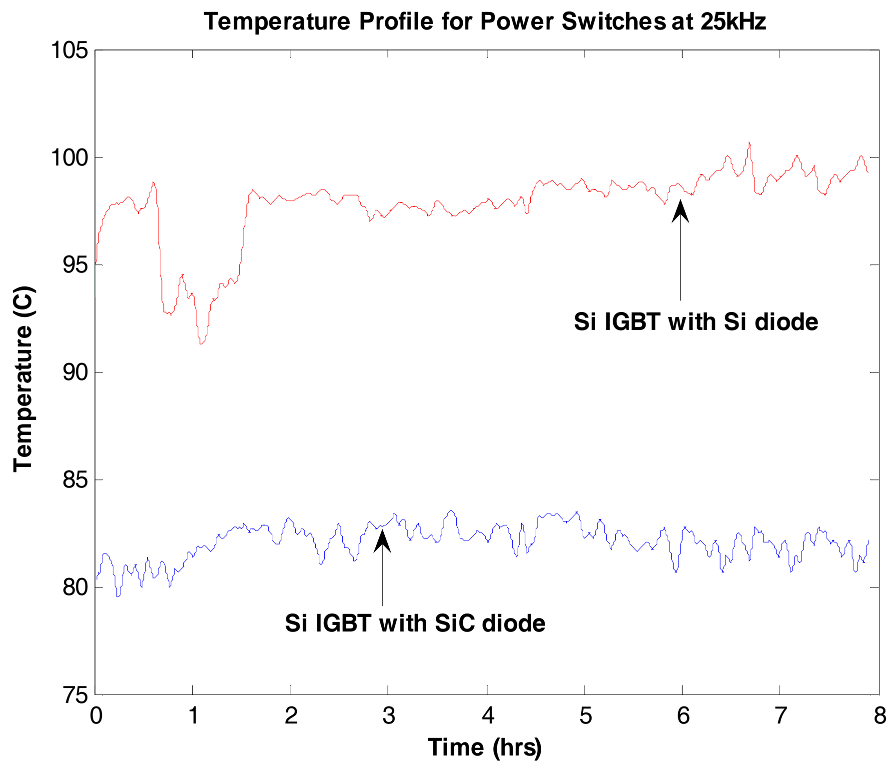

Fig. 5.23. Plot of temperature profile for power switches at 20 kHz.

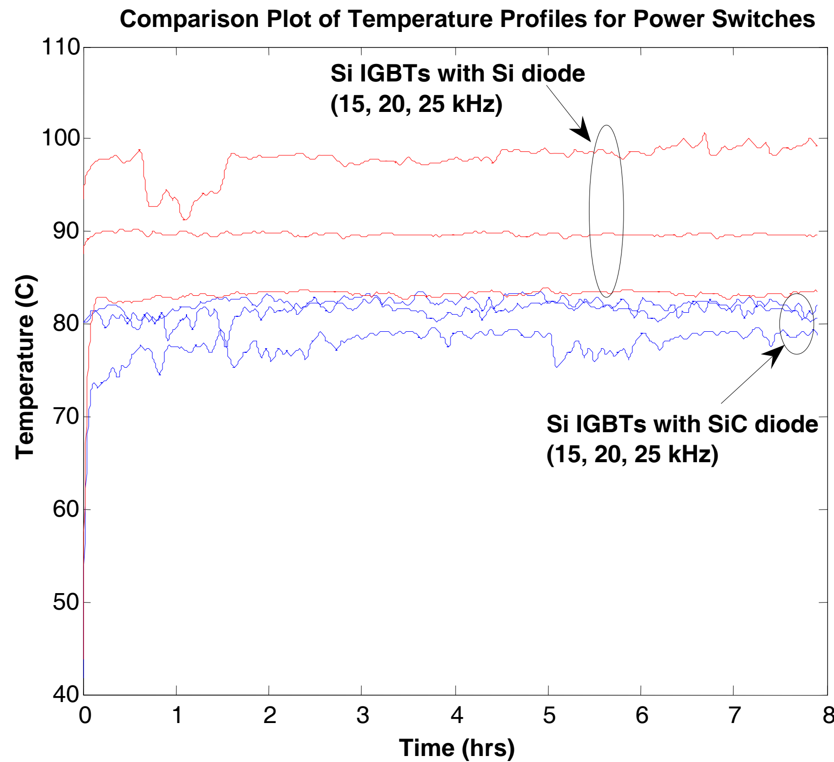

Fig. 5.24. Plot of temperature profile for power switches at different frequencies.

5.4 DEVICE FAILURE DISCUSSION

During the tests, several power switches failed at different operating conditions. The diodes never failed over several months of operation.

Si IGBTs failed at certain operating conditions because the thermal limits of the devices were exceeded. Even with heat sinks, they required cooling at higher power levels. It should be noted that only case temperatures were measured and the junction temperatures would be much higher. Note that the devices were operated without any snubber circuits, thus stressing the power switches even more than normal.

SiC JFETS operated at higher voltage levels than the Si IGBTs and without heat sinks. They failed only after several days of operation

SiC JFETs operated without any failures even at higher voltage levels and without heat sinks. However, the JFETs failed repeatedly after several days of operation. An investigation of the devices that failed found that the gate-to-source of some devices was shorted, while some had an open drain-to-source failure. This shows that these experimental samples need more reliability improvement.

5.5 CONCLUSIONS

The duration tests were completed successfully and the analysis of the data was presented. The SiC diodes have shown better thermal performance than the Si devices at higher power levels and higher frequencies. However, at lower frequencies and for the same power levels, the Si diodes had lower losses and hence were operating at lower temperatures.

The SiC JFETs were operating at lower temperatures for all the operating conditions than the Si IGBTs, even without heat sinks. The temperatures of the SiC JFETs operating at 150 kHz were comparable to the temperatures of Si IGBTs operating at 10 kHz for the same power levels. This significant difference in operating temperatures will result in reduced heat sink size and volume when SiC devices are used.

Some Si IGBTs failed during operation because of the extreme stresses they were under. Some SiC JFETs also may have failed because these are still experimental samples and they need further improvement.

6. CONCLUSIONS

Several new SiC devices were acquired, tested, and characterized over a wide temperature range, and the results were presented in Chapter 2 of this report.

The SiC Schottky diode parameters were extracted from test data and models were developed in Saber. The SiC diode models were used in an inverter model, and the simulation studies showed that the efficiencies of the Si IGBT, SiC diode hybrid inverter were higher than an all Si inverter. The 55-kW Si IGBT–SiC Schottky diode hybrid inverter developed in collaboration with Cree and Semikron was tested extensively. The inverters were tested with an inductive load and a dynamometer load. They were operated in motoring and regeneration modes to study the effect of the SiC Schottky diodes on the system. The efficiencies of the hybrid inverter were measured and revealed that they were higher than those of the Si inverter. The average loss reduction in the hybrid inverter was up to 35% with an inductive load. The inverters were tested to a maximum power of 47 kW.

The SiC JFET parameters were extracted from the test data and the models were developed in Saber. The models were used to study the inverter performance. The results showed that the efficiencies were low (83–94%). The all-SiC inverter module developed in collaboration with Rockwell was tested with inductive and pure resistive loads and compared with an IGBT-based Si module. The efficiencies of the SiC module were less compared with the Si module because of the higher on-state losses of the SiC JFET. It should be noted that the SiC JFETs are still prototype devices, and it appears that the SiC power switches need further improvement to make them comparable to the Si devices.

Duration tests were conducted using buck converters. Four buck converters were built with different combinations of Si IGBTs, SiC JFETs, Si pn, and SiC Schottky diodes. The converters were operated an average of 7.5 hours a day for several months. The experiments revealed that the SiC JFETs had better performance in terms of operating temperatures for the same power levels with the same load. The SiC Schottky diodes had better thermal performance at higher frequencies since they have lower reverse-recovery losses compared with the Si diodes.

It was interesting to note that the all-SiC converter and the hybrid converter (Si IGBT–SiC diode) had less noise in the thermal data than the Si-based converters. This indicates that there is a reduction in emitted noise when SiC devices are used.

The diodes in the duration tests never failed even after several months of operation. The Si IGBTs failed only for some operating conditions. However, the SiC JFETs failed repeatedly after several days of operation. This shows that the SiC JFETs are not yet mature enough to handle long-duration operation.

It can be concluded that the SiC Schottky diodes perform better than similar Si pn diodes. The use of SiC Schottky diodes in traction drives results in much lower losses for the same operating conditions. The reliability of the power switches is a concern, but their performance is promising.

It is important to follow current developments in SiC power-device technology closely because the pace of improvement has increased considerably. Better, less expensive and more reliable SiC power devices are not far away.

7. REFERENCES

1. B. Ozpineci, L. M. Tolbert, S. K. Islam, and F. Z. Peng, "Testing, Characterization, and Modeling of SiC Diodes for Transportation Applications," pp. 1673–1678 in *IEEE Power Electronics Specialists Conference*, Cairns, Australia, June 23–27, 2002.

2. L. M. Tolbert, B. Ozpineci, S. K. Islam, and F. Z. Peng, "Impact of SiC Power Electronic Devices for Hybrid Electric Vehicles," pp. 765–771 in *SAE 2002 Transactions Journal of Passenger Cars–Electronic and Electrical Systems*, ISBN 0-7680-1291-0, 2003.

3. B. Ozpineci and L. M. Tolbert, *Comparison of Wide Bandgap Semiconductors for Power Electronics Applications*, ORNL/TM-2003/257, UT-Battelle, LLC, Oak Ridge National Laboratory, November 2003.

4. S. Hodge, "SiC Schottky Diodes in Power Factor Correction," pp. 14–18 in *Power Electronics Technology*, August 2004.

5. H. R. Chang, E. Hanna, and A. V. Radun, "Demonstration of Silicon Carbide (SiC)–Based Motor Drive," pp. 1116–1121 in *Conference of the IEEE Industrial Electronics Society*, November 2–6, 2003.

6. A. M. Abou-Alfotouh, A. V.Radun, H. R. Chang, and C. Winerhalter, "A 1 MHz Hard-Switched Silicon Carbide DC/DC Converter," pp. 132–138 in *IEEE Applied Power Electronics Conference*, February 9–13, 2003.

7. M. Bhatnagar, P. K. McLarty, and B. J. Baliga, "Silicon Carbide High Voltage (400 V) Schottky Barrier Diodes," pp. 501–503 in *IEEE Electron Device Letters*, October 1992.

8. M. Chinthavali, B. Ozpineci, and L. M. Tolbert, "High Temperature Characterization of SiC Power Electronic Devices," pp. 43–47 in *IEEE Workshop on Power Electronics in Transportation*, October 21–22, 2004.

9. A. R. Hefner, R. Singh, J. Lai, D. W. Berning, S. Bouche, and C. Chapuy, "SiC Power Diodes Provide Breakthrough Performance for a Wide Range of Applications," pp. 273–280 in *IEEE Transactions on Power Electronics*, March 2001.

10. M. L. Heldwein and J. W. Kolar, "A Novel SiC J-FET Gate Drive Circuit for Sparse Matrix Converter Applications," pp. 116–121 in *IEEE Applied Power Electronics Conference*, February 22–26, 2004.

11. B. Allebrand and H. Nee, "On the Possibility to Use SiC JFETs in Power Electronic Circuits," *European Conference on Power Electronics and Applications,* Austria, 2001.

12. M. Ruff, H. Mitlehner, and R. Helbig, "SiC Devices: Physics and Numerical Simulation," pp. 1040–1054 in *IEEE Transactions on Electron Devices*, June 1994.

13. D. Peters, H. Mitlehner, R. Elpelt, R. Schorner, and D. Stephani, "State of the Art Technological Challenges of SiC Power MOSFETs Designed for High Blocking Voltages," *European Conference on Power Electronics and Applications*, Toulouse, France, September 2–4, 2003.

14. S. H. Ryu, A. Agarwal, J. Richmond, J. Palmour, N. Saks, and J. Williams, "10 A, 2.4 kV Power DIMOSFETs in 4H-SiC," pp. 321–323 in *IEEE Electron Device Letters*, June 2002.

15. S. H. Ryu, S. Krishnaswami, M. Das, J. Richmond, A. Agarwal, J. Palmour, and J. Scofield, "4H-SiC DMOSFETs for High Speed Switching Applications," *5th European Conference on Silicon Carbide Related Materials*, August 31–September 4, 2004.

16. K. Mino, K. S. Herold, and J. W. Kolar, "A Gate Drive Circuit for Silicon Carbide JFET," pp. 1162–1166 in *Conference of the IEEE Industrial Electronics Society*, November 2–6, 2003.

17. M. Chinthavali, B. Ozpineci, and L. M. Tolbert, "Enhancing Power Electronic Devices with Wide Bandgap Semiconductors," *Advanced Workshop on Frontiers of Electronics*, Aruba, December 17–22, 2004.

18. T. R. McNutt, "Modeling and Characterization of Silicon Carbide Power Devices," Ph.D. Dissertation, Department of Electrical Engineering, University of Arkansas, Fayetteville, Arkansas, 2004.

19. D. Zendzian, *AIPM 42 V Software Functional Description Manual*, SEMIKRON, Inc., March 2002.

20. A. S. Kashyap, "Compact Modeling of Silicon Carbide Junction Field Effect Devices," M.S. Thesis, Department of Electrical Engineering, University of Arkansas, Fayetteville, Arkansas, 2005.

APPENDIX A: i-v CHARACTERISTICS OF SiC AND Si DIODES

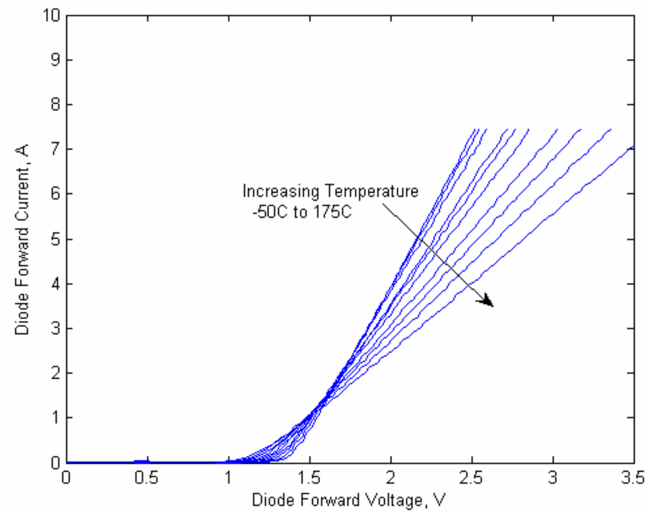

Fig. A.1. *i-v* characteristics of S1 (1200 V, 7.5 A) at different operating temperatures.

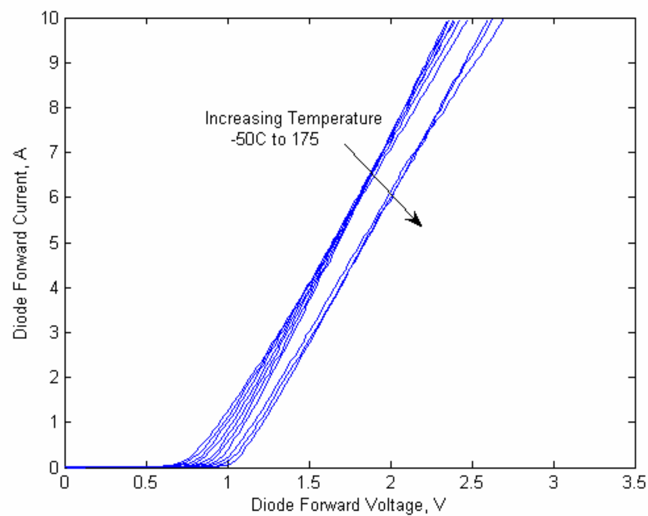

Fig. A.2. *i-v* characteristics of S4 (300 V, 10 A) at different operating temperatures.

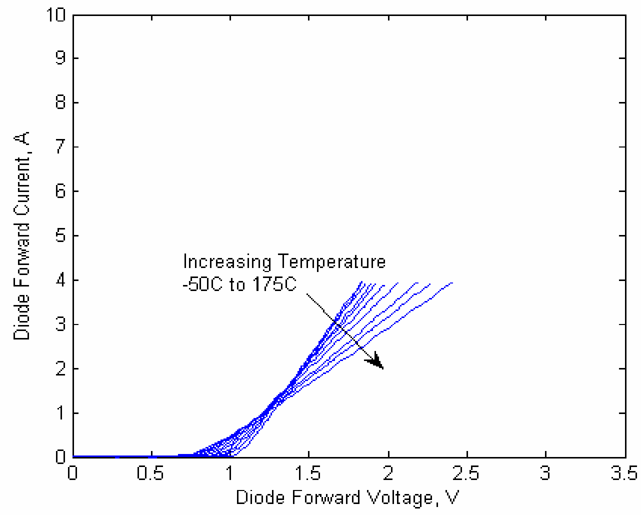

Fig. A.3. ***i-v*** **characteristics of S2 (600 V, 4 A) at different operating temperatures.**

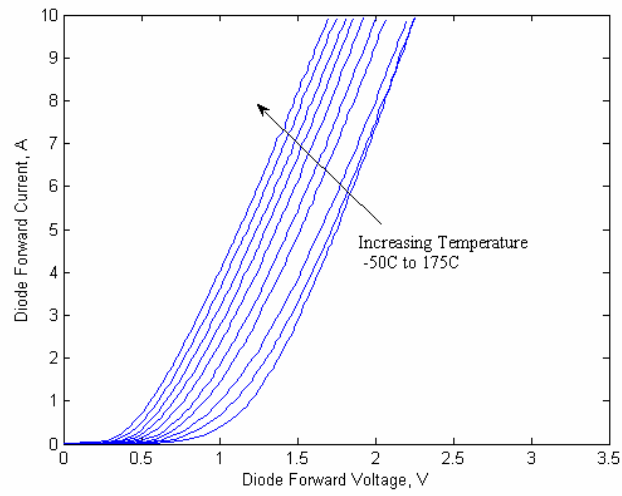

Fig. A.4. ***i-v*** **characteristics of Si pn diode (600 V, 10 A) at different operating temperatures.**

APPENDIX B: MOVING AVERAGE FILTER EXPLANATION

A moving average filter is a low-pass filter generally used to smooth the data and to remove the noise in the sampled data. The moving average filter can be viewed as a window (an array of data points considered at one time); moving along the data and the data points inside the window will be averaged to find a new value. The smoothness of the data depends on the size of the window. A new array of the averaged values of size N will be created where

$$N = \textbf{array size/window size}$$

The window size chosen for all the data plots is 13.

Matlab code:

```
clear all
b=load('275v_total_data.m');
s=b(:,9);percent input data array
M=13;percent window size
sum1=0;
for n=1:max(size(s))-M
  for j=1:M
    sum1=sum1+s(n+j);
  end
  ss(n)=sum1/M;
sum1=0;
end
f=max(size(ss))
for h =1:1:f
  t(h)=b(h,1)/3600;
end
plot(t,ss,'g')
      hold on
```

DISTRIBUTION

Internal

1. D. J. Adams
2. E. C. Fox
3. K. P. Gambrell
4. L. D. Marlino
5. M. Olszewski
6. M. Starke

7–8. Laboratory Records

External

9. T. Q. Duong, U.S. Department of Energy, EE-2G/Forrestal Building, 1000 Independence Avenue, S.W., Washington, D.C. 20585.
10. R. R. Fessler, BIZTEK Consulting, Inc., 820 Roslyn Place, Evanston, Illinois 60201-1724.
11. K. Fiegenschuh, Ford Motor Company, Scientific Research Laboratory, 2101 Village Road, MD-2247, Dearborn, Michigan 48121.
12. V. Garg, Ford Motor Company, 15050 Commerce Drive, North, Dearborn, Michigan 48120-1261.
13. E. Jih, Ford Motor Company, Scientific Research Laboratory, 2101 Village Road, MD-1170, Rm. 2331, Dearborn, Michigan 48121.
14. W. C. Johnson, University of Tennessee-Knoxville, ECE Department, 414 Ferris Hall, 1508 Middle Drive, Knoxville, Tennessee 37996.
15. A. Lee, Daimler Chrysler, CIMS 484-08-06, 800 Chrysler Drive, Auburn Hills, Michigan 48326-2757.
16. F. Liang, Ford Motor Company, Scientific Research Laboratory, 2101 Village Road, MD1170, Rm. 2331/SRL, Dearborn, Michigan 48121.
17. M. W. Lloyd, Energetics, Inc., 7164 Columbia Gateway Drive, Columbia, Maryland 21046.
18. M. Mehall, Ford Motor Company, Scientific Research Laboratory, 2101 Village Road, MD-2247, Rm. 3317, Dearborn, Michigan 48124-2053.
19. N. Olds, USCAR, nolds@uscar.org.
20. J. Rogers, Chemical and Environmental Sciences Laboratory, GM R&D Center, 30500 Mound Road, Warren, Michigan 48090-9055.
21. S. A. Rogers, U.S. Department of Energy, EE-2G/Forrestal Building, 1000 Independence Avenue, S.W., Washington, D.C. 20585.
22. G. S. Smith, General Motors Advanced Technology Center, 3050 Lomita Boulevard, Torrance, California 90505.
23. E. J. Wall, U.S. Department of Energy, EE-2G/Forrestal Building, 1000 Independence Avenue, S.W., Washington, D.C. 20585.
24. B. Welchko, General Motors Advanced Technology Center, 3050 Lomita Boulevard, Torrance, California 90505.
25. P. G. Yoshida, U.S. Department of Energy, EE-2G/Forrestal Building, 1000 Independence Avenue, S.W., Washington, D.C. 20585.